To the Graduate Council:

I am submitting herewith a dissertation written by Burak Ozpineci entitled "System Impact of Silicon Carbide Power Electronics on Hybrid Electric Vehicle Applications." I have examined the final electronic copy of this dissertation for form and content and recommend that it be accepted in partial fulfillment of the requirements for the degree of Doctor of Philosophy, with a major in Electrical Engineering.

Leon M. Tolbert
Major Professor

We have read this dissertation
and recommend its acceptance:

Syed K. Islam

Jack S. Lawler

Jeffrey W. Hodgson

Accepted for the Council :

Anne Mayhew
Vice Provost and
Dean of Graduate Studies

(Original signatures are on file with official student records.)

SYSTEM IMPACT OF SILICON CARBIDE POWER ELECTRONICS ON HYBRID ELECTRIC VEHICLE APPLICATIONS

A Dissertation
Presented for the
Doctor of Philosophy Degree
The University of Tennessee, Knoxville

Burak Ozpineci
August 2002

DEDICATION

This dissertation is dedicated to my parents

Mrs. Gülderen Özpineci

and

Mr. Oktay Özpineci

My family and I had to go through a lot of obstacles to come to this point. Although from far away, I still feel their presence supporting me to overcome any obstacles, however big they may be.

Mom, both of your sons are doctors now like you always wanted, not medical doctors though.

ACKNOWLEDGEMENTS

I would like to thank many people who supported me in finishing this dissertation. I am most thankful to my advisor, Dr. Leon M. Tolbert for taking a chance on me almost two years ago, providing me with opportunities I had not even dreamt of, and for his supervision, his guidance, his unending support, and his friendship.

Thanks are also extended to my committee members, Drs. Jeffrey W. Hodgson, Syed K. Islam, and Jack S. Lawler not just for being in my committee but for also supporting me during all my years at The University of Tennessee.

I would like to acknowledge Donald J. Adams, John W. McKeever, and Robert M. Schilling Jr. for providing me with the opportunity to work at Oak Ridge National Laboratory. I would also like to thank ORNL SiC Team and ORNL PEEMRC members for their valuable discussions.

I had the pleasure of meeting many people during my studies in Knoxville. Among them, the most significant figure in my life at UT was Joao O. P. "Oh, man!" Pinto, I will always remember our discussions and most of all our friendship. Thank you for all of the good times.

I would also like to acknowledge Luiz E. B. da Silva for making me understand that change is not always bad.

My thanks are also extended to Mrs. Lola and Dr. Nejat M. Tajen for making me feel at home thousands of miles away from home.

Finally, someone special for me deserves extra recognition, Alev Tajen for being there for me in the difficult times. I do not know how I could have gone through the first four and a half years of my studies at UT without her unending moral support.

I also would like to acknowledge the U.S. Department of Energy and Oak Ridge National Laboratory for funding the SiC project, and the Electrical and Computer Engineering Department as well as the GATE program for their financial support in the first years of my studies.

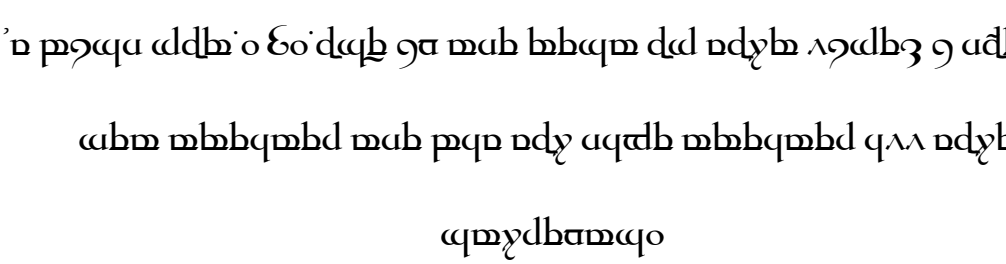

ABSTRACT

The emergence of silicon carbide- (SiC-) based power semiconductor switches with their superior features compared with silicon (Si) based switches has resulted in substantial improvements in the performance of power electronics converter systems. These systems with SiC power devices are more compact, lighter, and more efficient, so they are ideal for high-voltage power electronics applications including hybrid electric vehicle (HEV) power converters.

In this dissertation, first, a power supply converter and a traction drive converter of an HEV are selected and then, the impact of SiC-based power devices on these converters is investigated. Reductions in heatsink size and device losses with the increase in the efficiency are analyzed using an averaging model of a three-phase PWM inverter in the traction drive. In addition to these, the reductions in the filter and transformer size for the power supply are also included. For more accurate results, experimental data and/or device physics are taken into consideration to model power diodes and MOSFETs.

Finally, suggestions of parameter modification to design better performing application specific power devices are made after a parametric study of the devices.

TABLE OF CONTENTS

Chapter	Page
1 Introduction……..	**1**
1.1 Transportation requirements……..	2
1.2 Why not silicon?……	3
1.3 Why silicon carbide?……...	6
1.4 Other SiC application areas……	8
1.4.1 Aerospace applications……	9
1.4.2 Power systems applications……	9
1.5 Outline of the dissertation……	10
2 Literature Survey……	**12**
2.1 History of SiC……..	13
2.2 Physical properties of SiC……	15
2.2.1 Wide bandgap…….	17
2.2.2 High electric breakdown field……..	20
2.2.3 High saturated drift velocity……	24
2.2.4 High thermal stability……	24
2.3 SiC power devices…….	25
2.3.1 High voltage devices……..	26
2.3.2 High temperature operation…….	28
2.3.3 High frequency operation…….	29
2.3.4 High reliability……	29
2.4 SiC power device applications……...	30
2.5 The next steps……..	31
3 Devices……	**33**
3.1 Diodes……..	35
3.1.1 Types of diodes……	36
3.1.1.1 pn diodes……	36
3.1.1.2 Schottky diodes……..	38
3.1.2 Loss Modeling…….	40
3.1.2.1 Conduction losses……..	40
3.1.2.1.1 Ideal diode IV characteristics……	40
3.1.2.1.2 Finding diode parameters……	43

3.1.2.1.3 Piece Wise Linear (PWL) model of a power diode…… 45
3.1.2.1.4 Calculating conduction losses…….. 46
3.1.2.1.5 Conduction losses of a 200 A diode……. 50
3.1.2.2 Switching losses…… 52
3.1.2.2.1 Derivation of the switching loss expression……..…… 53
3.1.2.2.2 Finding switching losses experimentally… 56
3.1.2.2.3 Switching losses of a 200 A diode……..…. 66
3.2 MOSFETs……...…… 67
3.2.1 Types of MOSFETs……...…….. 68
3.2.2 Loss Modeling……. 70
3.2.2.1 Conduction losses……...…….. 70
3.2.2.2 Switching losses……. 74
3.3 Summary……...……. 76

4 Systems……..… **78**
4.1 Dc-dc Power Supply……...…….. 80
4.1.1 The dc-dc converter operation……...…….. 82
4.1.2 Thermal studies…….. 83
4.1.2.1 MOSFET losses…….. 83
4.1.2.1.1 Conduction losses……...…... 83
4.1.2.1.2 Switching losses…….. 84
4.1.2.2 Diode losses……...… 85
4.1.2.2.1 Conduction losses……..... 85
4.1.2.2.2 Switching losses…….. 86
4.1.2.3 Results……. 86
4.1.3 Passive components……...… 91
4.1.3.1 High frequency transformer…… 91
4.1.3.2 Output filter requirements……... 93
4.1.3.2.1 The size of the filter capacitor……... 96
4.1.3.2.2 The size of the filter inductor…… 96
4.2 Electric Traction Drive……...…….. 97
4.2.1 Average modeling of the inverter…… 99
4.2.1.1 Derivation of the average model……...……. 101
4.2.1.2 Verification by simulation……...… 103
4.2.1.3 Averaging model as a “moving average filter”… 107
4.2.1.4 MOSFET losses…….. 109
4.2.1.4.1 Conduction losses……...… 109
4.2.1.4.1.1 PWM duty ratio……...… 110
4.2.1.4.1.2 Averaged rms currents…..……. 111
4.2.1.4.2 Switching losses…….. 115

4.2.1.5 Diode losses……... 118
4.2.1.5.1 Conduction losses…….. 118
4.2.1.5.2 Switching losses…….. 120
4.2.1.6 Summary of loss equations…….. 120
4.2.1.6.1 Diode…… 120
4.2.1.6.2 MOSFET……... 120
4.2.1.6.3 Total inverter losses……...… 121
4.2.2 Results…….. 123
4.3 Summary 129

5 Parametric Device Study……..... **131**
5.1 Diodes……. 132
5.1.1 Conduction loss parameters……...…... 132
5.1.1.1 Traction drive…… 132
5.1.1.2 Dc power supply……... 138
5.1.2 Switching loss parameters……...……. 139
5.2 MOSFETs……...…… 142
5.2.1 Conduction loss parameters…..…….. 142
5.2.2 Switching loss parameters……...…. 143
5.3 Summary…… 145

6 Conclusions…… **146**
6.1 The main contributions of this study..……..……. 148
6.2. Recommended future work……... 149
6.2.1 Circuits related future work……. 149
6.2.1. Device research……. 150

References…… **152**

Appendix…… **161**
Appendix A Curve Fitting Using Genetic Algorithms…….. 162
A.1 Genetic Algorithm…… 163
A.2 Curve fitting using GA…… 166

Appendix B Induction Machine Simulation……..…… **168**
B.1 Induction motor model…… 169
B.1.1. o-n conversion block…….. 169
B.1.2. abc-syn conversion block…….. 170
B.1.3. syn-abc conversion block…….. 170
B.1.4. Unit vector calculation block…… 171
B.1.5. Induction machine d-q model block…… 171

B.2. Simulation……... 177
B.2.1. Initialization…… 177
B.2.2. Results…….. 177

Appendix C ADVISOR Parameters……..……. 180

Vita…….... 182

LIST OF FIGURES

Figure		Page
2.1	SiC history timeline……..…..	15
2.2	Tetragonal bonding between carbon and silicon atoms……..….	16
2.3	Simplified energy band diagram of a semiconductor……...	19
3.1	pn diode and its structure…….	36
3.2	Schottky diode and its structure……..	38
3.3	Diode ideal *I–V* characteristics……..…	41
3.4	*I–V* characterization circuit……...	42
3.5	Experimental *I–V* characteristics of the Si and SiC diodes in an operating temperature range of 27°C to 250°C……..	43
3.6	PWL diode model (a) Diode symbol and its PWL model (b) *I–V* curve of the PWL model…….…….……...……	45
3.7	The PWL diode model parameters vs. temperature…..……	47
3.8	Conduction losses of Si and SiC diodes at different temperatures…….……..	49
3.9	Typical diode switching waveform…….……	53
3.10	Reverse recovery loss measurement circuit……	57
3.11	Waveforms showing the operation of the chopper in Figure 3.10……..……...	57
3.12	Typical reverse recovery waveforms of the Si pn and SiC Schottky diode (2A/div)..……..	58
3.13	Turn-off waveforms of SiC (a-c) and Si (d-f) diodes, (a)+(d): V_{dc}=100V, (b)+(e): V_{dc}=200V, (c)+(f): V_{dc}=300V (2A/div)……...	59
3.14	Turn-off waveforms in Figure 3.13 in one plot (2A/div)…….	61
3.15	Peak reverse recovery values with respect to the forward current at different operating temperatures……...	63
3.16	Diode switching loss at different operating temperatures……...	65
3.17	The basic structure of a lateral MOSFET…….	69
3.18	The basic structure of a vertical MOSFET……...	69
3.19	Specific on resistance vs temperature (logarithmic plot)…….….	73
3.20	MOSFET capacitances……	75
4.1	Isolated full-bridge step-down dc-dc converter…….	81
4.2	Operation waveforms of the dc-dc converter…….	82
4.3	Simple transient thermal model of a semiconductor device……	87
4.4	SIMULINK model of the dc-dc converter thermal simulation…	87

4.5	Diode losses in the dc-dc converter (20 kHz operation)……..	90
4.6	Diode losses in the dc-dc converter (100kHz operation)……..	90
4.7	Output filter…….	93
4.8	Filter parameters with respect to the switching frequency…..…	95
4.9	Three-phase inverter driving an induction machine load……	98
4.10	Federal Urban Driving Schedule (FUDS)……	99
4.11	Block diagram of the traction drive model…….……	100
4.12	PWM operation waveforms……..	102
4.13	PWM operation in one switching cycle……...	102
4.14	Averaging model explanatory waveforms…….	104
4.15	SIMULINK model developed to verify the averaging model…..	105
4.16	Verification of the averaging model (steady-state) **…….**	106
4.17	Verification of the averaging model (transient)…….	106
4.18	MA filter example for n=8 and n=9……..	107
4.19	Averaging model as a MA filter……...	109
4.20	The switch current waveforms in two switching cycles……...	112
4.21	Triangles defined to simplify (4.50)…….	117
4.22	Equivalent circuit for the conduction losses……...	122
4.23	SIMULINK model of the traction drive thermal simulation……	125
4.24	Total loss profile for a diode and a MOSFET……..	126
4.25	Total losses and the efficiency of the inverter over the FUDS cycle……..	127
4.26	Junction temperature profiles of the diodes and MOSFETs in the three-phase inverter…….	128
5.1	The variation of $f(M\cos\phi)$ with $M\cos\phi$ (a) The denominator and the numerator of $f(M\cos\phi)$ vs. $M\cos\phi$ (b) $f(M\cos\phi)$ vs. $M\cos\phi$…….	134
5.2	The R_D – V_D plane for the traction drive…….	136
5.3	Carrier distribution in a diode during turn-off (a) Linearized carrier density distribution of a diode at different time instants (b) Linearized turn-off current waveform of the diode…..……..	141
B.1	The complete induction machine SIMULINK model……	169
B.2	Dynamic model of an induction machine……...	172
B.3	Implementation of (B.13) in SIMULINK…….	175
B.4	Induction machine dynamic model implementation in SIMULINK……..….	176
B.5	Implementation of (B.18) in SIMULINK…….	177
B.6	Induction machine model initialization file……	178
B.7	Induction machine simulation results…….	179
C.1	ADVISOR parameters used in this study……...	181

LIST OF TABLES

Table		Page
2.1	Physical characteristics of some semiconductors including SiC polytypes [3-5].....	18
3.1	Diode parameters.....	44
3.2	Diode PWL model parameters.....	47
3.3	200 A diode parameters.....	51
3.4	200 A Diode PWL model parameters.....	52
3.5	I_F and I_R data tables.....	62
3.6	The values of the integral in (3.25).....	64
3.7	On resistance values for Si and 4H-SiC at different temperatures.....	72
4.1	Maximum device voltage and currents for different load power and input voltage conditions.....	83
4.2	Required heatsink mass and volume for the dc-dc converter operating at full load and switching at 20 kHz.....	88
4.3	Required heatsink mass and volume for the dc-dc converter operating at full load and switching at 100 kHz.....	88
4.4	Heatsink mass and volume for each device and inverter.....	128
5.1	SiC Diode PWL model parameters and V_D/R_D ratio.....	137
B.1	Induction motor dynamic model equations (flux linkage form).	174
B.2	(B.7-10,18) in state-space form.....	175

Chapter 1

INTRODUCTION

Over the past decade, changes have taken place that have drawn more attention to electric and hybrid electric vehicles. Increasing oil prices and worries of a diminishing oil supply are creating a need for alternatives to traditional gasoline and diesel engines. Consequently, more and more companies in the transportation industry are introducing electric or hybrid electric vehicles. In addition, the military is ready for all electric war ships and more electric fighter planes while various industries are gearing up to convert from all gasoline or all diesel vehicles to all electric or hybrid electric ones. The hurried demand for electric/hybrid electric vehicles (EV/HEV) enhances the significance of the power electronics in these vehicles. Furthermore, the present Silicon (Si) technology is reaching the material's theoretical limits, and cannot meet all the

requirements of the transportation industry. A new semiconductor material, Silicon Carbide (SiC) is ready to overtake Si in transportation applications. The next sections will discuss why this will happen.

1.1. Transportation requirements

Power electronics converters for transportation applications have to comply with strict requirements because of the space and weight limitations and extremely harsh operating conditions. In a vehicle, there is limited space for the electrical and/or mechanical units; therefore, all the units have to be compact, occupying as little volume as possible. Moreover, they are expected to be lightweight so that the weight of the vehicle stays constrained. A lighter vehicle means less load on the engine and/or motor, faster acceleration, and higher efficiency. Higher efficiency results in less fuel or battery charge consumption. Finally, the converters have to be able to function at high temperatures without failure for long times, i.e. they have to be highly reliable, and they must be available at a reasonable price.

As a summary, the general requirements for any power converter in a transportation application are compactness, lightweight, high power density, high efficiency, and high reliability under harsh conditions.

The main focus of this study is hybrid electrical vehicles (HEV), and all of the aforementioned power electronics requirements are also true for them.

1.2. Why not silicon?

All vehicles contain power converters as rectifiers, power supplies, battery chargers, etc. Separating HEVs from conventional vehicles, however, is the electrical traction drive. This drive, as the vital part of an HEV, carries the most power among all the HEV power converters.

All of the electronics in a vehicle must continue to operate under harsh conditions with the most detrimental condition being high temperature. Since heat is generated by the engine, the motor, the semiconductor device losses, and the environment, all of the electronics have to be cooled so that they will continue to perform. Note that the maximum junction temperature limit for most Si electronics is 150°C; therefore, the temperature of the Si chips and power devices should remain under this value. Even then, the variation in the electrical characteristics of Si devices with temperature and time is still a big reliability issue.

Three standard options for cooling the devices are natural air, forced air, or water-cooled heatsinks. However, as the temperature of the environment increases, the cooling capacity of the cooling system decreases. The power rating of the converter determines the type of heatsink to use. For low power converters, bulky natural air heatsinks are sufficient whereas high power converters require the more expensive, but smaller liquid-cooled heatsinks. However, the latter requires a pump to circulate the coolant as well as a radiator and a fan to cool it. A heatsink typically occupies one-third of the total volume for a power converter and usually weighs more than the converter itself. Building electronics that can withstand higher temperatures is one way of decreasing the cooling requirements, size and cost of the converter, but Si devices have reached their theoretical temperature limits.

A major source of heat affecting the vehicular electronics is the heat generated by the semiconductors themselves, especially the power semiconductors. These power devices have losses associated with conducting and switching high currents. The amount of loss depends on the type of power devices utilized. In high power transportation applications, like the traction drive, Insulated Gate Bipolar Transistors (IGBT) and PiN diodes are presently used. Both are bipolar devices and have higher losses compared to their unipolar counterparts like Metal Oxide Semiconductor Field Effect Transistors (MOSFET) and Schottky

diodes. Although, the aforementioned unipolar devices have superior properties compared to bipolar devices, they are not used in traction drives since they do not exist at high power ratings. Building higher voltage rating MOSFETs and Schottky diodes would not be feasible because as the breakdown voltage increases, the device requires a large silicon die area and this results in reduced manufacturing yields and increased costs. For higher breakdown voltages, a material with a higher electric breakdown field is required.

The switching frequency of the devices is also limited due to the heat generated by the devices, primarily the switching losses. Higher frequency operation is preferred because of filtering requirements, less audible noise, and smaller passive components. The outputs of high frequency power converters are smoother, and a small filter would be sufficient enough to filter the harmonics. Additionally, with high frequency the size of the passive components decreases so there is an overall gain in size and weight. Moreover, with higher frequency, the converters could work at an inaudible frequency range, which would be comfortable for the user. While some Si bipolar devices can operate around 20kHz and unipolar Si devices can operate at higher frequencies, the problem is that they do not exist at higher voltage or power ratings.

1.3. Why silicon carbide?

As seen above, increasing the effectiveness of Si to meet the needs of the transportation industry is not viable because it has reached its theoretical limits. However, it is already proven that even the first SiC-based power devices surpass Si's theoretical limits. SiC power devices can work in harsh environments where Si power devices cannot function. SiC power devices, with their close-to-ideal characteristics, offer great performance improvements. Some of the advantages compared with Si based power devices are as follows:

- SiC unipolar devices are thinner, and they have lower on-resistances. At low breakdown voltages (~50V), these devices have specific on-resistances of 1.12μΩ, around 100 times less than their Si counterparts. At higher breakdown voltages (~5000V), this goes up to 29.5mΩ, 300 times less than comparable Si devices. With lower R_{on}, SiC power devices have lower conduction losses; therefore, higher overall converter efficiency is attainable.
- SiC-based power devices have higher breakdown voltages because of their higher electric breakdown field; e.g., Si Schottky diodes are commercially available typically at voltages lower than 300 V, but the first commercial SiC Schottky diodes are already rated at 600 V.
- SiC has a higher thermal conductivity (4.9 W/cm-K for SiC and 1.5 W/cm-K for Si); therefore, SiC power devices have a lower junction-to-case thermal

resistance, $R_{th\text{-}jc}$ (0.02 K/W for SiC and 0.06 K/W for Si); device temperature increase is slower.

- SiC can operate at high temperatures. SiC device operation at up to 600°C is mentioned in the literature. Si devices, on the other hand, can operate at a maximum junction temperature of only 150°C.
- SiC is extremely radiation hard; i.e. radiation does not degrade the electronic properties of SiC; therefore, a SiC converter can be used in aerospace applications decreasing the weight of the vehicle due to reduced radiation shielding.
- Forward and reverse characteristics of SiC power devices vary only slightly with temperature and time; therefore, they are more reliable.
- SiC-based bipolar devices have excellent reverse recovery characteristics. With less reverse recovery current, the switching losses and EMI are reduced, and there is less or no need for snubbers. As a result, there is no need to use soft-switching techniques to reduce the switching losses.
- Because of low switching losses, SiC-based devices can operate at higher frequencies (>20 kHz) not possible with Si-based devices in power levels of more than a few tens of kilowatts.

Although SiC has these advantages compared with Si, the present disadvantages limit its widespread use. Some of these disadvantages are

- Low processing yield because of micropipe defects. The best wafers available have <1/cm^2, but they are more expensive than the typical wafer with <10/cm^2.
- High cost– The first SiC Schottky diodes (Spring 2001) cost about $50 for a 600 V, 4 A Schottky diode (similar Si pn diode <<$1). Recently (Spring 2002) , the prices of SiC Schottky diodes have come down to $7/each.
- Limited availability - only Schottky diodes at relatively low power are commercially available).
- Need for high temperature packaging techniques that have not yet been developed.

These disadvantages are normal considering that SiC technology has not matured, yet. The same disadvantages existed for Si when it was thought that it could replace germanium (Ge), and today few remember the initial processing problems of Si. The advantages already outweigh the disadvantages. As far as the power electronics are concerned, the future will be SiC!

1.4. Other SiC application areas

Some power electronics application areas will benefit from SiC power device development more than others. These areas can be listed as aerospace, power systems, and transportation. The main focus of this study is the transportation

area; therefore, SiC impact on the other two areas will be summarized only briefly.

1.4.1. Aerospace applications

Some of the requirements for a power converter in a spacecraft are small mass, small volume, and high/low temperature operation. If SiC power devices are used, because of their high temperature operation capability and lower losses, there would be mass and volume advantages. In addition to this, SiC power devices are radiation hard, which means that they are less susceptible to the damaging effects of radiation. Therefore, if SiC devices are used there is need for less radiation shielding, which also results in a gain in mass. The discussion on low temperature operation of SiC devices is still going on and there is no clear answer yet.

1.4.2. Power systems applications

With the recent advances, power electronics interfaces to power systems like Static Transfer Switches, Dynamic Voltage Restorers, Static VAR compensators, High Voltage DC Transmission (HVDC), and Flexible AC Transmission System (FACTS) are getting more and more attention. Presently, there are no high voltage/high current single-Si devices available for these applications. Instead, lower rated devices are put in series and parallel. With SiC's high voltage

capability, in the near future it will be possible to replace many Si devices in series and/or in parallel by one SiC power device. This will decrease the device count and the size of these converters. If single power devices can be used, balancing resistors and capacitors can be discarded saving even more space and avoiding voltage balancing and/or current sharing problems. Moreover, because of the high temperature operability and lower losses of SiC power devices, cooling system size will also decrease. Finally, with less reverse recovery, less or no snubbers will be required.

1.5. Outline of the dissertation

The objective of this study is to develop necessary modeling and simulation tools for evaluating the system impact of SiC power devices on a HEV. To do this, first, Si and SiC diodes and MOSFETs will be characterized and modeled. Then, two sample power converters in an HEV will be selected and the advantages of SiC over Si will be quantitatively demonstrated. Finally, a parametric study will show what device parameters need to be modified in order to obtain system specific optimum power devices.

Chapter 2 starts with the history of the SiC compound. Then, its physical and electrical characteristics are discussed. The chapter continues with information on the state-of-the-art SiC devices and their applications. At the end of the

chapter, a summary of "what is already done" and "what needs to be done next" will be given.

Chapter 3 explains the approach used to characterize and model diodes and MOSFETs and compares the performance of Si and SiC diodes and MOSFETs.

Chapter 4 discusses the system modeling approach using the device loss models developed in Chapter 3 and provides results of the system simulations.

Chapter 5 contains a parametric study of SiC diodes and MOSFETs showing what device parameters need improvement to get better results in transportation applications.

Chapter 6 provides conclusions and an overall summary of this work.

Chapter 2

LITERATURE SURVEY

In the previous chapter, the advantages of SiC and SiC-based devices have been summarized briefly. Before going into system level studies, more information on the SiC material and SiC-based devices is required to understand the systems research better. In this chapter, a brief history of SiC research will be given, which will be followed by the details on the physical characteristics of SiC and how these characteristics enhance the power devices. Finally, a summary of previous research will be given and the remaining research work will be discussed.

2.1 History of SiC

Silicon Carbide (SiC) is one of the oldest compound semiconductors in the universe, but it had to wait until the end of the 20th century for its turn to be recognized by the semiconductor community. SiC is almost nonexistent in nature. It is believed that SiC was formed around stars some 4.6 billion years ago [1] and grains have reached the earth on meteorites.

In 1824, a Swedish Chemist, Jöns Jacob Berzelius discovered that there could be a bond between carbon and silicon. This was the first hint in the history to the existence of SiC. SiC still had to wait for the invention of the electric smelting furnace [2] and its application to carbon compounds. Sixty-seven years after Berzelius' discovery, Eugene G. Acheson of Monongahale, Pennsylvania melted a mass of carbon and aluminum silicate. He was trying to produce a diamond-like substance for cutting and polishing purposes. He noticed small, bright blue crystals forming after the mixture cooled down to the room temperature. These crystals were very hard, so they were used for cutting and abrasive purposes. He was expecting a compound of aluminum and carbon instead of silicon and carbon. He called the new compound he found "carborundum" from Al_2O_3, which is called "corundum". Later, he and his coworkers found out that the new

compound was made up of silicon and carbon. SiC is still known as "carborundum".

In 1905, Moissan found natural SiC in meteorites. Because of this discovery, SiC is known to mineralogists as "moissanite" [2].

The first SiC Light Emitting Diode (LED) was made in 1907. However, the research in SiC did not go far until Lely developed his concept of growing higher quality SiC crystals in 1955 [2]. The first SiC conference was held in 1958 in Boston. Soon after Si arrived, almost all the research attention was diverted from SiC to Si. However, during the silicon era there was still some SiC research going on, especially in the former Soviet Union.

Interest in SiC resumed when researchers realized that Si technology had peaked and new semiconductor materials were needed with capabilities beyond that of Si. SiC research accelerated with the founding of Cree Research in 1987 after which SiC wafers were readily available.

SiC history is illustrated on a timeline in Figure 2.1.

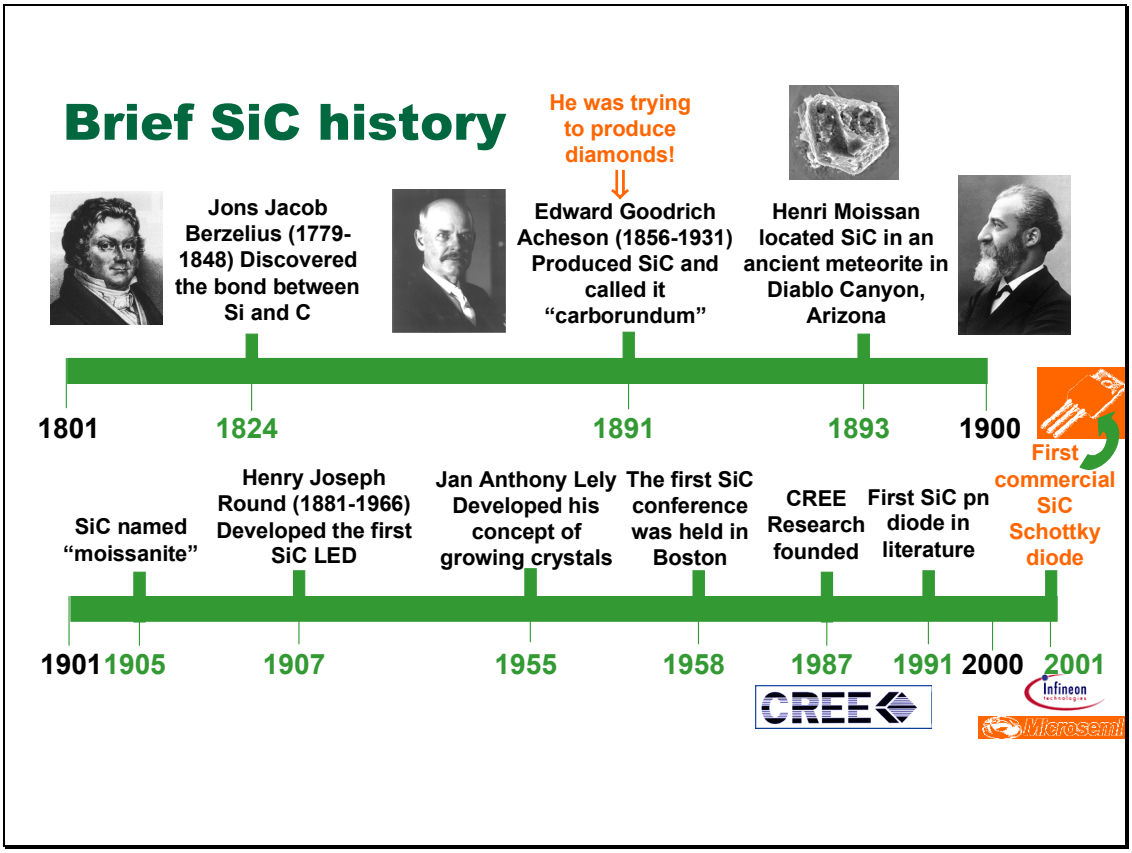

Figure 2.1: SiC history timeline.

2.2 Physical properties of SiC

SiC is a wide bandgap semiconductor with high thermal conductivity, high breakdown electric field strength, high-saturated drift velocity, and high thermal stability. It exists in what are called polytypes. These polytypes are formed by stacking SiC molecules on top of each other in a certain order. Figure 2.2 shows one of these molecules, a carbon atom in the center of a tetragonal shape formed by four silicon atoms bonded to the carbon atom. More than 170 SiC polytypes

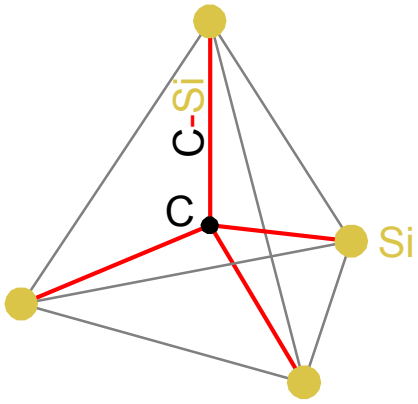

Figure 2.2: Tetragonal bonding between carbon and silicon atoms.

are reported and each of them has different physical properties. The most commonly known polytypes are 3C-SiC, 6H-SiC, and 4H-SiC, but only the last two are commercially available. Since 1994, 4H-SiC has replaced 6H-SiC as the most commonly used SiC polytypes.

The naming convention of the polytypes comes from their repeated stacking order and the shapes they form. 3C corresponds to stacking of three SiC molecules stacked in layers in three different positions A, B, and C and the formed crystal has a cubic (C) shape. The same way 4H has a stacking order of ABAC and the resulting shape is hexagonal (H). Finally, the stacking order of 6H-SiC is ABCACB repeating and this also has a hexagonal shape.

Some physical characteristics of the SiC polytypes and some other competing semiconductors are given in Table 2.1 ([3-5]). The following sections will talk

Table 2.1: Physical characteristics of some semiconductors including SiC polytypes [3-5].

Property	**Units**	**Si**	**GaAs**	**3C-SiC**	**6H-SiC**	**4H-SiC**	**Diamond**
Bandgap, *Eg*	eV	1.12	1.43	2.4	3.03	3.26	5.45
Dielectric constant, ε_r[1]	--	11.9	13.1	9.7	9.66	10.1	5.5
Electric Breakdown Field, E_c	kV/cm	300	400	2120	2500	2200	10000
Electron Mobility, μ_n	$cm^2/V{\cdot}s$	1500	8500	800	500 (⊥ to c axis) 80	1000 (⊥ to c axis)	2200
Hole Mobility, μ_p	$cm^2/V{\cdot}s$	600	400	40	101	115	850
Thermal Conductivity, λ	W/cm·K	1.5	0.46	3.2	4.9	4.9	22
Saturated Electron Drift Velocity, v_{sat}	cm/s	1×10^7	1×10^7	2×10^7	2×10^7	2×10^7	2.7×10^7

[1] $\varepsilon = \varepsilon_r \cdot \varepsilon_o$ where $\varepsilon_o = 8.85\times10^{-12}$ F/m

about these characteristics and their effects on the power devices.

2.2.1 Wide bandgap

In a solid, electrons exist at energy levels that combine to form energy bands. A simplified energy band diagram is shown in Figure 2.3. The top band is called the conduction band and the next lower one is called the valence band. The region between the valence band and the conduction band is called the forbidden band where ideally no electrons exist. Note that, there are more bands lower than the valence band, but these are not so important for this study.

If the electrons in the valence band are excited externally, they can move to the conduction band. In the valence band, they have an energy of E_v, so to move to the conduction band, they need an E_g=E_c-E_v amount of energy where E_g is called the bandgap.

For a conductor, like copper, the forbidden band does not exist and the energy bands overlap. For an insulator, on the other hand, this band is so wide that the electrons need a lot of energy to move from the valence band to the conduction band. For the semiconductors, the forbidden gap exists and is smaller than that of an insulator.

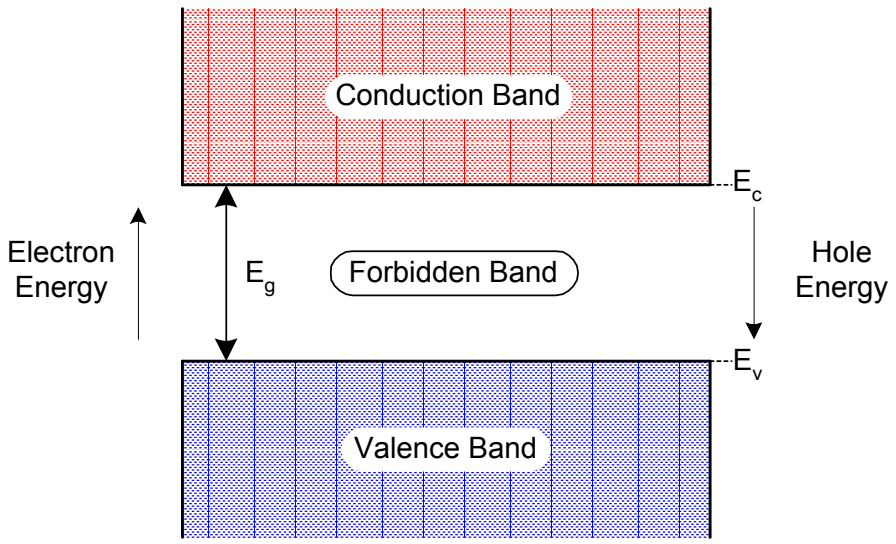

Figure 2.3: Simplified energy band diagram of a semiconductor.

Some semiconductors are classified as wide bandgap semiconductors because of their wider bandgap. Si has a bandgap of 1.12 eV and is not considered a wide bandgap semiconductor. The bandgap of SiC polytypes range from 2.39 eV for 3C-SiC to 3.33 eV for 2H-SiC; therefore, all SiC polytypes are classified as wide bandgap semiconductors.

Wide bandgap semiconductors have the advantage of high temperature operation and more radiation hardening. As the temperature increases, the thermal energy of the electrons in the valence band increases. At a certain temperature, they have sufficient energy to move to the conduction band. This is an uncontrolled conduction that needs to be avoided. The temperature at which this happens is around 150°C for Si. For SiC, the bandgap energy is higher;

therefore, electrons in the valence band need more thermal energy to move to the conduction band. This intrinsic temperature for SiC is around 900°C.

The above reasoning is also true for radiation hardening. Radiation energy can also excite an electron like the thermal energy and make it move to the conduction band.

As a result of the wide bandgap, devices built with SiC can withstand more heat and radiation without losing their electrical characteristics. They can be used in extreme conditions where Si-based devices cannot be used.

2.2.2 High electric breakdown field

Electric breakdown field (E_c) of SiC is five times that of Si because of its wider bandgap. With this high electric breakdown field ($1.5\text{-}4\times10^6$) much higher doping levels can be achieved; thus, the device layers can be made thinner than Si at the same breakdown voltage levels. The resulting SiC devices are thinner than their Si counterparts, and they have smaller on-resistances.

For example, the breakdown voltage (BV) of a pn diode is expressed in [6] as follows:

$$BV \approx \frac{\varepsilon_r E_c^2}{2qN_d} \tag{2.1}$$

where q is the charge of an electron and

N_d is the doping density

Using the semiconductor parameters for Si and SiC in Table 2.1, this expression can be simplified as follows:

$$BV^{Si} \approx \frac{2.96\times10^{19}}{N_d} \tag{2.2}$$

$$BV^{4H-SiC} \approx \frac{135.11\times10^{19}}{N_d} \tag{2.3}$$

From (2.2) and (2.3), two conclusions can be derived:

1. The breakdown voltage of 4H-SiC pn power diode is 46 times higher than that of its Si counterpart with the same doping density.
2. To achieve the same breakdown voltage, the 4H-SiC pn diode can be doped 46 times more heavily provided that the material is non-degenerate.

Moreover, the width of the depletion layer at breakdown can be expressed as [6]:

$$W(BV) \approx \frac{2BV}{E_c} \tag{2.4}$$

For a non-punch-through pn diode, the width of the depletion layer should be less than the width of the drift region. Therefore,

$$W_d > \frac{2BV}{E_c} \tag{2.5}$$

Using the electric breakdown field values for Si and 4H-SiC from Table 2.1, the drift thickness of the drift region for these two semiconductors are found as

$$W_d^{Si} = 6.67 \times 10^{-6} BV \tag{2.6}$$

$$W_d^{4H-SiC} = 0.91 \times 10^{-6} BV \tag{2.7}$$

It can be concluded from (2.6) and (2.7) that for the same BV, a 4H-SiC pn diode is seven times thinner than its Si counterpart.

On the other hand, the specific on-resistance associated with the drift layer of a power MOSFET is given below [7]:

$$R_{on,sp} = \frac{4(BV^2)}{\varepsilon_s (E_c)^3 \mu_n} \tag{2.8}$$

where BV is the breakdown voltage,

ε_s is the dielectric constant,

E_c is the electric breakdown field, and

μ_n is the electron mobility.

The denominator in (2.8) is called the Baliga figure of merit (BFM), which gives a measure of the specific on-resistance of a MOSFET's drift region. The higher the BFM is, the smaller is the drift region resistance. Comparing a Si MOSFET to a 4H-SiC MOSFET, for the same breakdown voltage, $R_{on,sp}$ for a Si device (ε_s=11.9, E_c=3×10^5 V/cm, μ_n=1500 cm^2/V·s) is 223 times more than that of a similar SiC device (ε_s=10.1, E_c=22×10^5 V/cm, μ_n=1000 cm^2/V·s).

As the breakdown voltage increases, more doping can be applied to SiC than Si, so the specific on resistance ratio between Si and SiC increases further. At low breakdown voltages (~50V) it is around 100 and at higher breakdown voltages (~5000), it might go up to 300 [7]. Note that for lower voltages (<1kV), channel resistance dominates the drift resistance, so the total on resistance of a SiC MOSFET is not too different from that of a Si MOSFET. With lower $R_{on,sp}$, at high voltages, SiC power devices have lower conduction losses; therefore, higher efficiencies.

In addition to these, the storage of the minority carriers (Q_{rr} in diodes) is also reduced because of the thinner layers. Therefore, reverse recovery losses of SiC diodes decrease allowing higher frequency operation.

2.2.3 *High saturated drift velocity*

High frequency capability of a semiconductor material is directly proportional to its drift velocity. The drift velocity of SiC polytypes (2×10^7) is twice the drift velocity of Si (1×10^7); therefore, it is expected that SiC-based power devices could be switched at higher frequencies than their Si counterparts. Moreover, higher drift velocity allows charge in the depletion region of a diode to be removed faster; therefore, the reverse recovery current of SiC diodes is smaller and the reverse recovery time is shorter.

2.2.4 *High thermal stability*

As explained earlier, because of the wide bandgap of the SiC material, SiC-based semiconductor devices can operate at high temperatures. In addition to this, SiC has another thermal advantage not mentioned before and that is its high thermal conductivity. 4H-SiC has more than three times higher thermal conductivity (4.9 W/cm-K) compared to Si (1.5 W/cm-K); therefore, considering (2.9), junction-to-case thermal resistance, $R_{th\text{-}jc}$, of a 4H-SiC device is more than three times lower.

$$R_{th-jc} = \frac{d}{\lambda A}\ , \tag{2.9}$$

where λ is the thermal conductivity,

d is the length, and

A is the cross-sectional area.

Lower $R_{th\text{-}jc}$ means that heat generated in a SiC-based device can more easily be transmitted to the case, heatsink, and then to the ambient.

2.3 SiC power devices

The number of SiC power device publications has been increasing rapidly in the last few years. There are many examples of 4H-SiC and 6H-SiC PiN diodes, Schottky diodes, IGBTs, thyristors, BJTs, various MOSFETs, GTOs, MCTs, MTOs, etc. in kV range [8] with reduced on-resistances. However, except for some of the diodes, the reported devices are all experimental devices with very low current ratings. Only a few papers have been published on power converter applications of SiC diodes [9] and none on the applications of controlled switches. As of April 2002, three companies have advertised the commercial availability of SiC Schottky diodes, Infineon (600V up to 12A or 300V up to 10A), Microsemi (200V/400V/600V, 1A/4A), and Cree (600V up to 10A). Considering that the first commercially available diode was out just last year, this is a great improvement.

Some of the SiC power devices reported in the literature will be discussed in the following subsections.

2.3.1 High voltage devices

With their close-to-"ideal" switch properties, unipolar devices are preferred over bipolar devices in power electronics applications. Majority carrier devices (or unipolar devices) such as MOSFETs, MESFETs, JFETs, and Schottky diodes are faster than minority carrier devices (or bipolar devices) such as PiN diodes, BJTs, IGBTs and SCRs. The controlled unipolar devices have negligible switching losses and also have the advantage of low gate drive requirements. The Schottky diodes, on the other hand, have lower voltage drops and reverse recovery losses.

Presently, for Si at voltages higher than a certain value (~300V) it is more cost effective to use bipolar devices because of their higher current densities than unipolar devices. This voltage value is ten times [10] higher in SiC devices (3 kV) than Si devices. Thus, SiC unipolar devices are expected to replace Si bipolar devices in the 300-3000V range power applications; however, over 3kV, bipolar devices regain the control. In this voltage range, SiC bipolar devices still have an edge over their Si counterparts.

A 1.75 kV 4H-SiC Schottky diode is reported in [11] with an on-resistance of 5 $m\Omega \cdot cm^{2.}$ Two higher voltage SiC Schottky diodes in the literature are a 3kV [12] diode and a 4.9 kV diode [8]. The latter is built by Purdue University and has a specific resistance of 43 $m\Omega \cdot cm^2$. It is argued that these diodes have high current

densities; however, because of their small size they can just carry low currents. Only if they were paralleled they would be capable of carrying higher currents. For comparison purposes, please note that the highest current-rated commercially available Si Schottky diode has a current rating of 600A at 100V and the highest voltage-rated one is rated at 600V and 25A. Even the first commercially available SiC Schottky diodes from Infineon were rated at 300V and 600V [13] with a current rating of 10A extremely close to the ratings of the state-of-the-art Si Schottky diode.

Kansai and Cree, on the other hand, reportedly produced a 19.2 kV PiN diode. Some other 12-19 kV PiN diodes are also demonstrated in [14]. These diodes are high voltage diodes but they carry low currents.

Unfortunately, no SiC controlled switches are commercially available, yet. However, some papers report experimental prototypes of controlled SiC switches at higher blocking voltages compared with their Si counterparts. MOSFETs are of special importance because they are unipolar devices. Si MOSFETs are usually available for low voltage (<300V) applications. SiC MOSFETs, on the other hand, are demonstrated in the kV range. A 1.4 kV UMOSFET is reported in [8] with a specific on-resistance of 15.7 $m\Omega \cdot cm^2$. Another MOSFET, a DIMOSFET is reported to be at 1.85 kV with an $R_{on,sp}$ of 46

$m\Omega \cdot cm^2$ in [9]. Note that the theoretical specific on-resistance for Si is 180 $m\Omega \cdot cm^2$ and for 4H-SiC it is 0.3 $m\Omega \cdot cm^2$. It is promising to see that SiC power MOSFETs even in their infancy have surpassed Si's theoretical limits.

Some research has also been conducted for other power devices like a 1.8kV SiC BJT and a 3.1 kV GTO reported in [8].

2.3.2 High temperature operation

As discussed earlier, SiC power devices can operate at high temperatures. SiC MOSFETs have been reported to function at as high as 650°C [16]. Moreover, a SiC UMOSFET was shown to work at 450°C and a thyristor (700V, 6A) at 350°C [17]. This is quite an improvement compared with 150°C operation temperature for Si power devices.

The high temperature SiC power devices are still in experimental stage because there are no high temperature contacts or packaging available yet. The only commercially available SiC Schottky diodes have a rated operating temperature of 175°C [13].

2.3.3 High frequency operation

SiC power devices have reduced switching losses and they can operate at high temperatures. As a result of these two properties, SiC power devices can operate at higher switching frequencies. The switching frequency of Si power devices is usually limited to less than 20 kHz for power levels of more than a few tens of kilowatts. As the power of the converter increases, the switching frequency decreases because of the increased losses. Switching frequencies of over 100kHz are possible for SiC power devices. A striking example in the literature is a 700V, 4.2 kW 4H-SiC thyristor that reportedly [10] could be switched at frequencies up to 250 kHz. Normally, Si thyristors can be operated at only a few kHz.

2.3.4 High reliability

Some reliability studies of SiC PiN diodes are done in [18] and [19]. Both consider mainly the static characteristics of these diodes. They show that in the long-term, SiC PiN diodes show excellent reverse voltage characteristics. The forward voltage drop, however, increases in time. No comparison with Si PiN diodes is given. No other directly reliability related sources are found in the literature.

Some other papers report that the static and dynamic characteristics of SiC devices do not change much with temperature. In [20], the reverse recovery

waveforms of a 1500V 0.5 A rated SiC diode is shown at different temperatures. The peak reverse current of the SiC diode stays at 0.4 A while that of the 1000V 1A rated Si PiN diode increases from 1.5A to 2.7 A as the temperature changes from 25°C to 225°C. Furthermore, the reverse recovery time of the SiC diode stays at 20 ns while that of the Si diode increases from 50 ns to 100 ns. Similar results are also given in [21].

2.4 SiC power device applications

Recently, more and more SiC power device application papers are being published. The first papers published were dc-dc converter applications where Si diodes were replaced by their SiC counterparts [20, 22-26]. The only inverter application up-to-date with SiC diodes is described in [27].

[20, 22, 23] demonstrate the increase in the efficiency of the dc-dc converter just by replacing Si diodes with SiC diodes. The full-load efficiency is reported to be 88% with SiC diodes and 82% with Si diodes. They also show the decrease in the electromagnetic interference (EMI). This is because of the smaller reverse recovery current of the SiC diode, which is the major contributor to EMI. It is also noted that SiC diodes work at 100kHz switching frequency without any

problems but several commercially available Si diodes were destroyed at comparable frequencies. Similar results have been reported in [24].

In [25], it is reported that the performance of Si and SiC diodes is similar at low voltage and low temperature (100°C) applications. However, as the voltage and the temperature increase, the advantages of SiC diodes become more pronounced. Trivedi et al. come to the same conclusion in [25] through high temperature testing of 3A Si and SiC devices.

The inverter application in [27] with Si diodes replaced by their SiC counterparts shows efficiency improvements, especially at higher temperatures. The reverse recovery loss of the Si diode is reported to be 90μJ per switching at 201°C, while that of the SiC diode was found to be 12.6μJ at 205°C.

Some other recent publications compare the Si and SiC diodes in hard and soft switching applications ([28], [29]) and power correction applications ([30], [31]).

2.5 The next steps

As discussed in this chapter, there are many papers on SiC devices, and the number is increasing rapidly. Most of these papers are written by physicists and

device researchers; therefore, they are all about very low power device testing and characterization and comparison with Si devices where the devices have high current densities but low currents. These do not depict the whole story as far as high power converters are concerned.

There are also some papers ([20], [22]-[31]) on power electronics applications of SiC diodes. Most of these papers focus on dc-dc converters (except for [27]), and they do not talk about the overall system advantages of using SiC devices.

None of the papers found in the literature convey a clear picture as to what the global impacts of SiC power devices would be on a power electronics system. Furthermore, none of them specifically target the transportation industry or explain the potential impact of SiC devices in this area. Therefore, this dissertation is here to bridge this gap.

Chapter 3

DEVICES

The analysis of the system impact of SiC power electronics requires system level studies, which include both simulation and experimental work. For the experimental work, power converters have to be built and tested; however, with the present SiC technology, the power devices with the required power ratings are not available. This increases the importance of realistic simulation studies for which practical device models are needed. This chapter will focus on two power switches, power diodes and MOSFETs, and will discuss the approaches to model these devices.

SiC diodes are commercially available at much lower current ratings than required for the transportation applications because of the processing problems.

For a typical application, 200A diodes are required, but the commercially available diodes are only rated at 10A; therefore, 200A diode models cannot be derived experimentally. However, it is possible to model lower current rated diodes experimentally and then to scale the model to obtain high current diode models.

The other device of interest in this study is the power MOSFET. SiC MOSFETs are presently not commercially available; therefore, it is not possible to develop experimental models. However, theoretical models can be developed using the parameters available in the literature.

In the first part of this chapter, both an experimental and a theoretical model of 10A diodes including high temperature effects are derived; then, these models are scaled to represent 200A diodes. Using the experimental test results, the characteristics of a Si and a SiC power diode are compared to show the device advantages of SiC diodes over Si diodes. While testing the high temperature effects on the diodes, their high temperature durability is also tested.

In the second part of the chapter, a theoretical model of a power MOSFET is developed using some equations and parameters from the literature. Using the

theoretical models, the advantages of a SiC power MOSFETs are evaluated with respect to a Si MOSFET.

3.1 Diodes

Diodes are the simplest power devices and they are major components of all power converters. There are mainly two types of diodes used in power converters: pn diodes and Schottky diodes. For low power converters, Schottky diodes are preferred because they are faster than pn diodes; they have low on-state voltages, and low reverse recovery losses. However, for high power applications requiring diodes rated over 300V, Si Schottky diodes are not available; therefore, Si pn diodes are used. The first commercial SiC Schottky diodes are available at voltage ratings of 600V. As the SiC technology matures, SiC Schottky diodes will be available in the kilovolt range, and they will replace Si pn diodes of similar voltage rating.

The following sections first present information on these diodes and develop experimental models to be used in system simulations.

3.1.1 Types of diodes

3.1.1.1 pn Diodes

A pn diode is made by joining a p-type semiconductor and an n-type semiconductor. For the device to withstand high voltages the n-type region is divided into a highly doped n^+ and a lightly doped n^- regions as shown in Figure 3.1. The n^- region is also called the "drift region". When a reverse voltage is applied, the depletion layer forms in this layer. If it touches the n^+ layer, then the diode is called the "punch-through diode". Normally, for "non-punch-through diodes" this layer is confined in the drift region. Depending on the breakdown voltage rating of the diode, the drift region can be made wider or narrower.

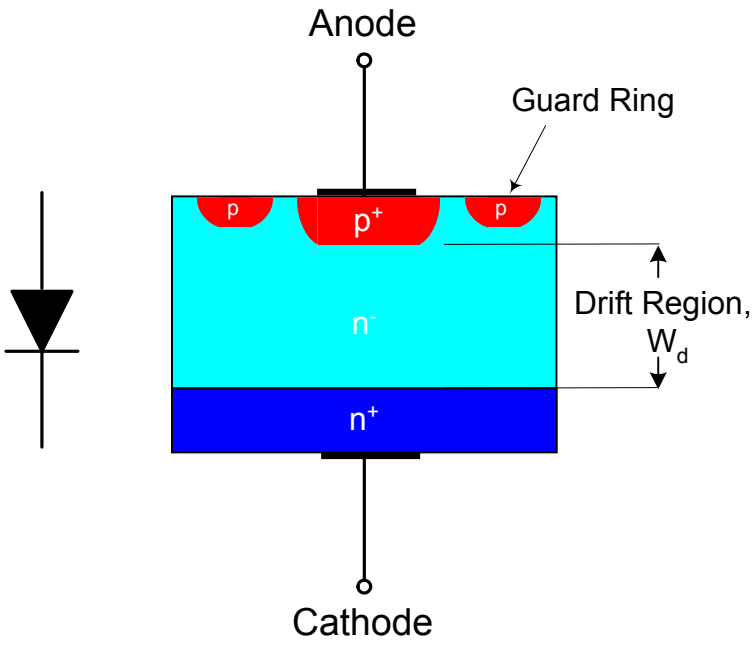

Figure 3.1: pn diode and its structure.

To better picture the dimensions and the doping levels of a diode, consider the diode given in [6] and shown in Fig. 3.1 as an example where the highly doped p^+ region is 10μm wide and has a doping density of $N_a = 10^{19}\,\text{cm}^{-3}$. The n^+ region, on the other hand, is wider at 150μm but has the same doping density. The width of the lightly doped ($N_d = 10^{14}\,\text{cm}^{-3}$) drift region depends on the breakdown voltage of the diode as explained in Chapter 2.

The pn diode is a minority carrier (or bipolar) device, so it has a large amount of stored charge when it is on. This results in a reverse recovery current when the device turns off, which slows the device and increases the switching losses especially at higher switching frequencies.

Because of their bipolar nature, pn diodes exhibit a negative temperature coefficient, which makes it difficult to parallel them. An interesting consequence of the negative temperature coefficient is that as the temperature increases, the conduction loss of a pn diode decreases, but, as will be seen later in this chapter, the switching losses increase even more making the decrease in the conduction loss seem trivial.

The modeling sections will present more information on the conduction and switching characteristics of the pn diodes and the next chapter will discuss the

effects of the parameters on the device and system performance.

3.1.1.2 Schottky diodes

A metal to semiconductor junction as seen in Figure 3.2 forms a Schottky diode; therefore, it is simpler than the pn diode and actually it is the simplest of all the semiconductor switches. Although the most common form of Schottky diodes are formed by metal to n-type semiconductor junction, others formed by a metal to p-type semiconductor junction are also used.

The Si Schottky diodes have lower on-state voltages (0.3 - 0.4V) than Si pn diodes (0.7) but they have higher reverse leakage currents. To prevent the reverse

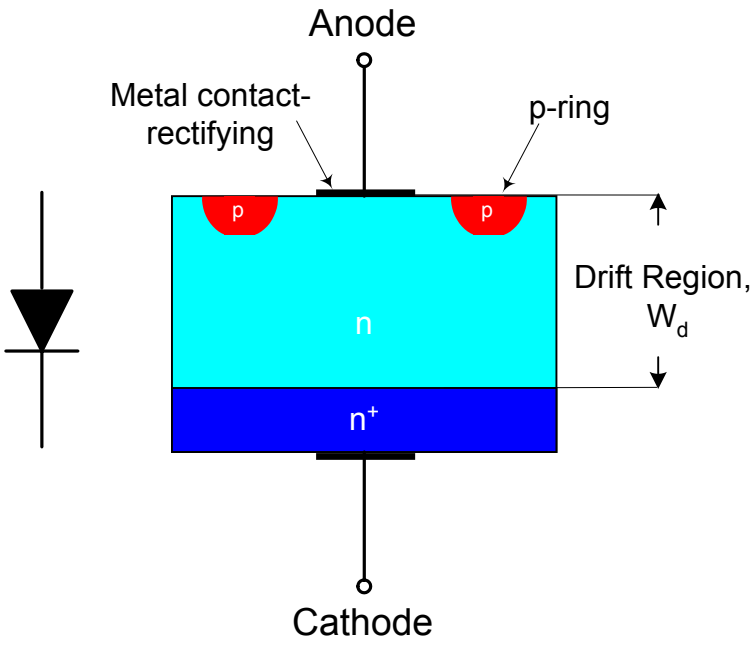

Figure 3.2: Schottky diode and its structure.

leakage currents, p-rings can be used, which form parasitic pn diodes in the Schottky diode to block the reverse leakage currents but at an expense of reverse recovery currents. Theoretically, Schottky diodes are majority carrier devices, so they do not have stored minority carriers when they are on, which means that they do not have reverse recovery problems and are faster than pn diodes. However, with the introduction of the p-ring, they show some unwanted reverse recovery characteristics. In addition to the reverse recovery, a high frequency ringing is observed during turn-off, which is caused by the capacitance of the diode forming a series resonant circuit with the parasitic inductance of the circuit. An *RC* snubber circuit in parallel to the diode can suppress this ringing.

Another advantage of the Schottky diodes is that they have a positive temperature coefficient as opposed to the negative temperature coefficient of the pn diode so that unlike the pn diode they can be paralleled easily.

Because of the advantages of the Schottky diodes over the pn diodes, they are preferred devices for power applications; however, because of their present low power range they can be utilized only in low power applications. This is already changing with the introduction of commercial SiC Schottky diodes at higher power levels.

3.1.2 Loss Modeling

System studies described in the next chapter need loss models of the Si and SiC devices. In this section, the diode loss model will be derived using experimental testing and characterization.

3.1.2.1. Conduction losses:

The conduction loss of a diode is related to the static characteristics of the device and is a strong function of the diode series resistance. Therefore, it is required to find the *I–V* characteristics of the diodes to estimate their conduction losses.

3.1.2.1.1. Ideal diode I-V characteristics

The ideal diode characteristics shown in Figure 3.3 can generally be represented by the following equation:

$$I = I_s \left(e^{q(V - IR_s)/nkT} - 1 \right) \tag{3.1}$$

where I_s is the saturation current,

q is the magnitude of electron charge (1.601×10^{-19}C),

k is the Boltzmann's constant (1.3805×10^{-23} J/K),

T is the temperature in Kelvins,

n is the ideality factor,

V is the voltage across the diode,

I is the current through the diode, and

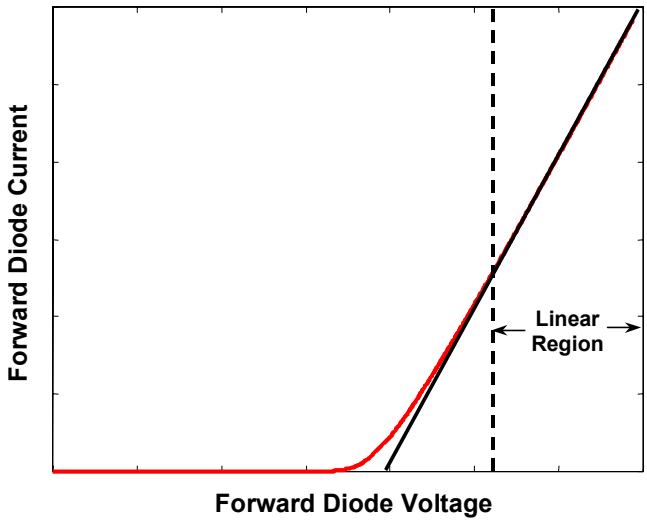

Figure 3.3: Diode ideal I–V characteristics

R_s is the diode series resistance

Note that for the signal diodes, the series resistance is usually ignored because the signal diode is not used to carry power. Power diodes, however, usually operate in the linear region (Figure 3.3) of the diode I–V characteristics where the series resistance is more dominant because of the higher level of current they are carrying. For this reason, the power devices can be modeled using piece-wise linear models with good accuracy.

First, it is required to find the I–V characteristics of the diodes. For signal diodes and BJTs, there are instruments, which measure the I–V characteristics; however, these instruments are scarcely available in high power range. Therefore, it is necessary to build custom circuits for this test. The circuit in Figure 3.4 is an

example of such a circuit. The following procedure is used to obtain the diode *I–V* characteristics using this circuit:

1. Vary V_{dc} so that the current through the diode varies in steps.
2. Note the current value and measure the voltage drop at each current step.
3. Stop when the current level is around 6A (because of the diode and power supply current limitations)
4. Repeat the above steps at different temperatures up to 250°C (because of oven limitation) or until the diodes burn

The data obtained are plotted in Figure 3.5. The following observations can be made from this figure:

1. The forward voltage drop of the SiC diode is higher than that of the Si diode for the same current. This is expected because of SiC's wider bandgap. It also implies that the conduction losses of SiC diodes might be higher.

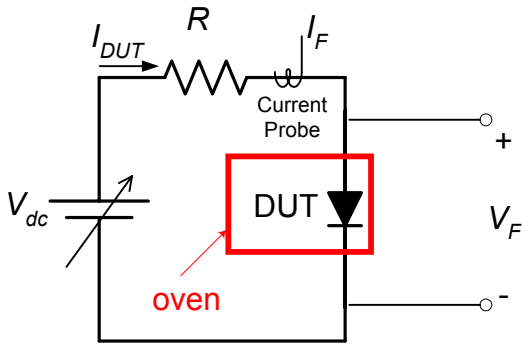

Figure 3.4: *I–V* characterization circuit.

2. The high temperature behavior of the two diodes is different. As the temperature increases, the forward characteristics of the Si diode changes severely while that of the SiC diode stays confined to a narrow region.
3. The pn diode (negative) and the Schottky diode (positive) have different polarity temperature coefficients, and that is why the slope of the curve at higher currents is increasing in the Si diode case and decreasing in the SiC diode case with the temperature increase.

3.1.2.1.2. Finding the diode parameters

Diode parameters, I_s, R_s, and n can be found from the experimental data through a curve fitting method. There are many curve-fitting methods available but here,

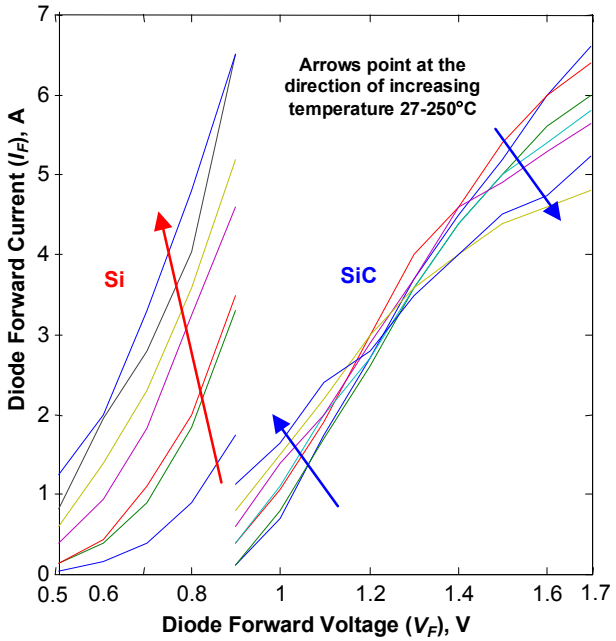

Figure 3.5: Experimental I–V characteristics of the Si and SiC diodes in an operating temperature range of 27°C to 250°C.

a Genetic Algorithm (GA-) based approach is developed. GA is a search-based computational model that solves optimization problems by imitating genetic processes and the theory of evolution. It imitates biological evolution by using genetic operators like reproduction, crossover, mutation, etc.

For curve fitting, it is required to find the equation best matching the data curve. The data are already available from the test results and the equation in this case is the ideal diode equation in (3.1). More information on the GA method and its application in this study can be found in Appendix A.

The diode parameters found using this GA technique are listed in Table 3.1. Some of the values seen in this table seem to be inconsistent; this is because of the measurement error during experimentation. Please note that the measurement

Table 3.1: Diode parameters.

	SiC Schottky Diode			**Si pn Diode**		
T_{oven}, °C	R_s, mΩ	I_s, μA	n	R_s, mΩ	I_s, μA	n
27	121.3	0.28	2.000000	139.104	2.74	1.969872
61	133.5	1.59	1.999999	81.322	35	1.999998
82	132.3	6.79	1.994021	64.824	18.7	1.843186
106	146.8	11.8	1.999849	67.173	93.5	1.788652
129	147.5	39.5	1.999628	66.198	575	1.999997
150	167.8	111	1.405057	54.112	849	1.954359
174	162.8	106	1.986808	45.166	1670	1.952035
200	169.6	182	1.859660	50.227	3540	1.900935
250	210.5	441	1.994792	51.327	13800	1.999695

error will propagate with the calculations based on these data, so there will be more tables with irregular entries in the rest of this section.

3.1.2.1.3. Piece Wise Linear (PWL) model of a power diode

The piece-wise linear (PWL) diode model is an approximation of a diode by a voltage drop and a series resistor as shown in Figure 3.6. The parameters of the PWL model are found directly from the *I–V* characteristics of a diode. First, a line is drawn along the linear region of the diode *I–V* characteristics as shown in Figures 3.3 and 3.6. The x-intercept of this line is the PWL voltage drop, V_D and the inverse of the slope of this line is the series resistance R_D.

Then, the PWL diode model can be represented as:

$$V_D = \begin{cases} 0 & V_F \le V_D \\ R_D \cdot I_D & V_F \ge V_D \end{cases} \tag{3.2}$$

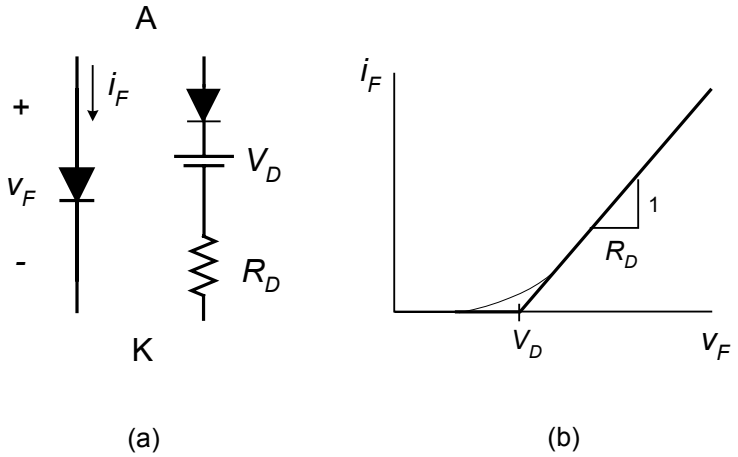

Figure 3.6: PWL diode model **(a)** Diode symbol and its PWL model **(b)** *I–V* curve of the PWL model.

The PWL model parameters are found using GA curve fitting and the resulting parameters are listed in Table 3.2 and plotted in Figure 3.7 with respect to temperature.

Again using curve fitting, an equation for each parameter as a function of temperature is found:

$$V_D^{SiC} = 0.2785e^{-0.0046T} + 0.7042 \tag{3.3}$$

$$R_D^{SiC} = -0.1108e^{-0.0072T} + 0.2023 \tag{3.4}$$

$$V_D^{Si} = 0.3306e^{-0.0103T} + 0.5724 \tag{3.5}$$

$$R_D^{Si} = 0.2136e^{-0.0293T} + 0.0529 \tag{3.6}$$

where T is in °C. These are also plotted in Figure 3.7.

3.1.2.1.4. Calculating conduction losses

The voltage drop on the diode and the series resistance are the sources of a diode's conduction losses. These losses can be expressed as:

$$P_{cond} = I_{D,av} \cdot V_D + I_{D,rms}^2 \cdot R_D \tag{3.7}$$

where V_D and R_D are the PWL parameters found earlier.

Table 3.2: Diode PWL model parameters.

	SiC Schottky Diode		Si pn Diode	
T_{oven}, °C	R_D, mΩ	V_D, V	R_D, mΩ	V_D, V
27	121.6	0.93	139.3	0.80
61	134.0	0.91	82.5	0.72
82	133.3	0.87	65.7	0.75
106	147.7	0.9	68.3	0.68
129	147.7	0.93	67.9	0.67
150	168.6	0.82	55.7	0.67
174	164.2	0.88	47.0	0.65
200	171.1	0.82	52.0	0.60
250	211.1	0.71	53.6	0.58

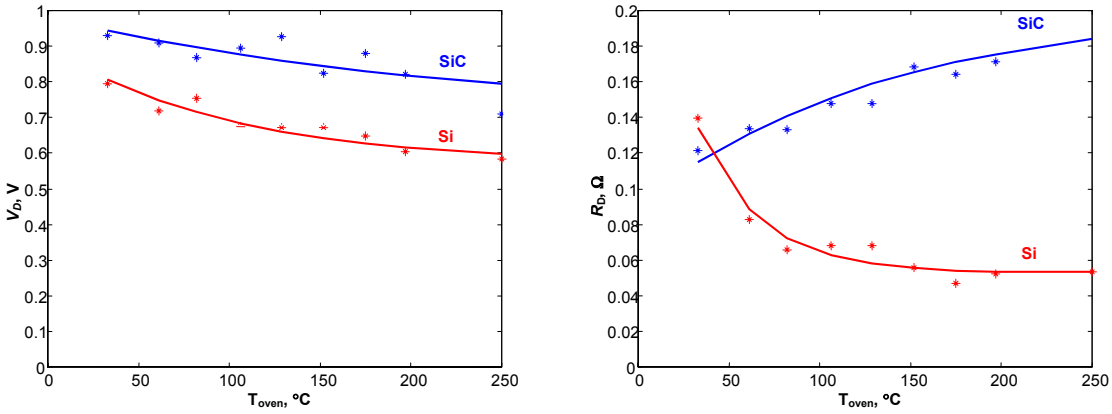

(a) **(b)**

Figure 3.7: The PWL diode model parameters vs. temperature.

When a dc current I_{DC} is applied, then both the average current and rms current are equal to the dc current and (3.7) becomes

$$P_{cond} = I_{DC} \cdot V_D + I_{DC}^2 \cdot R_D \tag{3.8}$$

From (3.8), it is clear that resistive losses dominate the conduction losses for the dc operation especially at higher current values.

To calculate the conduction losses of a Si diode at different temperatures, (3.5) and (3.6) are applied to (3.8). The results are plotted in Figure 3.8a. As expected, the conduction losses decrease with the temperature increase, because both R_D and V_D decrease.

The same calculation is done for the SiC diode using equations (3.3) and (3.4). The results are plotted in Figure 3.8b. This time the losses increase with temperature because V_D is decreasing with temperature but R_D is increasing and as mentioned before R_D is more dominant at higher currents.

Superimposing the waveforms of Figures 3.8a and 3.8b, Figure 3.8c is obtained. It is observed that above 55 °C, the SiC diode has more losses than the Si diode. This statement seems to be contradicting all that is said earlier about SiC power devices; however, everything will be clearer after the switching losses are calculated.

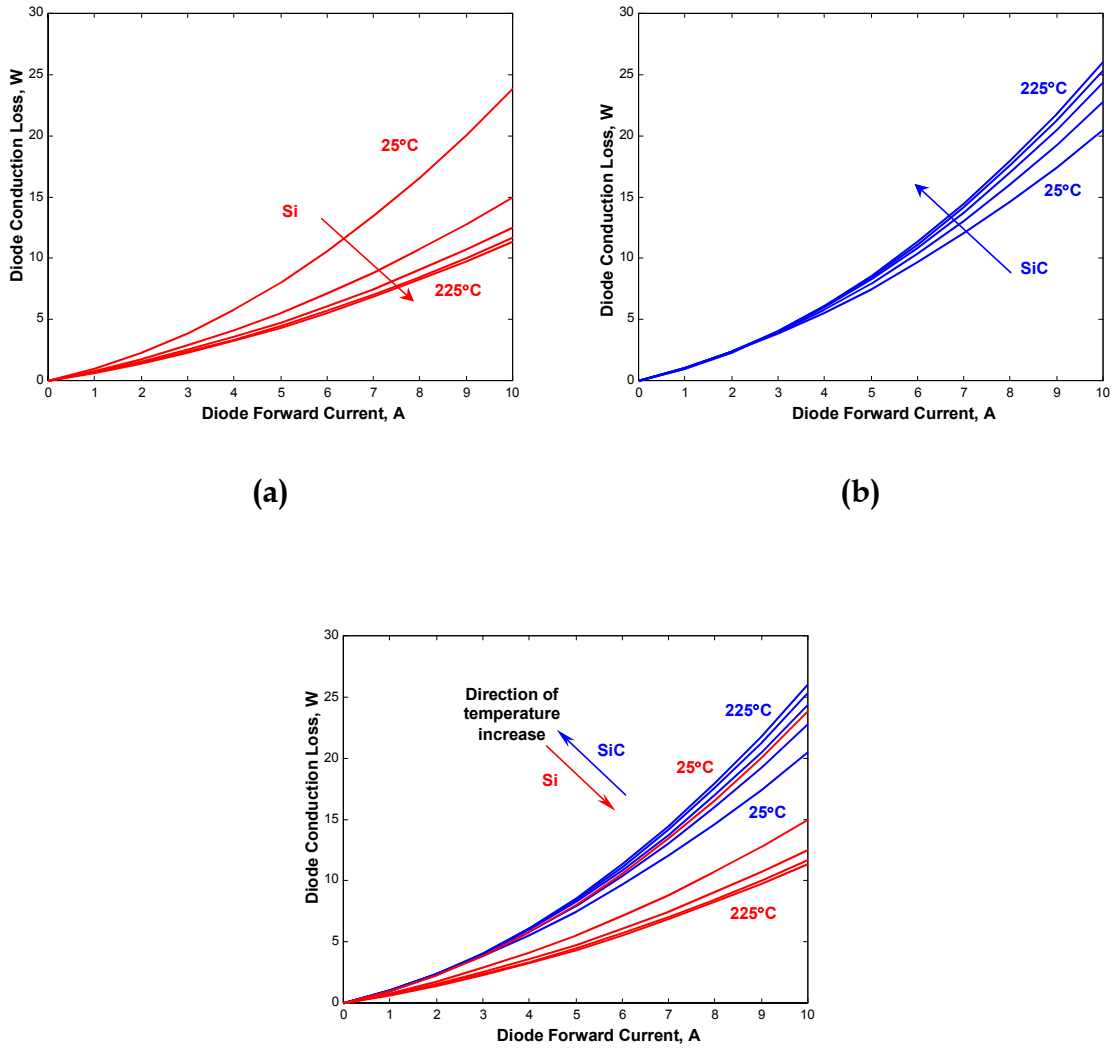

Figure 3.8: Conduction losses of Si and SiC diodes at different temperatures.

3.1.2.1.5. Conduction losses of a 200A diode

Most power electronics applications require devices with higher current ratings than the ones in this study; however, these devices are not currently available. In spite of this, the higher current devices can be modeled by scaling the models of the lower rated devices. For example, a 200A SiC diode can be formed by assuming that 20 10A diodes are paralleled. The *I-V* characteristics of 20 diodes in parallel are conventionally obtained by adding the *I-V* characteristic of all the diodes. In this case, the diodes are identical; therefore, multiplying the current values of the *I-V* characteristics would give the representation of the *I-V* characteristics of 20 diodes in parallel.

The method suggested in this study assumes the 20 diodes combined to represent one diode. Therefore, the changes in paralleling these devices are incorporated in one diode equation.

Considering (3.1), two parameters seem to be affected from paralleling the diodes, I_s and R_s. The final 200A diode has an area of 20 times the original diodes and I_s varies directly with the area; therefore, increasing the area 20 times means increasing I_s 20 times. On the other hand, R_s is inversely proportional with the area; therefore, the 200 A diode will have 20 times less R_s.

Then for a 200A diode, (3.1) becomes

$$I = 20 \times I_s \left(e^{q\left(V - I\frac{R_s}{20}\right)/nkT} - 1 \right) = I_s' \left(e^{q(V - IR_s')/nkT} - 1 \right) \tag{3.9}$$

where $I_s' = 20 I_s$ and $R_s' = R_s / 20$.

Table 3.3 lists the 200A diode parameters. The diode PWL parameters for the 200A diodes are obtained using the procedure in the previous subsection, and Table 3.4 shows these parameters.

R_D and V_D for 200A diodes can be approximated as exponential functions of temperature like (3.3) - (3.6) to be used in computer simulations

Table 3.3: 200A diode parameters.

	SiC Schottky Diode			**Si pn Diode**		
T_{oven}, **°C**	R_s, **mΩ**	I_s, **μA**	n	R_s, **mΩ**	I_s, **μA**	n
27	3.386	0	1	9.545	277	1.999001
61	7.757	151	1.999997	4.332	774	2
82	8.55	843	1.997918	3.083	817	1.999956
106	7.329	402	2	2.881	3613	1.979946
129	7.985	1704	2	2.637	6487	1.982204
150	9.444	4855	1.997722	3.004	3759	1.591954
174	9.418	6399	1.999983	2.516	52374	2
200	10.567	45478	2	2.463	94926	2
250	9.824	16287	1.711025	2.256	72541	1.715328

Table 3.4: 200A Diode PWL model parameters.

	SiC Schottky Diode		Si pn Diode	
T_{oven}, °C	R_D, mΩ	V_D, V	R_D, mΩ	V_D, V
27	4.204	1.07	10.759	0.56
61	9.418	0.63	5.819	0.55
82	10.306	0.56	4.865	0.57
106	8.852	0.68	4.872	0.50
129	10.028	0.59	4.682	0.50
150	11.469	0.55	4.726	0.45
174	11.660	0.55	04.792	0.40
200	11.772	0.50	3.542	0.45
250	12.081	0.48	4.552	0.37

$$V_D^{SiC} = 0.35e^{-0.0065T} + 0.43 \tag{3.10}$$

$$R_D^{SiC} = -0.012e^{-0.013T} + 0.013 \tag{3.11}$$

$$V_D^{Si} = 0.3e^{-0.0065T} + 0.34 \tag{3.12}$$

$$R_D^{Si} = 0.011e^{-0.018T} + 0.0035 \tag{3.13}$$

where T is in °C.

3.1.2.2. Switching losses:

Diode switching losses consist of the turn-on, turn-off, and reverse recovery loss. The most dominant of these losses is the reverse recovery loss. The rest of them are negligible; therefore, only the reverse recovery losses will be considered in this study. Figure 3.9 shows typical "exaggerated" switching waveforms of a diode.

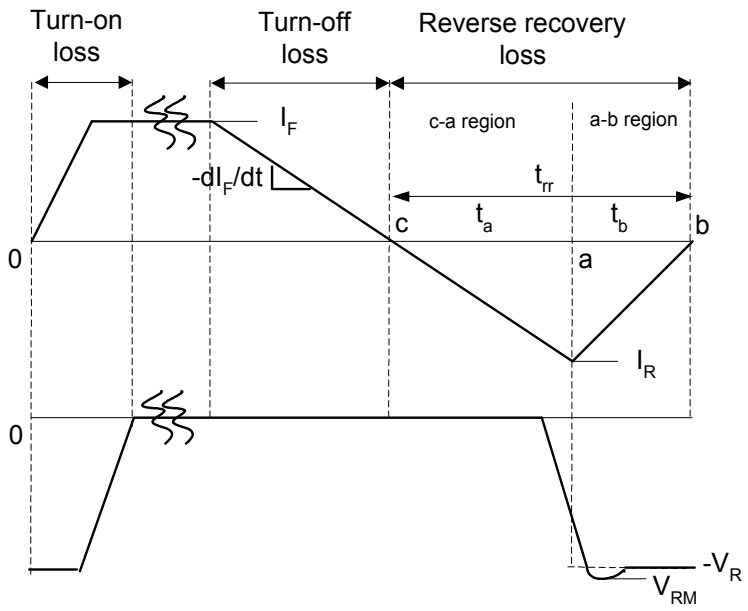

Figure 3.9: Typical diode switching waveform.

In the following sections, first an expression for the reverse recovery loss of a diode is derived to show the parameter dependence of this loss, and then the reverse recovery loss is calculated experimentally.

3.1.2.2.1. Derivation of the switching loss expression

The reverse recovery loss equation is derived using Figure 3.9. First, the energy loss during reverse recovery needs to be calculated.

$$E_{rr} = \int_{c}^{b} v_d \, i_d \, dt \tag{3.14}$$

The reverse recovery waveform can be divided into two regions denoted by the c-a region and a-b region. The voltage across the diode is almost zero in the c-a region; therefore, the loss in this region can be ignored. In the a-b region,

however, there is full voltage applied to the diode. There is also an overshoot in this region but it can be ignored for simplicity. Then, the energy loss equation becomes

$$E_{rr} = \int_a^b \left(-V_R\right) \cdot I_R \cdot \left(-1 + \frac{t-a}{t_b}\right) dt = \frac{V_R I_R t_b}{2} \quad (3.15)$$

where V_R is the applied reverse voltage,

I_R is the peak reverse recovery current, and

t_b is the snap-off time.

The energy loss multiplied by the switching frequency gives the reverse recovery loss. Therefore,

$$P_{rr} = f_s \frac{V_R I_R t_b}{2} \quad (3.16)$$

This equation shows that the reverse recovery loss is directly proportional to the reverse blocking voltage, peak reverse recovery current, and the snap-off time. The reverse blocking voltage is usually constant for an application. The peak reverse recovery current and snap-off time are device specific parameters but they cannot always be found in the device datasheets. It would have been easier to calculate the losses if (3.16) was a function of the parameters found on any diode datasheet.

To express (3.16) in terms of datasheet parameters, it is necessary to express t_b and I_R in terms of the snappiness factor, S and the reverse recovery time, t_{rr} that are readily available on datasheets.

Snappiness factor is defined as,

$$S \equiv \frac{t_b}{t_a} \tag{3.17}$$

and the reverse recovery time is

$$t_{rr} = t_a + t_b . \tag{3.18}$$

(3.17) and (3.18) when solved together result in the following t_a and t_b equations in terms of S and t_{rr}

$$t_b = \left(\frac{S}{S+1} \right) t_{rr} \tag{3.19}$$

and

$$t_a = \left(\frac{1}{S+1} \right) t_{rr} \tag{3.20}$$

I_R can also be calculated in terms of S and t_{rr}, as follows,

$$I_R = \frac{dI_F}{dt} t_a \tag{3.21}$$

(3.20) in (3.21) gives

$$I_R = \frac{dI_F}{dt} \frac{1}{S+1} t_{rr} . \tag{3.22}$$

Then,

$$P_{rr} = f_s \frac{V_R}{2}\left(\frac{dI_F}{dt}\right)\frac{1}{S+1}t_{rr}\frac{S}{S+1}t_{rr} = f_s \frac{V_R}{2S}\left(\frac{dI_F}{dt}\right)\left(\frac{St_{rr}}{S+1}\right)^2 . \quad (3.23)$$

The reverse recovery loss of a diode can be calculated using (3.23); however, the result will not be right at different temperatures because (3.23) does not include the temperature dependent effects on the parameters. For a more accurate solution, high temperature testing is required.

3.1.2.2.2. Finding switching losses experimentally

A buck chopper with an *R-L* load is built as shown in Figure 3.10. Main switch *Q* is switched at 1 kHz with a 25% duty ratio. The operation waveforms of the chopper are shown in Figure 3.11. When *Q* is on, the current builds through the load and *Q*. After *Q* is turned off, the load current starts freewheeling through the diode. In this mode, it decreases until *Q* is turned on again.

The diode turn-off waveforms are shown in Figure 3.12 where it can be seen that the peak reverse recovery current of the Si diode is more than three times that of the SiC diode, and so is the reverse recovery loss.

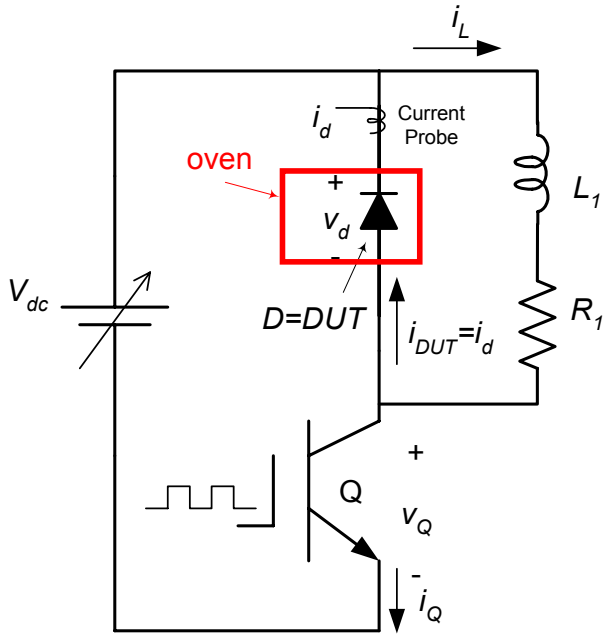

Figure 3.10: Reverse recovery loss measurement circuit.

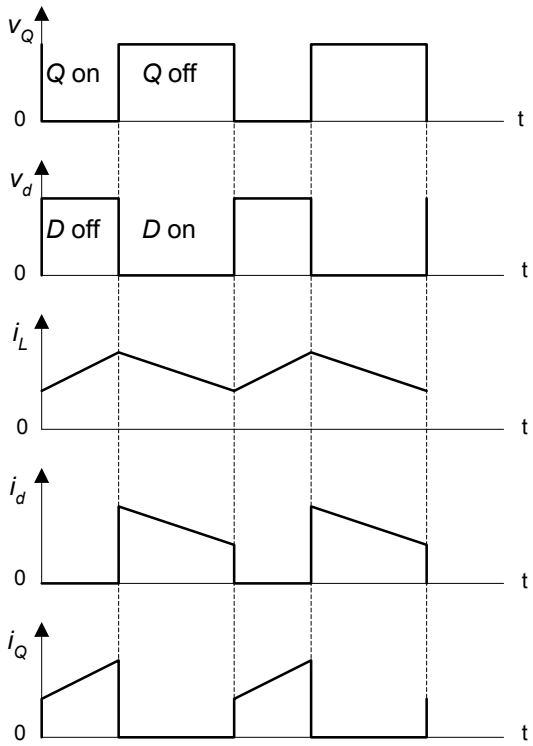

Figure 3.11: Waveforms showing the operation of the chopper in Figure 3.10.

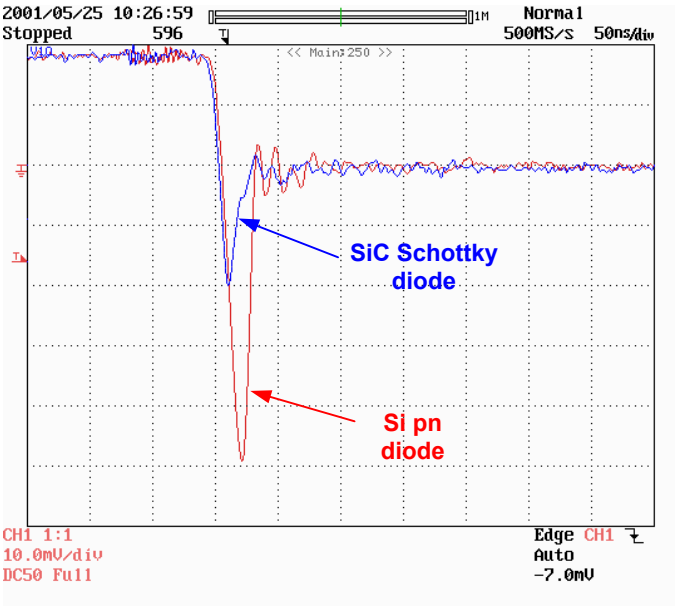

Figure 3.12: Typical reverse recovery waveforms of the Si pn and SiC Schottky diode (2A/div).

Two tests are done using this setup. For the first one, V_{dc} is increased in steps and the turn-off waveforms are observed. The results are plotted in Figure 3.13. As the dc voltage increases, the forward current increases, and the peak reverse recovery current and loss for each diode increase. This increase is smaller for the SiC diode than for the Si diode. A comparison can be seen in Figure 3.14 where all the turn-off waveforms shown in Figure 3.13 are plotted on the same graph.

Note that the peak reverse recovery current of the SiC diode even at 300 V is smaller than that of the SiC diode at 100 V.

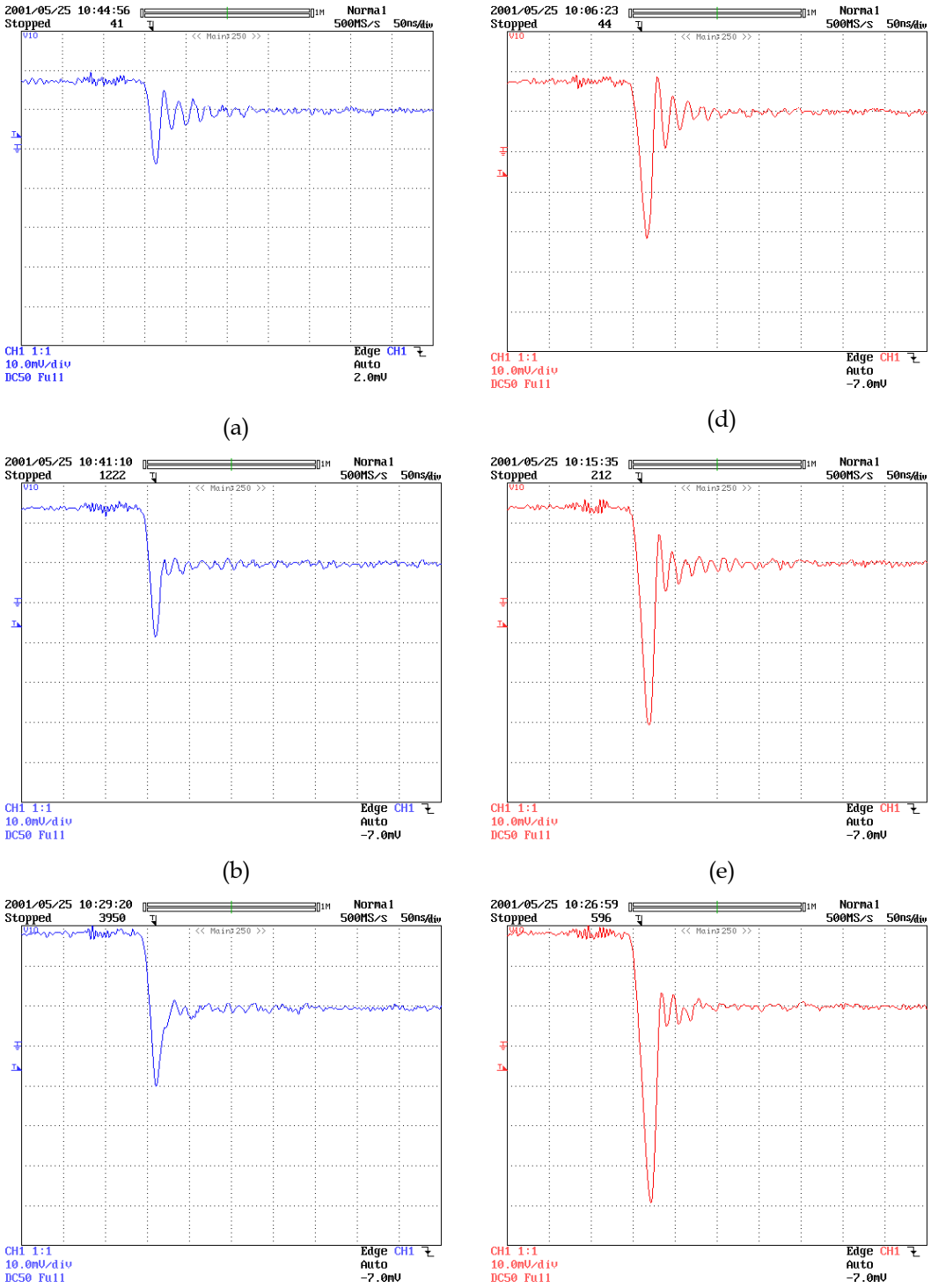

Figure 3.13 : Turn-off waveforms of SiC (a-c) and Si (d-f) diodes, (a)+(d): V_{dc}=100V, (b)+(e): V_{dc}=200V, (c)+(f): V_{dc}=300V (2A/div).

This test was done at room temperature; therefore, it is not enough to characterize the diodes totally in the whole temperature range. It is required to test them at higher temperatures. For this reason, a second test using the same setup is required. This time, the diodes are kept in a temperature-controlled oven and the test is repeated using the following procedure:

1. Keep the oven off, so that the diode is at room temperature.
2. Adjust V_{dc} to 20 V.
3. Measure the peak reverse recovery current, I_R and the integral of the reverse recovery current over the reverse recovery time.
4. Increase V_{dc} by 10 V and do the same measurement in Step 3. Continue until the current limit of the power supply is reached.
5. Turn the oven on and set the oven temperature to 50°C and repeat steps 2 to 4.
6. Increase the oven temperature in steps of 50°C and repeat steps 2 to 4 until the diode gets damaged.

The test was over at 150°C and I_F=4.5A for the Si diode and at 250°C and I_F=4A for the SiC diode. This shows how the SiC diode can operate at higher temperatures compared with its Si counterpart. Note that on the Infineon SiC diode datasheet, its operating temperature rating was 175°C, but it worked even at higher temperatures.

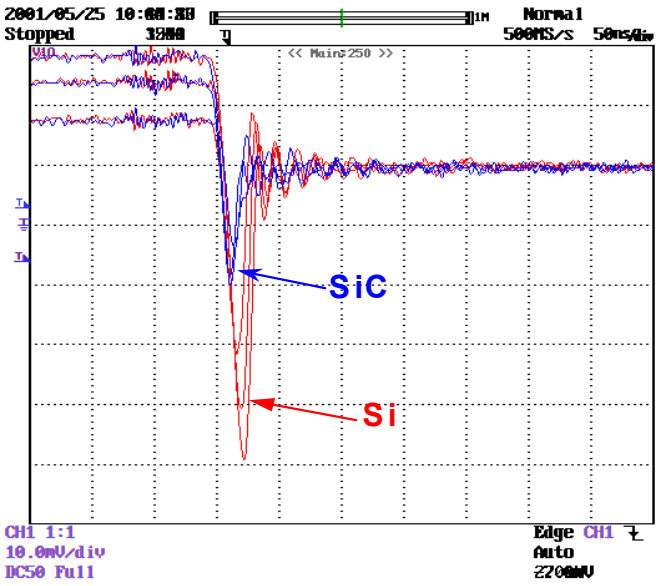

Figure 3. 14: Turn-off waveforms in Figure 3.13 in one plot (2A/div).

Table 3.5 lists the I_F and I_R values for the Si and SiC diodes obtained experimentally. I_R is plotted against I_F in Figure 3.15. Some observations made from this figure are as follows:

- Peak reverse recovery current of the Si diode is more than twice that of the SiC diode at room temperature. The difference increases with temperature and is around eight times at 151°C.
- Peak reverse recovery current of the SiC diode varies with I_F (0.208A at I_F=1A and 0.833A at I_F =4.6A) but does not change at all with temperature.
- Peak reverse recovery current of the Si diode varies greatly with I_F (0.5A at I_F =0.9A and 2.6A at I_F =4.6A) and temperature (0.5A at room temperature with a I_F =0.9A but it is 1.5A with the same I_F at 151°C).

Table 3.5: I_F and I_R data tables.

	SiC I_F, A						Si I_F, A			
V/T_{oven}	**27**	**61**	**107**	**151**	**200**	**250**	**27**	**61**	**107**	**151**
20	1	1	1	1	1	1	0.9	1	1	1.1
30	1.4	1.4	1.5	1.5	1.5	1.5	1.5	1.6	1.6	1.6
40	1.9	2	2	2	2	2	2	2.1	2.1	2.1
50	2.4	2.4	2.4	2.4	2.5	2.5	2.3	2.5	2.5	2.6
60	2.8	2.8	2.8	2.8	2.8	2.8	2.8	2.9	2.9	2.9
70	3	3.1	3	3.1	3.1	3.2	3	3.1	3.2	3.3
80	3.2	3.3	3.2	3.3	3.3	3.3	3.3	3.5	3.4	3.5
90	3.5	3.6	3.4	3.6	3.6	3.5	3.5	3.7	3.8	3.8
100	3.8	3.9	3.8	3.9	3.9	3.8	3.8	4	4	4
110	4.2	4.1	4	4	4.1	×	4.4	4.2	4.3	4.4
120	4.6	4.3	4.3	4.3	4.3	×	4.6	4.4	4.5	4.5

	SiC I_R, A						Si I_R, A			
V/T_{oven}	**27**	**61**	**107**	**151**	**200**	**250**	**27**	**61**	**107**	**151**
20	0.208	0.208	0.208	0.208	0.208	0.208	0.500	0.625	1.04	1.500
30	0.291	0.333	0.291	0.292	0.292	0.291	0.625	1.042	1.500	2.040
40	0.375	0.375	0.375	0.375	0.375	0.375	1.040	1.375	1.958	2.625
50	0.458	0.417	0.417	0.417	0.458	0.458	1.290	1.792	2.375	3.125
60	0.541	0.458	0.458	0.542	0.500	0.500	1.625	2.2500	2.792	3.583
70	0.625	0.525	0.542	0.583	0.542	0.583	1.916	2.500	3.042	4.125
80	0.666	0.583	0.583	0.625	0.625	0.625	2.000	2.917	3.458	4.200
90	0.708	0.708	0.667	0.625	0.708	0.666	2.125	3.2500	3.625	4.600
100	0.75	0.750	0.667	0.708	0.75	0.708	2.460	3.500	4.083	5.170
110	0.791	0.750	0.792	0.750	0.791	×	2.460	3.667	4.167	5.660
120	0.833	0.750	0.833	0.833	0.833	×	2.60	3.917	4.292	6.830

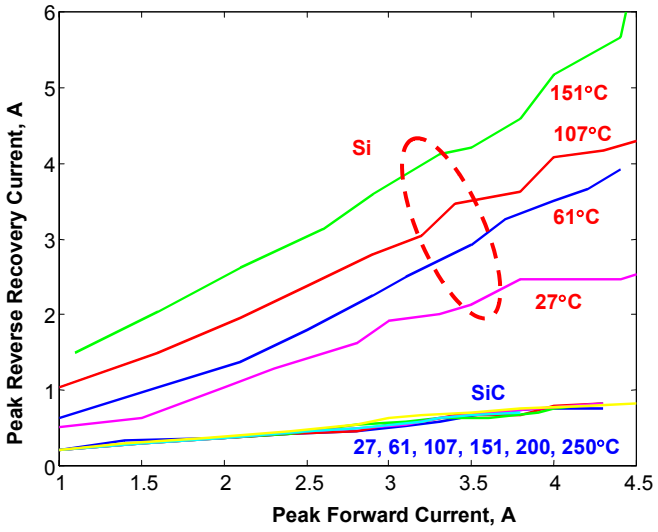

Figure 3.15: Peak reverse recovery values with respect to the forward current at different operating temperatures.

Note that, there are some irregular data in Table 3.5, too. The reason for this is the instrumentation measurement error.

The second set of data obtained experimentally is the integral of the reverse recovery current over t_{rr}, which is tabulated in Table 3.6 and can be used to calculate the switching losses.

First, consider the energy loss equation (3.19), which gives the reverse recovery loss when multiplied by the switching frequency.

$$P_{rr} = f_s \int_c^b v_d \, i_d \, dt \tag{3.24}$$

Table 3.6: The values of the integral in (3.25).

	SiC (×10⁻⁹ A·s)						Si (×10⁻⁹ A·s)			
V/T_{oven}	**27**	**61**	**107**	**151**	**200**	**250**	**27**	**61**	**107**	**151**
20	37.5	36.7	32.2	23.4	30.5	21	47.5	35.8	64.9	129
30	42.1	43	45.5	45.9	36	41.3	60.5	56.2	90.8	174
40	44.2	50.3	52.3	48.3	40.7	55.8	77.1	77.1	121	202
50	67.1	60.6	70.2	64	55.7	64	90.9	108	137	226
60	67.7	70	70.7	70.7	60	77.3	103	122	155	243
70	77	79.9	73.7	74.2	71.7	80.3	123	141	161	271
80	86.1	84	85.6	84.5	80	90.3	131	160	179	297
90	90	91	85.9	87.3	85	92.2	143	174	192	303
100	91.3	92.3	90.8	89.5	93.3	104	150	180	207	325
110	103	96.4	96.1	93.1	96.1	×	169	191	212	342
120	111	99.6	111	99	103	×	180	209	220	422

Then, assume that the diode voltage rises very fast during turn-off, then $v_d=V_R$ during the a-b region in Fig. 3.9 and (3.24) becomes

$$P_{rr} = f_s V_R \int_a^b i_d \, dt \tag{3.25}$$

The switching loss can be calculated by multiplying the data in Table 3.6 by the switching frequency and the reverse blocking voltage. The results for a 20 kHz, 300V operation are plotted in Figure 3.16 where it is seen that the switching losses change almost linearly with the diode forward current.

To model the switching losses of a diode, the data in Table 3.6 can be linearly approximated and expressed as

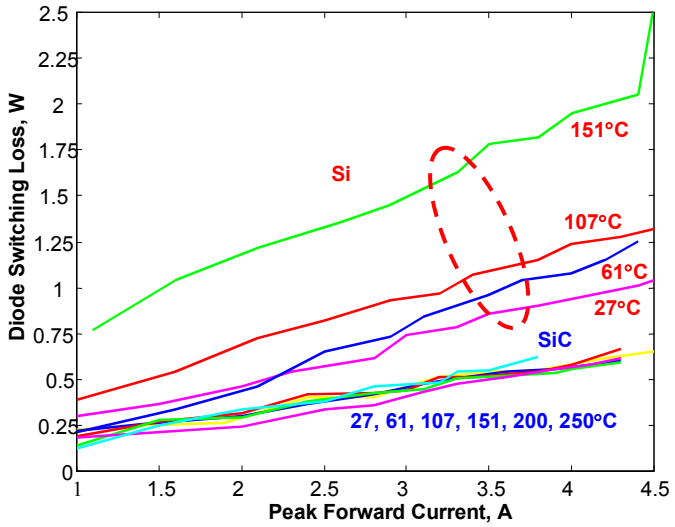

Figure 3.16: Diode switching loss at different operating temperatures.

$$\int_a^b i_d \, dt = \alpha \cdot I_F + \beta \tag{3.26}$$

where α and β are constants.

For Si α and β are temperature dependent and are expressed as

$$\alpha = 3.5\times10^{-8} + 2.5\times10^{-13} \cdot T^{2.31} \tag{3.27}$$

$$\beta = 1.25\times10^{-8} + 2.3\times10^{-15} \cdot T^{3.53} \tag{3.28}$$

where T is in °C.

For SiC, however, the reverse recovery data do not change much with temperature, then α=2.167×10^{-8} and β=2.33×10^{-8}.

Inserting (3.26) into (3.25) the reverse recovery loss is calculated.

$$\begin{aligned} P_{rr} &= f_s \cdot V_R \cdot \int_a^b i_d \, dt \\ &= f_s \cdot V_R \cdot (\alpha \cdot I_F + \beta) \\ &= f_s \cdot V_R \cdot \alpha \cdot I_F + f_s \cdot V_R \cdot \beta \\ &= \alpha' \cdot I_F + \beta' \end{aligned} \tag{3.29}$$

For V_R=300V and f_s=20kHz as in Fig. 3.16, the reverse recovery loss expression can be found by multiplying α and β by $V_R \cdot f_s$=300×20000=6×10^6 and obtaining α' and β'.

$$\alpha' = f_s \cdot V_R \cdot \alpha = 0.21 + 1.5 \times 10^{-6} \cdot T^{2.31} \tag{3.30}$$

$$\beta' = f_s \cdot V_R \cdot \beta = 0.0748 + 0.138 \times 10^{-7} \cdot T^{3.53} \tag{3.31}$$

where T is in °C.

Thus, P_{rr} for any V_R and f_s can be found by multiplying α and β by the $V_R \cdot f_s$ product and inserting α' and β' in (3.29) replacing α and β, respectively.

3.1.2.2.3. Switching losses of a 200A diode

The switching losses for a 200A diode can be calculated by assuming that twenty 10A diodes are connected in parallel. This assumption is based on the fact that device designers sometimes parallel lower current rated devices in one package to get a device with higher current handling capability. With this assumption, the

switching losses of the 200A diode can be calculated simply by multiplying the losses of the original diode by 20. The diode switching loss vs. peak forward current plot of a 200A diode would be the same as the plot in Fig. 3.16, if plotted, with both of the axes values multiplied by 20.

The switching loss curves in Figure 3.16 vary almost linearly with temperature; therefore, in the computer simulations, these losses can be represented by their linear approximation as in (3.29) and using the same α' and β' values.

$$P_{rr}^{200A} = 20 \cdot \left(\alpha' \cdot \frac{I_F}{20} + \beta' \right) \tag{3.32}$$

where the loss of one diode is calculated and the result is multiplied by the number of diodes.

This modeling procedure is not just developed for diode characterization purposes. As will be explained in the next chapter, the models developed here will be implemented in SIMULINK to obtain more realistic system simulation results.

3.2. MOSFETs

MOSFETs are widely preferred power devices in low power applications because they can be operated at high frequencies with relatively low loss switching

behavior. They are majority carrier devices; therefore, they do not have stored charge and can switch rapidly without a reverse recovery or a tail current.

Commercially available MOSFETs are most common at voltages less than 300 V because of the rapid increase in the conduction losses with blocking voltage. They do not have high current ratings either, but because of their positive temperature coefficient, they can be paralleled easily for higher current handling capability. However, usually for higher power applications greater than a few kW, IGBTs are used. This is bound to change with the introduction of commercial SiC MOSFETs in the near future.

3.2.1. Types of MOSFETs

There are many types of MOSFETs available in the literature such as UMOSFET, DMOSFET, VMOSFET, etc. However, the most general classification of MOSFETs depends on the direction of the current conduction - lateral MOSFETs and vertical MOSFETs. In the lateral MOSFET shown in Figure 3.17, the drain and the source are on the same side of the wafer, so the current flows horizontally when the MOSFET turns on. In the vertical MOSFET shown in Figure 3.18, however, the drain and the source are on opposite sides of the wafer, so the current flows vertically when the MOSFET turns on.

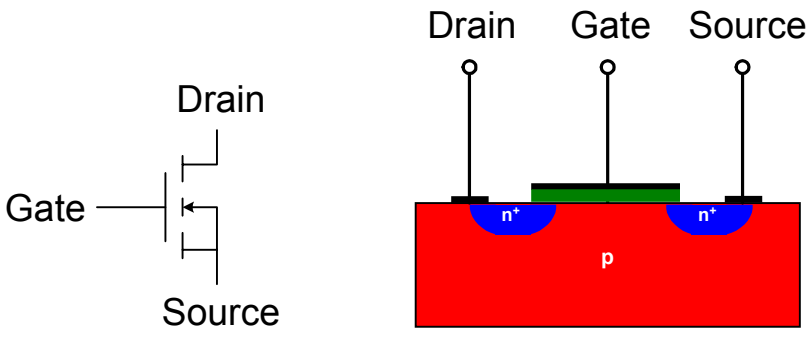

Figure 3.17: The basic structure of a lateral MOSFET.

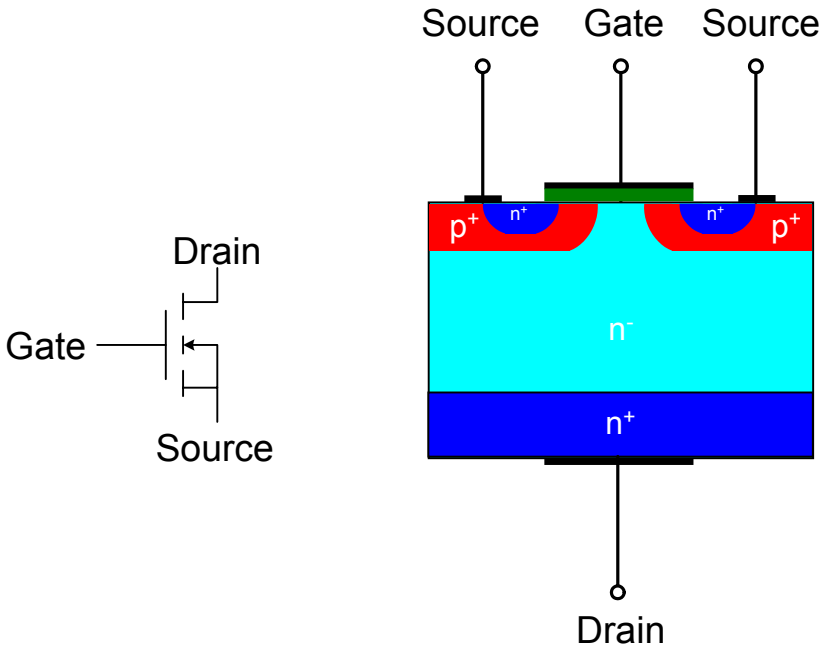

Figure 3.18: The basic structure of a vertical MOSFET.

For high voltage blocking, the thickness of the vertical MOSFET and the length of the lateral MOSFET has to be increased. At higher blocking voltages, the required area of a lateral MOSFET gets too large for an efficient production of the device; therefore, for high voltage applications, vertical MOSFETs are preferred.

3.2.2. *Loss Modeling*

MOSFETs, like diodes have two kinds of losses, conduction losses and switching losses. The conduction losses of a MOSFET, unlike the diode case, consist of only resistive losses. In addition to this, the switching losses are also different from the diode case, in the sense that there is no reverse recovery associated with the MOSFET; therefore, the switching losses consist only of turn-on and turn-off losses. For this study, there were no SiC MOSFETs available to develop an experimental model; so the model here will be a theoretical, physics-based one.

3.2.2.1. Conduction losses

The conduction losses of a MOSFET depend only on the on-resistance of the MOSFET; therefore, the conduction loss expression is as simple as

$$P_{cond,Q} = I_{Q,rms}^2 \cdot R_{DS,on}. \tag{3.33}$$

$R_{DS,on}$ depends on the specific on resistance of the material. In [7], the following values for $R_{on,sp}$ in room temperature are stated for Si and 6H-SiC MOSFETs.

At 300°K for a 1 cm^2 device $R_{on,sp}$ = 0.18Ω for Si

and $R_{on,sp}$ = 0.61x10^{-3} Ω for 6H-SiC

No values are given for 4H-SiC. This dissertation concentrates on 4H-SiC devices; therefore, it is required to find $R_{on,sp}$ for 4H-SiC.

The following formulas for the on resistance for 4H-SiC and 6H-SiC MOSFETs are given in [7].

$$R_{on,sp}^{4H-SiC} = \frac{4V_B^2}{\varepsilon^{4H-SiC}(E_c^{4H-SiC})^3 \mu_n{}^{4H-SiC}} \tag{3.34}$$

$$R_{on,sp}^{6H-SiC} = \frac{4V_B^2}{\varepsilon^{6H-SiC}(E_c^{6H-SiC})^3 \mu_n{}^{6H-SiC}} \tag{3.35}$$

These two materials have the same dielectric constant, ε, and the same breakdown field, E_c; thus, for the same breakdown voltage, V_B, the on resistance formulas can be written as

$$R_{on,sp}^{4H-SiC} = \frac{K}{\mu_n{}^{4H-SiC}} \text{ and } R_{on,sp}^{6H-SiC} = \frac{K}{\mu_n{}^{6H-SiC}}$$

where $K = \frac{4V_B^2}{\varepsilon(E_c)^3}$

Equating *K*s from both of the above equations.

$$
\begin{aligned}
R_{on,sp}^{4H-SiC} \cdot \mu_n{}^{4H-SiC} &= R_{on,sp}^{6H-SiC} \cdot \mu_n{}^{6H-SiC} \\
R_{on,sp}^{4H-SiC} \cdot 1000 &= R_{on,sp}^{6H-SiC} \cdot 500 \\
R_{on,sp}^{4H-SiC} &= R_{on,sp}^{6H-SiC} \cdot \frac{1}{2} = 0.61\times10^{-3} \cdot \frac{1}{2} \\
&= 0.305\times10^{-3}\,\Omega
\end{aligned}
\tag{3.36}
$$

In [7], it is also reported that $R_{on,sp}$ is proportional to a power of the temperature. This is because $R_{on,sp} \propto \frac{1}{\mu_n}$ and $\mu_n \propto \frac{1}{T^{\alpha}}$. Thus, $R_{on,sp} \propto T^{\alpha}$ where α is a constant and is 2.42 for Si and 1.3 for 6H-SiC.

Assuming that α for 4H-SiC is the same value as α for 6H-SiC and taking the $R_{on,sp}$ values at 300°K as a basis, $R_{on,sp}$ at higher temperatures can be calculated as follows:

$$
R_{on,sp}^{T} = R_{on,sp}^{300K}\left(\frac{T}{300}\right)^{\alpha} \tag{3.37}
$$

The on-resistance values are shown in Table 3.7 for different temperature values

Table 3.7: On resistance values for Si and 4H-SiC at different temperatures.

T (K)	$R_{on,sp}^{Si}$ (mΩ)	$R_{on,sp}^{4H\text{-}SiC}$ (mΩ)	$R_{on,sp}^{Si}/R_{on,sp}^{4H\text{-}SiC}$
300	188	0.305	614.82
325	223	0.338	672.48
350	272	0.373	730.68
375	322	0.408	789.38
400	376	0.443	848.55
425	*436*	0.480	*908.17*
450	*500*	0.517	*968.21*
475	*570*	0.554	*1028.65*
500	*646*	0.593	*1089.48*

and are also plotted in Figure 3.19.

As seen in Table 3.7, the on-resistance of the Si MOSFET is more than 600 times larger than that of 4H-SiC MOSFET. Furthermore, the on-resistance of a Si MOSFET triples when the junction temperature increases from 300°K to 500°K while the on resistance of 4H-SiC MOSFET only doubles in the same temperature range. Note that Si MOSFET cannot operate at temperatures over 423K (150°C); however, the $R_{on,sp}$ values in Table 3.7 are calculated only for an hypothetical comparison.

The conduction loss is directly proportional to the on-resistance; therefore, the

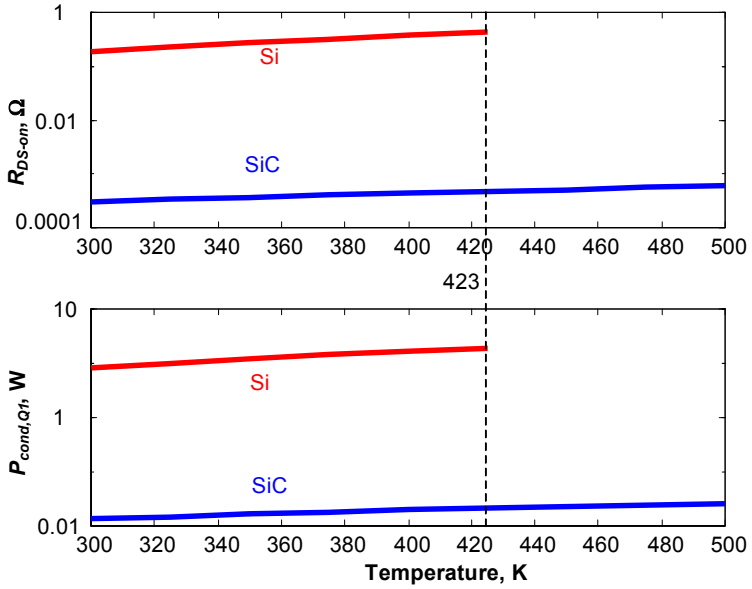

Figure 3.19 : Specific on resistance vs temperature (logarithmic plot).

conduction loss vs. temperature graph is a scaled version of the on-resistance vs. temperature graph as seen also in Figure 3.19.

3.2.2.2. Switching losses

The switching losses of a MOSFET can be calculated using piece-wise linear turn-on and turn-off waveforms. This is an approximation, which does not consider the physics behind switching. In this study, however, a more accurate physics-based model is going to be derived.

The turn-on and turn-off energy loss equations are derived in [32] as

$$E_{on} = \frac{1}{3(K_1 - 1)} \varepsilon_s E_c V \left(\frac{V}{BV} \right)^{1/2} \tag{3.38}$$

$$E_{off} = \frac{1}{3(K_2 + 1)} \varepsilon_s E_c V \left(\frac{V}{BV} \right)^{1/2} \tag{3.39}$$

where E_{on} and E_{off} are the losses during the charging and discharging of two device capacitances: drain-to-source and drain-to-gate (Figure 3.20). These capacitances are charged and discharged by effective currents of $(K_1\text{-}1)J$ and $(K_2\text{+}1)J$ respectively

where $K_1 = \frac{g_m (V_{GH} - V_{th})}{J}$ and $K_2 = \frac{g_m (V_{th} - V_{GL})}{J}$

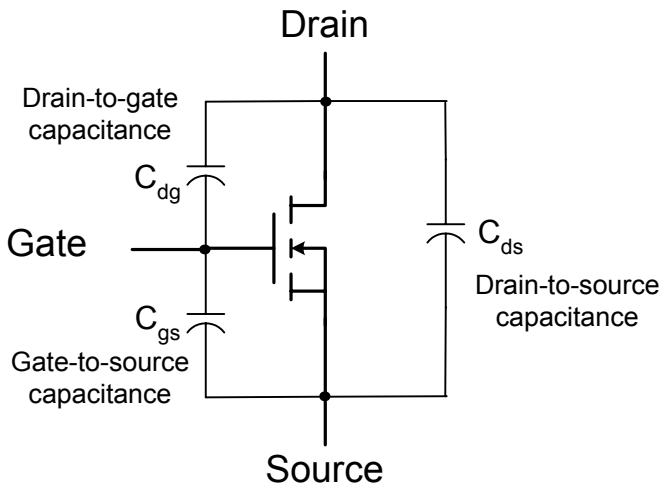

Figure 3.20: MOSFET capacitances

where g_m is the transconductance,

J is the current density

V_{GH} is highest gate voltage applied,

V_{GL} is lowest gate voltage applied, and

V_{th} is the threshold voltage

The energy loss for a turn-on and a turn-off of a MOSFET is the sum of (3.38) and (3.39)

$$E_{tot} = E_{on} + E_{off} = \frac{1}{3}\varepsilon_s E_c V \left(\frac{V}{BV}\right)^{1/2}\left[\frac{1}{(K_1 - 1)} + \frac{1}{(K_2 + 1)}\right]. \tag{3.40}$$

If a MOSFET is switched at a frequency of f_c, then its switching losses can be represented as

$$
\begin{aligned}
p_{Q1} &= f_c \cdot E_{tot} \\
&= f_c \cdot \left(E_{on} + E_{off}\right) \\
&= f_c \frac{1}{3} \varepsilon_s E_c V \left(\frac{V}{BV}\right)^{1/2} \left[\frac{1}{\left(K_1 - 1\right)} + \frac{1}{\left(K_2 + 1\right)}\right]
\end{aligned}
\quad . \tag{3.41}
$$

3.3. Summary

In this chapter, commercial Si and SiC power diodes have been tested, characterized, compared, and modeled. It has been found that SiC diodes have higher on voltages; consequently, they have higher conduction losses, especially for temperatures greater than 55°C. On the other hand, SiC diodes have been found to have lower switching losses, which are constant throughout their wider operation temperature range (≤250°C). The overall losses of the SiC diodes have been calculated to be much less than those of their Si counterparts.

In addition to diodes, Si and SiC MOSFETs have also been modeled; however, for MOSFETs, only theoretical models have been derived because of the lack of commercial SiC MOSFETs. The main difference between Si and SiC MOSFET losses is in the conduction losses because SiC MOSFETs have been calculated to have around 600 times less conduction losses than their Si counterparts.

These device models will be used to develop system level models in the next chapter.

As far as the contributions in this chapter are concerned, one of them is the development of a diode modeling procedure, which incorporated experimental test data, and also scaling 10A diodes to 200A. The other contribution is the application of genetic algorithm curve fitting method to model the static characteristics of diodes.

Chapter 4

SYSTEMS

In the previous chapters, SiC material and its properties have been explained; SiC power diodes and MOSFETs have been modeled and compared with their Si counterparts. The results have shown the superiority of SiC compared with Si in the materials and device levels. The impact of these SiC devices in the system level has been predicted before, but no quantitative proof is available, yet. In this chapter, some simulation tools will be developed to simulate two different converters used in HEV applications and the SiC system impact on these converters will be investigated.

In an HEV, the most important power converters are in the dc-dc power supplies or in the electric traction drive. A wide variety of dc-dc converters can be found

in an HEV, and it would be difficult and redundant to study and simulate every one of them to show the impact of SiC devices. Instead in this study, one sample dc-dc converter will be studied; the results can then be generalized to all the other converters because these converters are more or less similar. The sample converter in this study is an isolated full-bridge dc-dc converter, which is selected mostly because of its the high frequency transformer, which provides isolation and additional taps in the secondary to feed more than one converter. In this chapter, the dc-dc converter thermal model will be developed using the device models from the previous chapter, and it will be used to show the reduction in the heatsink size and volume due to SiC's lower losses and its high temperature operation capability. In addition to this, considering the high frequency operation capability of SiC power devices, the reduction in the size of the filter components and the transformer at higher frequencies will also be investigated.

The second power converter to be studied is the main traction drive, which uses most of the power in an HEV when the vehicle is in motion. A traction drive consists of a battery feeding a three-phase induction machine through a three-phase inverter. Because of the cooling requirements of the power devices in the inverter, usually a large heatsink is required. In an HEV, any reduction in volume and weight of any component will benefit the efficiency of the vehicle.

Because SiC devices can operate at higher temperatures and they have lower losses, the heatsink volume and weight can be reduced if all SiC devices are used in the inverter. To show this quantitatively, the traction drive loss model will be derived using the device models developed in the previous chapter and will be simulated over the federal urban driving schedule. In addition to this, reduction in device losses and the consequent increase in the efficiency will also be demonstrated.

The models of both of the converters will be simulated using all Si devices and all SiC devices to compare the results of both and show the superiority of SiC power devices in the systems level.

4.1. Dc-dc Power Supply

There are many power converter configurations available for dc-dc power supplies. In this study, a commonly used dc-dc converter topology is selected: full-bridge isolated step-down dc-dc converter (Figure 4.1). The main reason for selecting this topology, as explained before, is the transformer, which isolates the load from the source. It can also be used to feed more than one load if extra transformer taps are included, which would be desirable for a HEV application.

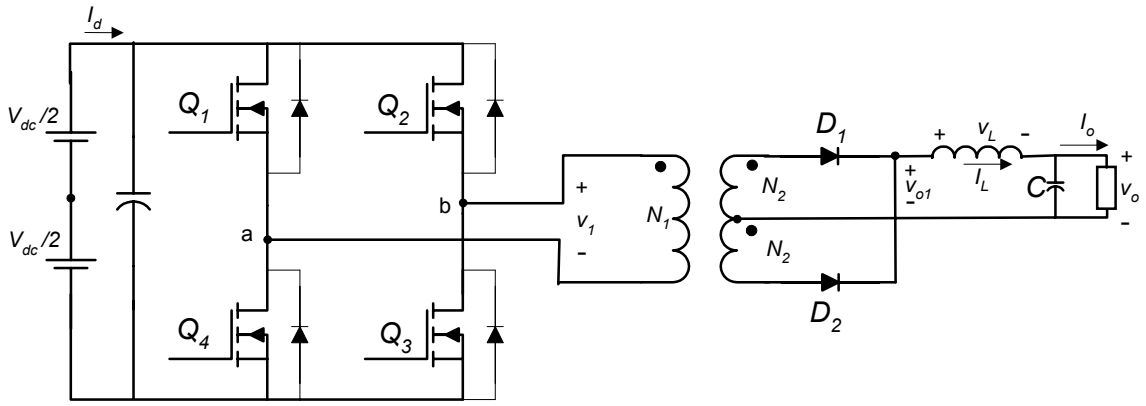

Figure 4.1: Isolated full-bridge step-down dc-dc converter.

If the impact of SiC power devices on this converter is shown, the results can be generalized to other dc-dc converters.

The dc-dc converter, here, is designed to supply a 2 - 5 kW variable load with regulated output voltage at 42 V and the input voltage fluctuating between 300V and 450V. This application can be used in any kind of vehicle; therefore, the results do not just hold for HEVs.

The impact of SiC power devices on this converter will be investigated in two categories: thermal studies and passive component studies. The former will show the savings in thermal management because of the high temperature operability of SiC devices and their lower total losses. The latter will consider the high frequency operation of SiC power devices and how this affects the sizing of the passive converters in the dc-dc converter.

4.1.1. The dc-dc converter operation

This converter consists of two stages: a high frequency inverter and a rectifier. The first stage converts the dc voltage to high frequency square wave by switching Q_1 and Q_3 or Q_2 and Q_4 in pairs. When the first pair is on, the transformer primary sees a negative dc voltage, and when the second pair is on, it sees a positive dc voltage. When all the switches are off, the transformer primary sees no voltage. The operation waveforms are shown in Figure 4.2.

Diodes, D_1 and D_2 rectify the voltage fed to them from the secondary of the transformer. This rectified voltage then passes through an *LC* filter to feed the dc load.

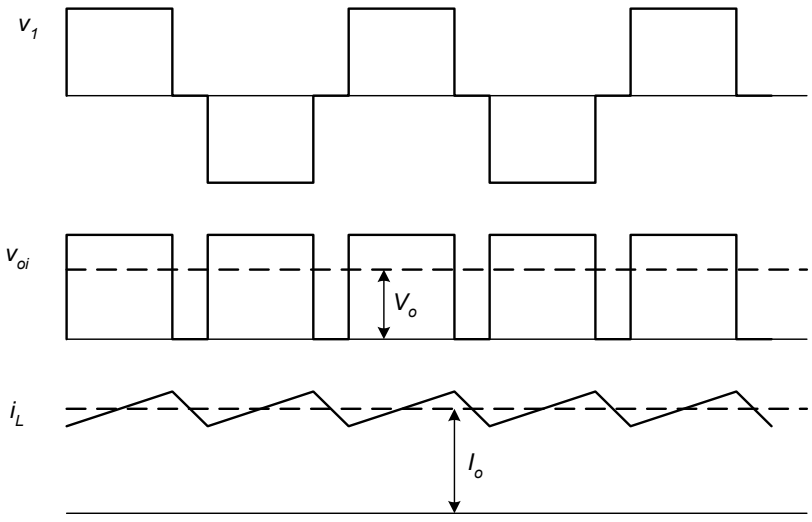

Figure 4.2: Operation waveforms of the dc-dc converter.

The maximum dc voltage across and current through each device are tabulated in Table 4.1 for minimum and maximum load and input voltage conditions.

4.1.2. Thermal studies

The device loss models have been derived in Chapter 3. In this section, these models will be used to model the losses of devices in the dc-dc converter.

4.1.2.1. MOSFET losses

4.1.2.1.1. Conduction losses

Because the rms current depends on the specific converter, this must be calculated for use in the loss model equations derived in the previous chapter.

For the full bridge converter, the current waveform can be approximated by a series of square pulses at the switching frequency. Then,

Table 4.1: Maximum device voltage and currents for different load power and input voltage conditions.

P_{out} (kW)	V_{dc} (V)	V_{MOSFET} (V)	I_{MOSFET} (A)	V_{DIODE} (V)	I_{DIODE} (A)
2	300	300	6.67	84	47
2	450	450	4.44	84	47
5	300	300	16.67	84	119
5	450	450	11.11	84	119

$$I_{Q(rms)} = \sqrt{d \cdot I_Q^2 + (1-d) \cdot 0^2} = I_Q \sqrt{d} \tag{4.1}$$

where d is the duty cycle.

Conduction losses of a MOSFET from (3.33) is

$$P_{cond} = I_{Q\,(rms)}^2 R_{DS,on} . \tag{4.2}$$

Thus,

$$P_{cond} = d \cdot I_Q^2 \cdot R_{DS,on} \tag{4.3}$$

4.1.2.1.2. Switching losses

The switching loss model of a MOSFET was derived in the previous chapter. Here, the equation will be repeated for Q_1.

$$p_{Q_1} = f_c E_{tot} = f_c \frac{1}{3} \varepsilon_s E_c V \left(\frac{V}{BV} \right)^{1/2} \left[\frac{1}{(K_1 - 1)} + \frac{1}{(K_2 + 1)} \right] \tag{4.4}$$

where $K_1 = \frac{g_m (V_{GH} - V_{th})}{J}$ and $K_2 = \frac{g_m (V_{th} - V_{GL})}{J}$

J in this case is the current density, I_D/A, where A is the device area.

4.1.2.2. Diode losses

4.1.2.2.1. Conduction losses

The main difference between the diode conduction loss model in this section and one in the previous chapter is the difference in the rms and average current expressions, which depend on the converter operation.

For the full bridge converter, the diode current waveform can also be approximated as a series of square pulses at the switching frequency resulting in

$$\begin{aligned} I_{D,rms} &= \sqrt{d \cdot I_D^2 + (1-d) \cdot 0^2} \\ &= I_D \sqrt{d} \end{aligned} \tag{4.5}$$

and

$$I_{D,av} = d \cdot I_D . \tag{4.6}$$

Conduction losses of a diode can be calculated as

$$P_{cond} = I_{D,av} \cdot V_D + I_{D,rms}^2 \cdot R_D \tag{4.7}$$

Then,

$$\begin{aligned} P_{cond} &= d \cdot I_D \cdot V_D + d \cdot I_D^2 \cdot R_D \\ &= d\left(I_D \cdot V_D + I_D^2 \cdot R_D\right) \end{aligned} \tag{4.8}$$

For the computer simulation, (3.10) – (3.13) developed in Chapter 3 are inserted into (4.8) and implemented in SIMULINK.

4.1.2.2.2. Switching losses

As explained in the previous chapter, multiplying (3.27) and (3.28) by $V_R \cdot f_c$ product and inserting the result in (3.29) gives the reverse recovery losses of a diode. For the dc-dc converter V_R=84V and f_c is not necessarily 20kHz. To obtain the diode switching loss model for the dc-dc converter at any switching frequency, multiply (3.27) and (3.28) by $V_R \cdot f_c = 84 \cdot f_c$ V·Hz.

4.1.2.3. Results

The dc-dc converter loss model is simulated at the full-load condition at two different switching frequencies, 20kHz and 100 kHz. The resulting loss profiles are fed to the device thermal model shown in Figure 4.3. The SIMULINK model for the Si case is shown in Figure 4.4, which is identical to the SiC model except for the device models.

The natural air-cooled heatsinks are selected to limit the junction temperatures of devices to their rated values, 150°C for Si and 175°C [13] for SiC. The resulting heatsink size and volume are listed in Tables 4.2 and 4.3.

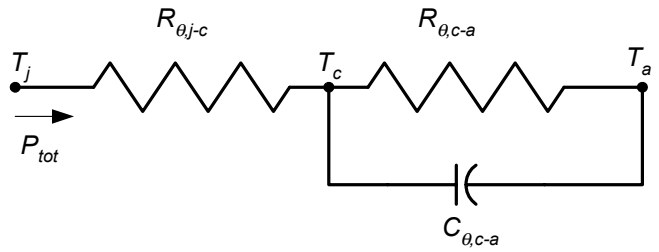

Figure 4.3: Simple transient thermal model of a semiconductor device.

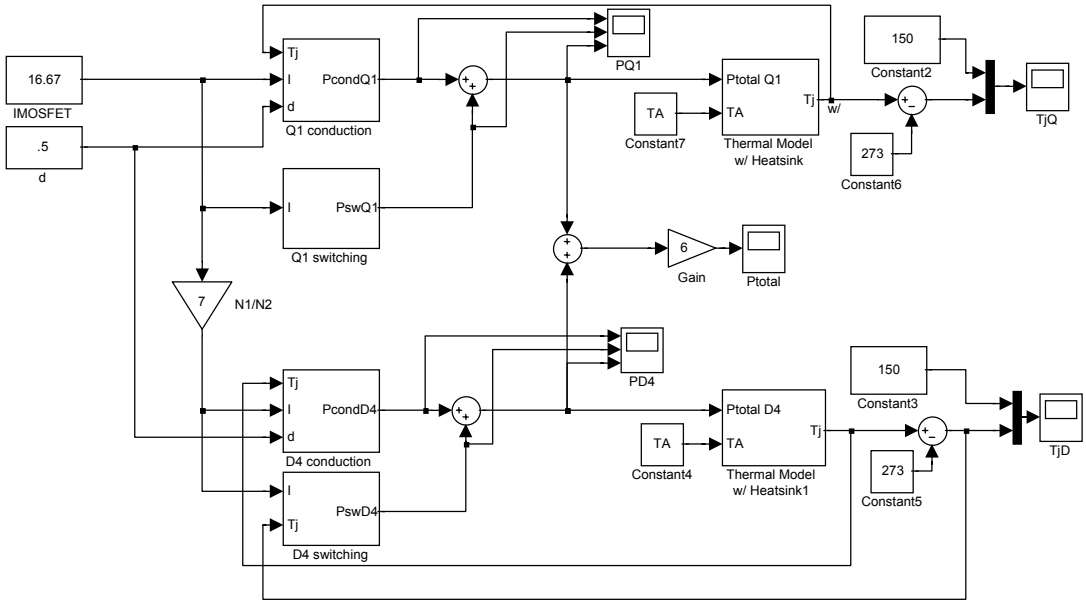

Figure 4.4: SIMULINK model of the dc-dc converter thermal simulation.

Table 4.2: Required heatsink mass and volume for the dc-dc converter operating at full load and switching at 20 kHz.

20kHz	Volume (cm^3)	Mass (g)
Si diodes	412	1111
SiC diodes	549	1481
Si MOSFETs	347	936
SiC MOSFETs	41	111
Si inverter	***759***	***2047***
SiC inverter	***590***	***1592***

Table 4.3: Required heatsink mass and volume for the dc-dc converter operating at full load and switching at 100 kHz.

100kHz	Volume (cm^3)	Mass (g)
Si diodes	775	2092
SiC diodes	626	1691
Si MOSFETs	1197	3232
SiC MOSFETs	205	556
Si inverter	***1972***	***5324***
SiC inverter	***831***	***2247***

As expected, Tables 4.2 and 4.3 show the reduction in the converter heatsink mass and volume when SiC devices are used instead of their Si counterparts; however, there is one point that needs special attention. In Table 4.2, it is observed that the SiC diodes require a bigger heatsink compared to the Si diodes for the 20kHz operation. This is because in this case, as the devices' temperature increases, the conduction loss of the Si diodes decreases (Figure 4.5) while that of the SiC diodes increases. The advantage of SiC diode in the switching losses is not enough to make up for their disadvantage in the conduction losses. SiC diode total losses are more than the Si diode total losses.

However, if the switching frequency is increased five times to 100 kHz, then the diode switching losses also increase five times (Figure 4.6). In this case, the switching losses become more dominant. As a result, SiC diode total losses are slightly lower than those of the Si diode and the required heatsink size is also less.

For the MOSFETs, the main difference in the losses comes from the low on resistance of the SiC MOSFET compared to its Si counterpart. As a result, the SiC MOSFET requires more than six times less heatsink at both frequencies.

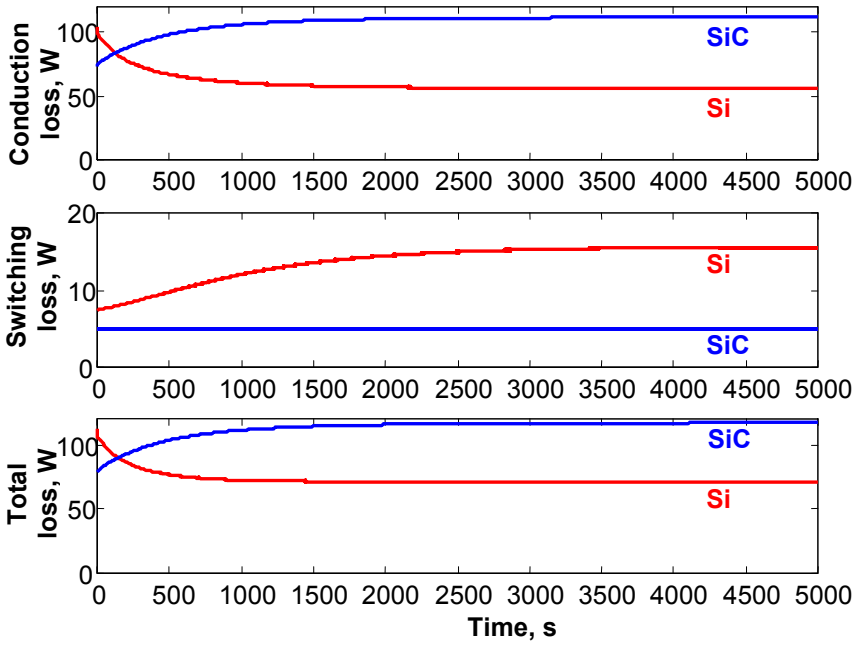

Figure 4.5: Diode losses in the dc-dc converter (20 kHz operation).

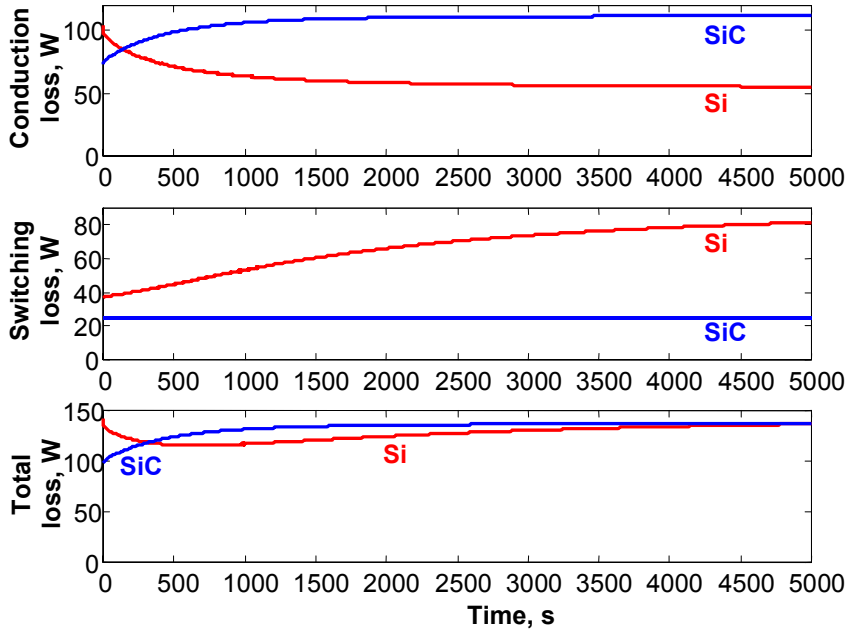

Figure 4.6: Diode losses in the dc-dc converter (100kHz operation)

Overall, the SiC dc-dc converter weighs 0.455 kg less and occupies 169 cm^3 less space for 20kHz operation and weighs 3.077 kg less and occupies 1141 cm^3 less space for 100kHz operation compared to the similar Si dc-dc converter.

4.1.3. Passive components

As discussed in the first two chapters, SiC devices can be switched at a higher rate than their Si counterparts because of their low losses and high temperature operation capability. There are two main advantages associated with high frequency switching: reduced filtering requirements and smaller passive components. These advantages will be investigated in the following subsections.

4.1.3.1. High frequency transformer

Whenever transformers are mentioned, the bulky 60 Hz transformers come to mind. However, high frequency transformers are much smaller than these. A 46kVA, 50kHz transformer is reported in [33] to weigh only 3.83 kg with a cubic structure of roughly 20 cm for each dimension.

To understand how the switching frequency affects the size of the transformer, consider the maximum flux density, B_{max} equation given in [34] for a transformer supplied by a square wave at a frequency of f_c.

$$B_{\max} = \frac{V}{4 f_c} \cdot \frac{1}{NA} \tag{4.9}$$

where V is the magnitude of the applied voltage, N is the number of turns, and A is the cross-section area of the magnetic circuit.

For a voltage V, if the switching frequency is increased, the area or the number of turns or both should be decreased correspondingly so that the $f_c \cdot N \cdot A$ product stays constant and the maximum flux density is maintained.

Then, a five times increase in the switching frequency from 20 kHz to 100 kHz, for a constant turns ratio, means five times less area, and consequently five times less volume and weight.

Note that this decrease in the size of a transformer is not always linear. As the switching frequency increases, the size of the transformer decreases but at a certain point, because of the eddy currents ("proximity effect") and "skin effect", the cooling requirements start dominating, and the size of the transformer has to be increased again for better thermal management.

4.1.3.2. Output filter requirements

The output filter of this dc-dc converter is a *LC* filter as shown in Figure 4.7 with a corner frequency of $f = \frac{1}{2\pi\sqrt{LC}}$. The filtered voltage and current ripple equations in the continuous conduction mode are given in [6] as

Current ripple, $\Delta I_o = \frac{V_o}{L}(1-d)T_c$, (4.10)

Voltage ripple, $\Delta V_o = \frac{T_c^2 V_o}{8LC}(1-d)$. (4.11)

where V_o and I_o are dc output voltage and current, T_c is the switching period, and d is the duty ratio.

Assume that the required filter is designed to limit the output ripple voltage to 1% of $V_o(\Delta V_o = 0.01 \times V_o = 0.42V)$, and the output ripple current to 10% of $I_o(\Delta I_o = 0.1 \times I_o = 11.9A)$.

For the converter in this study, the worst condition is when the load is maximum

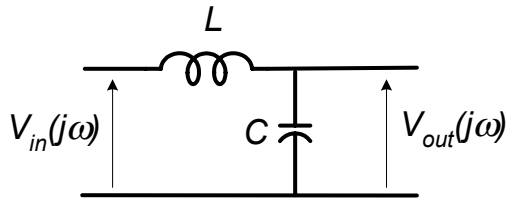

Figure 4.7: Output filter.

(maximum current ripple) and d is minimum (d_{min}=0.28, maximum voltage ripple). If the output filter is designed for the worst condition it would be sufficient for the rest of the operation region.

Using (4.10), an expression for L in terms of the switching frequency is found as

$$\begin{aligned}
\Delta I_o &< 11.9A \\
\frac{V_o}{L}(1-d)T_c &< 11.9 \\
11.9 &> \frac{V_o}{L}(1-d)T_c \\
L &> \frac{V_o}{11.9}(1-d)T_c \\
L &> \frac{42}{11.9}\cdot(1-0.28)\cdot T_c \\
L &> 2.54\cdot T_c = \frac{2.54}{f_c}
\end{aligned} \qquad (4.12)$$

The value of C can be found from (4.11),

$$\begin{aligned}
\Delta V_o &< 0.42 \\
\frac{1}{8}\frac{T_c^2}{LC}(1-d)V_o &< 0.42 \\
LC &> \frac{1}{8}\frac{T_c^2}{0.42}(1-d)V_o \\
LC &> \frac{1}{8}\frac{T_c^2}{0.42}(1-0.28)42 \\
LC &> 9T_c^2 = \frac{9}{f_c^2}
\end{aligned} \qquad (4.13)$$

Then, for a 20 kHz operation,

$L > \frac{2.54}{20000} = 127\mu H$ and $C > \frac{1}{127\times10^{-6}} \frac{9}{(20000)^2} = 177\mu F$. On the other hand, for a 100 kHz operation, $L > \frac{2.54}{100000} = 25.4\mu H$ and $C > \frac{1}{25.4\times10^{-6}} \frac{9}{(100000)^2} = 35.4\mu F$.

If the above values for L and C at different switching frequencies are considered, it can be observed that a five times increase in the switching frequency means a five times decrease in the filter component values. Figure 4.8 shows the decrease in L and C parameters at higher switching frequencies. How this decrease affects the size of the components will be investigated in the following subsections.

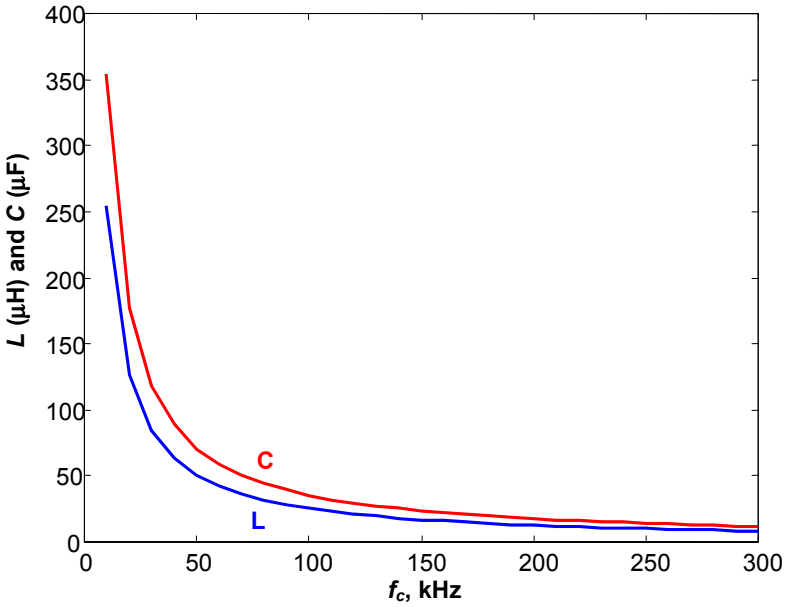

Figure 4.8: Filter parameters with respect to the switching frequency.

4.1.3.2.1. The size of the filter capacitor

The capacitance of a parallel plate capacitor is given as

$$C = \varepsilon \frac{A}{d_c} \tag{4.14}$$

where A is the area of the parallel plates and d_c is the distance between the capacitor plates. For the same voltage rating, if d_c is assumed constant, then for the same dielectric material, the capacitance varies with A. This means that k times less capacitance value means k times less capacitor area and consequently, volume.

For the dc-dc converter, the size of the required filter capacitance can be reduced five times if the switching frequency is increased from 20kHz to 100kHz.

Note that the above is a theoretical conclusion. In practice, the size of the capacitor also depends on the packaging size and availability.

4.1.3.2.2. The size of the filter inductor

A similar argument as in the high frequency transformer case can be applied here. The maximum flux in the case of an inductor [35] is

$$B_{\max} = \frac{LI_{\max}}{NA} \tag{4.15}$$

where L is the inductance and I_{max} is the maximum current level that corresponds to the maximum flux density. For the same application at different switching frequencies, I_{max} is the same and L is different. As the switching frequency increases, L decreases as shown in Figure 4.8; therefore, to keep B_{max} constant, N, A or both have to be decreased proportionally.

At the end, the same conclusion as in the filter capacitor case can be applied here. Overall, the required filter size, including both the filter capacitance and inductance, decreases five times if the switching frequency is increased from 20kHz to 100kHz.

4.2. Electric Traction Drive

The electric traction drive in this study is shown in Figure 4.9. It consists of a battery feeding a three-phase PWM inverter, which in turn feeds an ac machine. The highest power converter in a HEV is the three-phase inverter in the electric traction drive. As a result of high power operation, the inverter losses are higher and consequently, it has a large heatsink to dissipate the heat and to limit the device temperatures below the rated value.

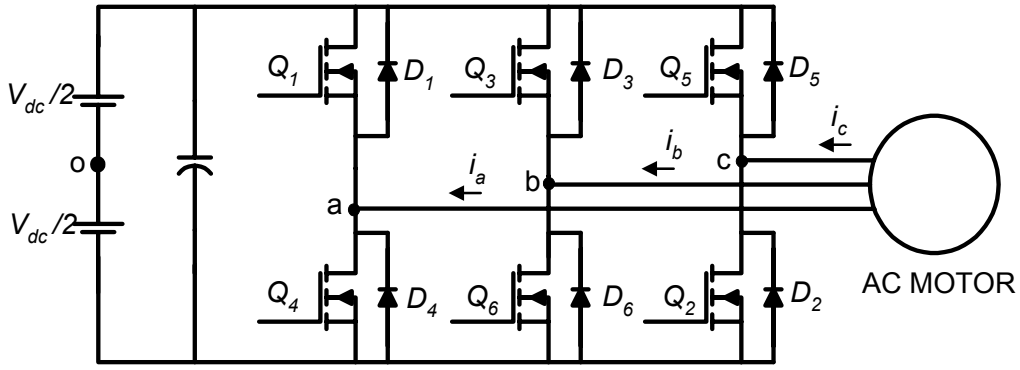

Figure 4.9: Three-phase inverter driving an induction machine load.

It is expected that if Si power devices in this inverter are replaced with their SiC counterparts, the device losses will decrease, inverter efficiency will increase, and the size of the required heatsink will decrease. In this section, these comments will be quantitatively demonstrated through thermal modeling using the device models developed in Chapter 3.

Considering this is a vehicle application, after the thermal model is developed, it has to be simulated over a practical driving schedule. The drive schedule generally used for vehicle testing is the Federal Urban Driving Schedule (FUDS), which is a 1369-second velocity profile of an average person's vehicle on the way to work from home (Figure 4.10).

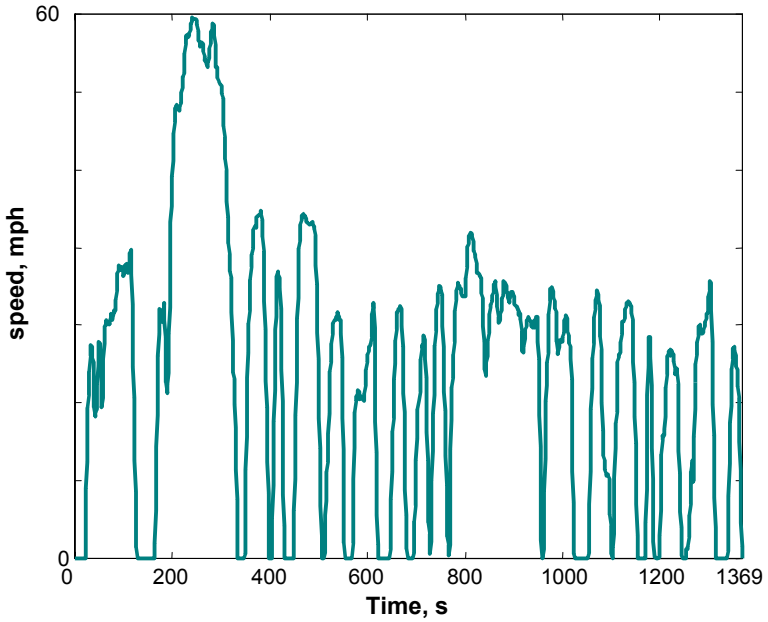

Figure 4.10: Federal Urban Driving Schedule (FUDS).

4.2.1. Average modeling of the inverter

Simulating the thermal model over the FUDS cycle is an involved and time-consuming procedure for a PWM inverter. This is because of the order of the sampling frequency difference between the driving schedule, the inverter, and device simulations (Figure 4.11).

Between the two sampling points of the FUDS cycle (1 second), the waveforms of an induction motor running at 200 Hz would run for 200 cycles. Moreover, during the same interval, the inverter devices switching at 20 kHz would turn on and off 20000 times. If device simulation is ignored, then the sampling time can be selected to be around 1μs resulting in 10^6 simulation points per second of

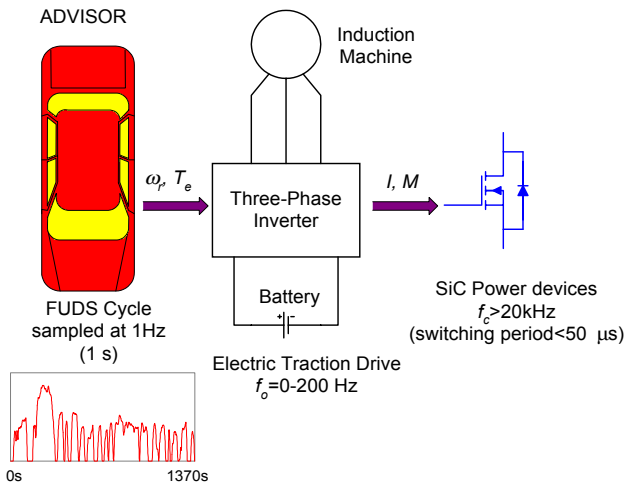

Figure 4.11. Block diagram of the traction drive model.

simulation. If device loss calculations are to be included, then the device turn-on and turn-off times are also important; therefore, the sampling time should be selected considering the dynamics of the device. Fast switching devices have switching times on the order of tens or hundreds of nanoseconds. A simulation for device losses then should have a sampling time of around 1ns. This means 10^9 points in one second and 1369×10^9 points over the FUDS cycle. This would take roughly around 1000 times more than the converter simulation ignoring the devices' dynamics.

In the literature, an averaging technique that gives a good estimation of the behavior of the converter at a shorter time has been proposed [36, 37]. This technique is applied by averaging all the variables in a switching cycle and using this average as a sampling point for the new model. As mentioned earlier, for an

inverter operating at 20kHz, the simulation sampling time can be selected as 1μs. Thus, 1s of simulation requires 10^6 points. If the averaging technique is used, then each switching cycle of 50μs (corresponding to 20 kHz) will be one average sample. The resulting number of samples will then be 20000, which is 50 times less than the original number of samples. This significantly reduces the simulation time. Note that, when device dynamic modeling and lower sampling times are considered, the savings will be much more than this.

4.2.1.1. Derivation of the average model

To understand how the averaging technique works, first consider an output voltage waveform and its construction for a PWM inverter given in Figure 4.12 for half a cycle of a sinusoidal modulating wave. The crossing points of the modulating wave and the triangular carrier wave give the switching instants. The output voltage, v_{ao} is, thus, a square wave with variable duty ratio. The duty ratio is varied in such a way to produce an output waveform with as low total harmonic distortion as possible.

Now, assume that the modulating wave v_{ao}* is a constant, K, during T_c period as shown in Figure 4.13. This assumption is valid when the output period, T_o is more than ten times greater than the switching period, T_c., which is usually the case.

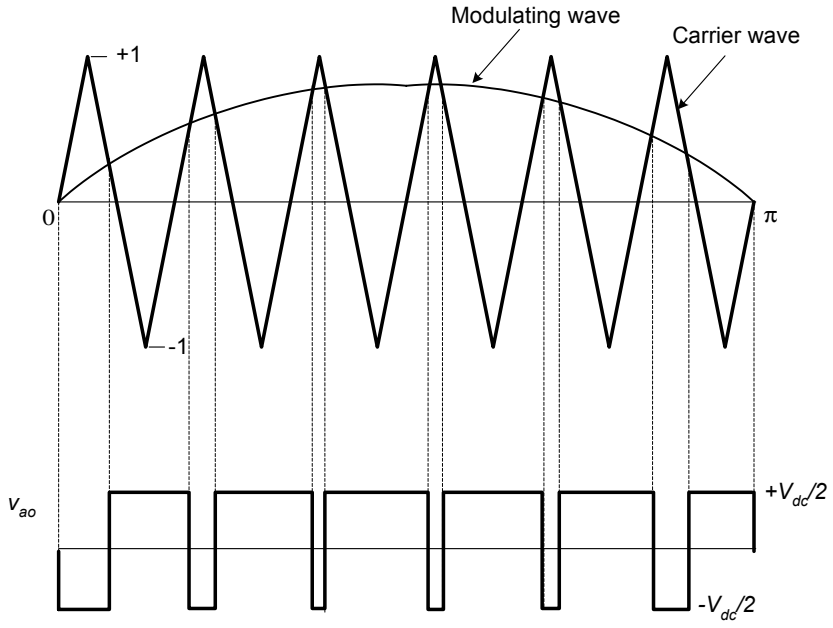

Figure 4.12: PWM operation waveforms.

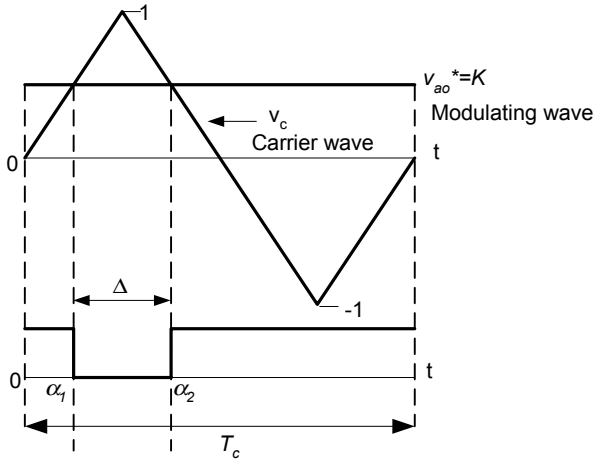

Figure 4.13: PWM operation in one switching cycle.

Averaging v_{ao} over T_c gives

$$\bar{v}_{ao} = \frac{1}{T_c}\int_0^{T_c} v_{ao}\,dt = K\frac{V_{dc}}{2} \tag{4.16}$$

In practice, v_{ao}* is a sinusoidally varying waveform with a peak value of M, where M is the modulation index and $\theta = \omega_o \cdot t$.

$$v_{ao} = M\sin\theta \tag{4.17}$$

Thus, (4.16) becomes

$$\bar{v}_{ao} = M\sin\theta\frac{V_{dc}}{2} \tag{4.18}$$

$\bar{v}_{bo}$ and $\bar{v}_{co}$ can be found by delaying $\bar{v}_{ao}$ by $2\pi/3$ and $4\pi/3$, respectively.

$$\bar{v}_{bo} = M\sin\left(\theta - \frac{2\pi}{3}\right)\frac{V_{dc}}{2} \tag{4.19}$$

$$\bar{v}_{co} = M\sin\left(\theta - \frac{4\pi}{3}\right)\frac{V_{dc}}{2} \tag{4.20}$$

4.2.1.2. Verification by simulation

For the averaging technique, at every T_c, variables are averaged; and the average value is assumed to be the constant value of the same variable over T_c. As a

result, $\bar{v}_{ao}$ is a stepped waveform like the one shown in Figure 4.14 sampled at a frequency of $f_c=1/T_c$, where each step corresponds to the average of the actual v_{ao} in the same interval, T_c. The same is also true for $\bar{v}_{bo}$ and $\bar{v}_{co}$.

These averaged voltages are fed to a three-phase induction machine to validate the accuracy of the averaging technique. Figure 4.15 shows the SIMULINK model developed to compare the average model with the actual model. This model is simulated for 1.5s with a step torque applied at 1s, and the results are plotted in Figures 4.16 and 4.17. The first figure corresponds to the steady-state condition without a load. The second one, on the other hand, shows the transient operation of the system after the step torque is applied. In these figures, it can be

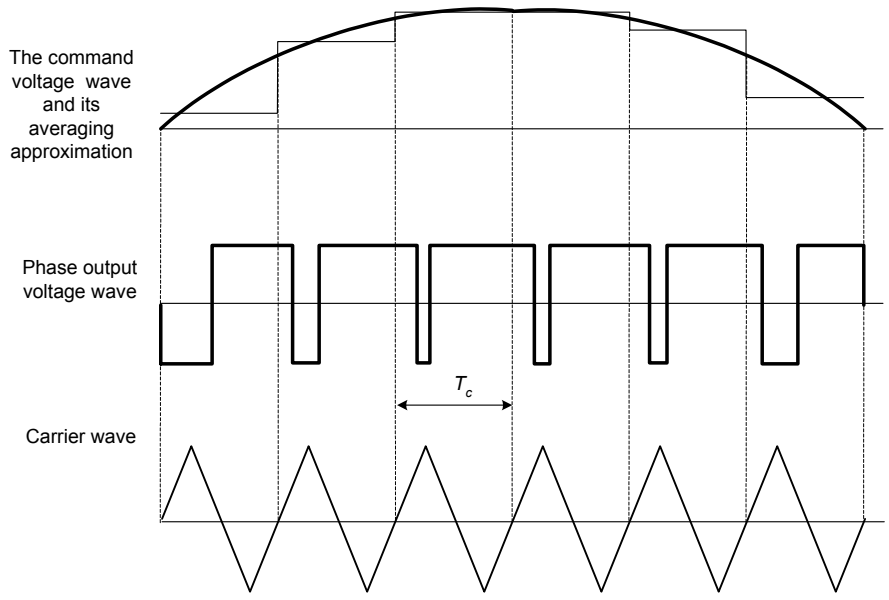

Figure 4.14: Averaging model explanatory waveforms.

observed that the averaging model tracks the actual system perfectly not only at steady state but also during the transients.

The induction machine block in Figure 4.15 contains an induction machine model, which was developed by the author and included in a recent graduate level power electronics book [38]. The details of this model are given in Appendix B.

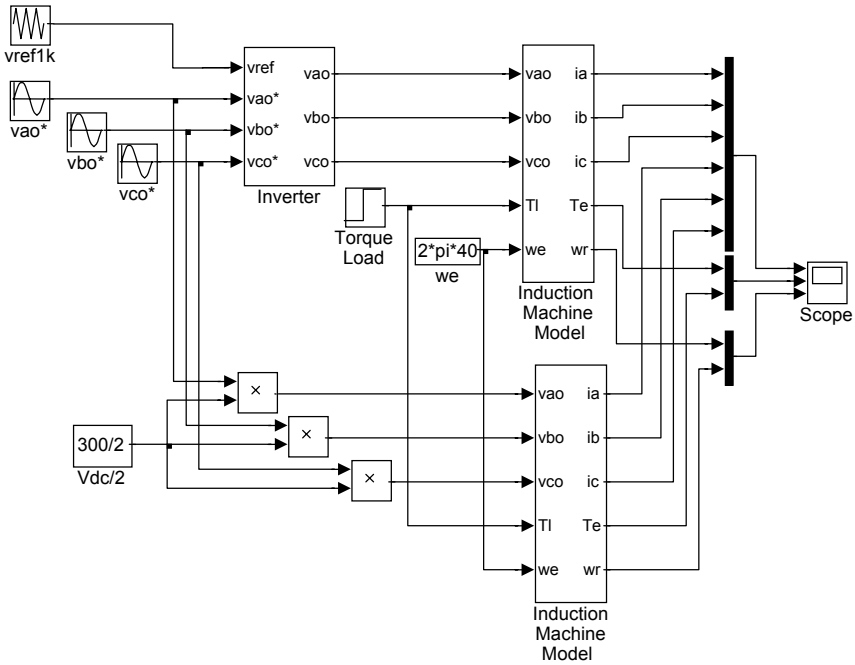

Figure 4.15: SIMULINK model developed to verify the averaging model.

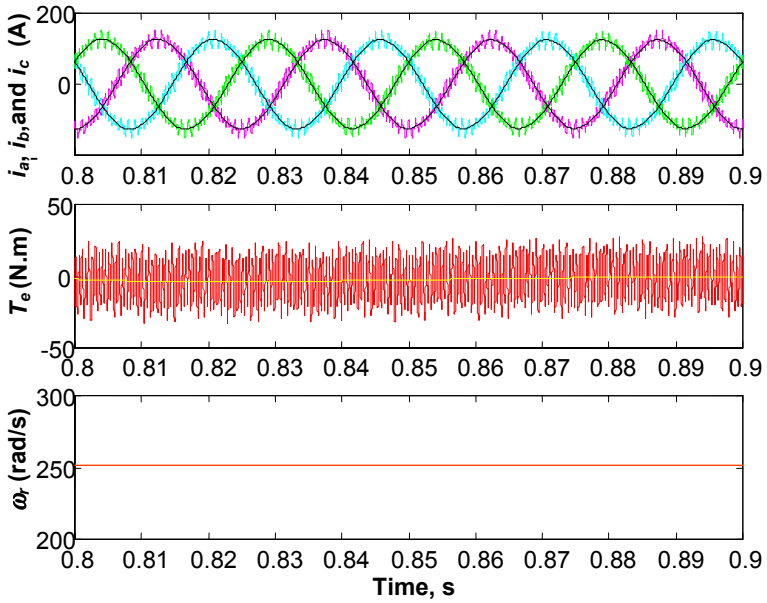

Figure 4.16: Verification of the averaging model (steady-state).

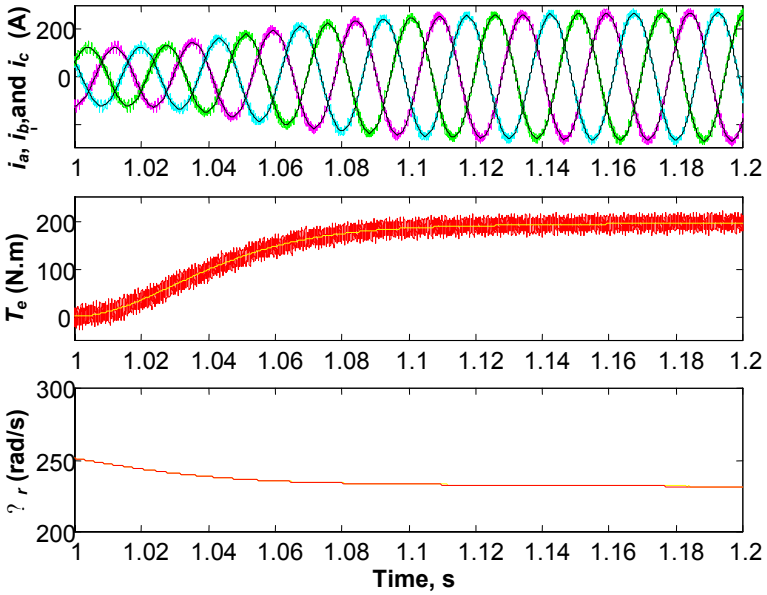

Figure 4.17: Verification of the averaging model (transient).

4.2.1.3. Averaging model as a "moving average filter"

The output waveforms of the averaging model look like the filtered versions of the actual waveforms. Essentially, it is observed that the averaging algorithm acts like a moving average filter.

A "moving average filter" (MA filter) is represented in [39] as

$$\begin{aligned} y[n] &= \frac{1}{M_1 + M_2 + 1} \sum_{k=-M_1}^{M_2} x[n-k] \\ &= \frac{1}{M_1 + M_2 + 1} \{x[n+M_1] + x[n+M_1-1] + \cdots + x[n]. \\ &\quad + x[n-1] + \cdots + x[n-M_2]\} \end{aligned} \tag{4.21}$$

n=0, 1, 2, 3, …

Figure 4.18 shows a general MA filter example for two different n values with

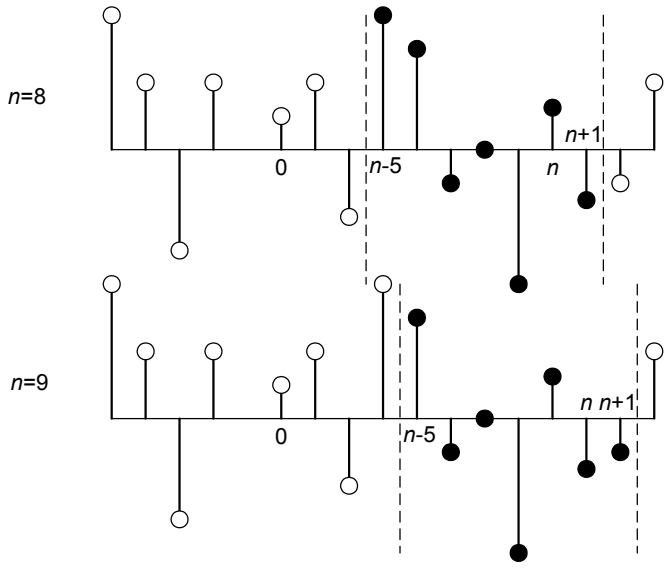

Figure 4.18: MA filter example for n=8 and n=9.

M_1=5 and M_2=1. The average filter moves one sample at a time calculating the average of the samples in a window formed by M_1 samples before and M_2 samples after n.

Compared to a MA filter, the averaging model moves one switching cycle at a time calculating the average of the samples in each cycle.

To represent the average model as a MA filter, first a sampling rate has to be selected and the number of samples in a switching cycle needs to be calculated. Let the sampling rate be f_s (sampling period $T_s=1/f_s$); then the number of samples in a switching cycle is $(T_c/T_s)+1$. Samples at $[n+M_1]$ and $[n-M_2]$ correspond to the end points while n is selected to be the midpoint of the switching cycle. Note that n can be selected to be any point in T_c as long as $[n+M_1]$ and $[n-M_2]$ correspond to the end points. If n is the midpoint as in Figure 4.19, then $M_1=M_2=T_c/(2T_s)$. As a result, the average model can be represented as a special MA filter in the same form as (4.21) but with

$M_1=M_2= T_c/(2T_s)$ and $n=n_0+mT_c$ ($n_0=T_c/2$ and $m=1, 2, 3,\ldots$) (4.22)

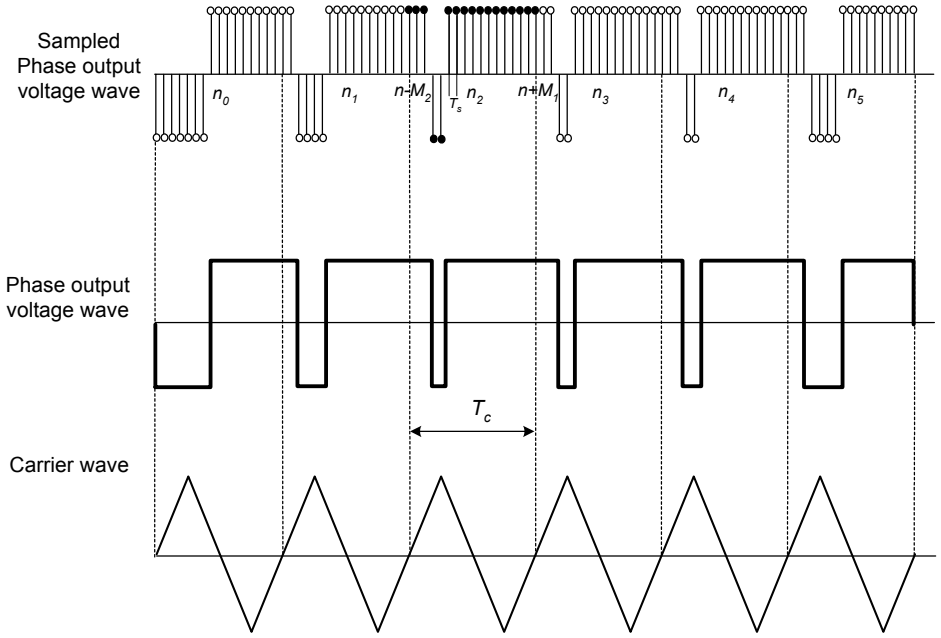

Figure 4.19: Averaging model as a MA filter.

4.2.1.4. MOSFET losses

4.2.1.4.1. Conduction losses

In the on state, a MOSFET acts like a resistor; therefore, its conduction losses are resistive as shown below

$$P_{cond,Q1} = I_{Q1,rms}^2 \cdot R_{DS,on}. \tag{4.23}$$

$I^2_{Q1,rms}$ can be found directly by the averaging technique as

$$I_{Q1,rms} = \sqrt{\frac{1}{N}\sum_{n=0}^{N-1} i_{o,n}^2 D_n} \tag{4.24}$$

where D_n = PWM duty ratio in the nth interval,

$i_{o,n}$ = average output current in the nth interval,

$N = \frac{f_c}{f_o} = \frac{T_o}{T_c}$, the number of intervals in an output period, (4.25)

$i_{o,n} = I\sin(\theta_n - \phi)$, I = peak output current, and (4.26)

$\theta_n = \frac{2\pi n}{N}$, ϕ = phase angle of the current (4.27)

4.2.1.4.1.1. PWM duty ratio

The duty ratio varies from switching cycle to switching cycle because of the PWM operation. To find the duty ratio, first consider one switching cycle of PWM operation with a constant modulating wave as shown in Figure 4.13.

The equation of the carrier wave is as follows:

$$v_c = \begin{cases} 4t/T_c & t < T_c/4 \\ 2 - 4t/T_c & T_c/4 < t < 3T_c/4 \\ -4 + 4t/T_c & 3T_c/4 < t < T_c \end{cases} \quad (4.28)$$

At the intersection points of the modulating wave and the carrier wave, assuming K>0,

$$K = \frac{\alpha_1}{T_c/4} \Rightarrow \alpha_1 = \frac{T_c}{4}K \quad (4.29)$$

$$K = 2 - \frac{\alpha_2}{T_c/4} \Rightarrow \alpha_2 = (2-K)\frac{T_c}{4}. \tag{4.30}$$

Then,

$$D = \frac{T_c - (\alpha_2 - \alpha_1)}{T_c} = 1 - \frac{\alpha_2 - \alpha_1}{T_c} = 1 - \frac{(2-K)T_c/4 - K\,T_c/4}{T_c} = \frac{1}{2} + \frac{K}{2} \tag{4.31}$$

Now consider a sinusoidally modulated v_{ao}^* instead of a constant K.

$$v_{ao}^* = M \sin\theta \tag{4.32}$$

where M is the modulation index.

$$D = \frac{1}{2} + \frac{M \sin\theta}{2} = \frac{1}{2}(1 + M \sin\theta) \tag{4.33}$$

This is the duty ratio of the main switches in the inverter. The duty ratio of the diodes, however, is different because they conduct when the switches are not conducting; therefore, the duty ratio of the diodes is *(1-D)* where '1' represents one hundred percent duty ratio. Thus,

$$D' = 1 - D = \frac{1}{2}(1 - M \sin\theta) \tag{4.34}$$

4.2.1.4.1.2 Averaged rms currents

To calculate the conduction losses in (4.23), rms device currents are needed. First, consider the rms value of the current in the first switching cycle in Figure 4.20. Note that in this figure, it was assumed that the switching frequency, f_c, is much

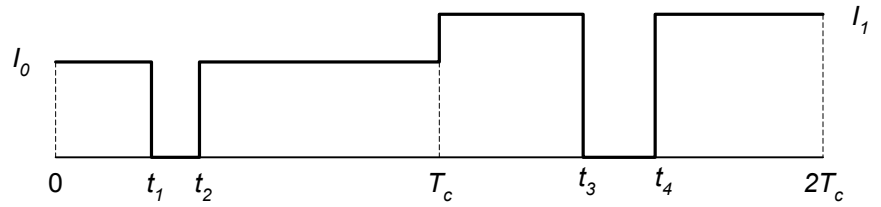

Figure 4.20: The switch current waveforms in two switching cycles.

greater than the output frequency, f_o ; thus, the switch current does not change much in T_c and can be assumed constant. Also note that the current jump from the first cycle to the next one is exaggerated in the figure.

Then considering the first cycle,

$$\begin{aligned} I_{p,rms} &= \sqrt{\frac{1}{T_c}\int_o^{T_c} I_0^2 dt} \\ &= \sqrt{\frac{1}{T_c}\left[\int_o^{t_1} I_0^2 dt + \int_{t_2}^{T_c} I_0^2 dt\right]} \\ &= \sqrt{\frac{1}{T_c}\left[I_0^2 t_1 + I_0^2 (T_c - t_2)\right]} \\ &= I_0\sqrt{\frac{t_1 + T_c - t_2}{T_c}} = I_0\sqrt{1+\frac{t_1 - t_2}{T_c}} = I_0\sqrt{1-(1-D)} \\ &= I_0\sqrt{D} \end{aligned} \tag{4.35}$$

where t_1 and t_2 are dummy time variables corresponding to the switching angles α_1 and α_2.

Now, consider both of the cycles and apply the approach in (4.35), then

$$I_{2p,rms} = \sqrt{\frac{1}{2T_c}\left(\int_o^{2T_c} I^2 dt\right)} = \sqrt{\frac{1}{2}\left(I_0^2 D_1 + I_1^2 D_2\right)} \tag{4.36}$$

In (4.36), it is seen that as more cycles are added to the rms calculation, more $I_n^2 D_n$ terms are added in the parenthesis under the square root sign. If (4.36) is generalized for N cycles, the general rms equation becomes

$$I_{Np,rms} = \sqrt{\frac{1}{N}\left(I_0^2 D_1 + I_1^2 D_2 + \cdots + I_{N-1}^2 D_{N-1}\right)} = \sqrt{\frac{1}{N}\sum_{n=0}^{N-1} i_{o,n}^2 D_n} \tag{4.37}$$

where $N = \frac{f_c}{f_o} = \frac{T_o}{T_c}$ and it is assumed to be an integer.

The actual load current for all the phases is in sinusoidal form. Consider the phase *a* current,

$$i_a = I\sin(\theta_n - \phi) \tag{4.38}$$

where I is the peak load current,

$\theta_n = \frac{2\pi n}{N}$ n=0,1,2,…,N-1, and

ϕ is the phase angle

The other phase currents are $2\pi/3$ and $4\pi/3$ apart from the phase *a* current.

The devices in an inverter do not conduct at every switching cycle. The upper devices conduct when the load current is positive and the lower devices conduct when it is negative. The main switch *Q1* conducts current when the current is positive; thus, in angular terms it conducts from $\theta=\phi$ to $\theta=\pi+\phi$. Then

$$\begin{aligned} I\sin(\theta_n-\phi)&>0\\ 0&<\theta_n-\phi<\pi\\ \phi&<\theta_n<\pi+\phi\\ \phi&<\frac{2\pi n}{N}<\pi+\phi\\ \frac{\phi}{2\pi}N&<n<\frac{\pi+\phi}{2\pi}N \end{aligned} \tag{4.39}$$

Inserting (4.38) and (4.33) in (4.37) and setting the angle limits, *Q1* rms current can be calculated.

$$I_{Q_1,rms}=I\sqrt{\frac{1}{2N}\sum_{n=\frac{\phi}{2\pi}N}^{\left(\frac{\pi+\phi}{2\pi}\right)N}\sin^2\left(\frac{2\pi n}{N}-\phi\right)\left[1+M\sin\left(\frac{2\pi n}{N}\right)\right]} \tag{4.40}$$

For $f_c >> f_o$ (or N>>1), the summation in the above equation can be approximated by an integral:

$$\begin{aligned} I_{Q_1,rms}&\cong I\sqrt{\frac{1}{2\cdot 2\pi}\int_{\phi}^{\pi+\phi}\sin^2(\theta-\phi)(1+M\sin\theta)d\theta}\\ &=I\sqrt{\frac{1}{4\pi}\left(\frac{\pi}{2}+\frac{4}{3}M\cos\phi\right)}\\ &=I\sqrt{\frac{1}{8}+\frac{1}{3\pi}M\cos\phi} \end{aligned} \tag{4.41}$$

The duty ratio for diode D_4 was calculated before in (4.34) as D'. D_4 also conducts when the current is positive but when Q_1 is off; therefore, the only difference between the rms currents of these devices is the – sign in the duty ratio equation. Then, the rms current through D_4 is

$$I_{D_4,rms} = I\sqrt{\frac{1}{8} - \frac{1}{3\pi}M\cos\phi} \tag{4.42}$$

To find the MOSFET conduction losses, insert (4.41) in (4.23)

$$P_{cond,Q1} = I^2 \cdot R_{DS,on} \cdot \left(\frac{1}{8} + \frac{1}{3\pi}M\cos\phi\right) \tag{4.43}$$

Note that the rms current and the conduction losses of all the MOSFETs in the inverter are the same.

4.2.1.4.2 Switching losses

The switching losses of a MOSFET were derived in the previous chapter. Here the equation will be repeated for Q_1.

$$p_{Q_1} = f_c E_{tot} = f_c \frac{1}{3}\varepsilon_s E_c V \left(\frac{V}{BV}\right)^{1/2}\left[\frac{1}{(K_1 - 1)} + \frac{1}{(K_2 + 1)}\right] \tag{4.44}$$

where $K_1 = \frac{g_m(V_{GH} - V_{th})}{J}$ and $K_2 = \frac{g_m(V_{th} - V_{GL})}{J}$

This equation calculates the losses in one cycle; however, there are N cycles in

one output period, T_o, and the current varies in each cycle. Again, the averaging technique will be used to calculate the losses over T_o.

First, the sinusoidally varying current expression needs to be added to (4.44) through K_1 and K_2.

$$J = \frac{i_a}{A} = \frac{I\sin(\theta-\phi)}{A} = J'\sin(\theta-\phi) \tag{4.45}$$

where A is the device area and J' is the peak current density.

For simplicity, the constant terms in the above equations are assigned letters as follows:

$$H = f_c \frac{1}{3}\varepsilon_s E_c V\left(\frac{V}{BV}\right)^{1/2} \tag{4.46}$$

$$G_1 = g_m(V_{GH} - V_{th}) \tag{4.47}$$

$$G_2 = g_m(V_{th} - V_{GL}) \tag{4.48}$$

Inserting (25-28) into (4.29),

$$p_{Q_1}(\theta) = H\left(\frac{J'\sin(\theta-\phi)}{G_1 - J'\sin(\theta-\phi)} + \frac{J'\sin(\theta-\phi)}{G_2 + J'\sin(\theta-\phi)}\right) \tag{4.49}$$

Averaging (4.34) over T_o, MOSFET switching loss expression is obtained

$$
\begin{aligned}
P_{sw,Q_1} &= \frac{1}{N}\sum_{n=1}^{N} p_{Q_1}(\theta_n) \\
&\cong \frac{1}{2\pi}\int_{\phi}^{\pi+\phi} p_{Q_1}(\theta_n)\,d\theta \\
&= \frac{H}{2\pi}\left[\frac{G_1}{\sqrt{G_1^2 - J'^2}}\left(\pi + 2\tan^{-1}\left(\frac{J'}{\sqrt{G_1^2 - J'^2}}\right)\right) + \frac{G_2}{\sqrt{G_2^2 - J'^2}}\left(-\pi + 2\tan^{-1}\left(\frac{J'}{\sqrt{G_2^2 - J'^2}}\right)\right)\right]
\end{aligned}
\tag{4.50}
$$

In a simpler form, the above equation can also be interpreted and written in terms of angles. Consider the right triangles in Figure 4.21 and define the following angles:

$$
\beta = \cos^{-1}\left(\frac{\sqrt{G_1^2 - J'^2}}{G_1}\right) \tag{4.51}
$$

and

$$
\gamma = \cos^{-1}\left(\frac{\sqrt{G_2^2 - J'^2}}{G_2}\right) \tag{4.52}
$$

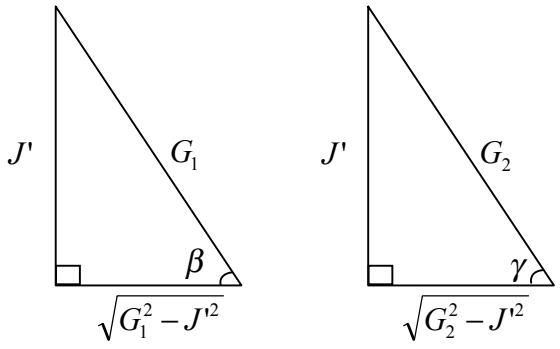

Figure 4.21: Triangles defined to simplify (4.50).

Using these angles, the following can be derived,

$$\tan^{-1}\left(\frac{J'}{\sqrt{G_1^2 - J'^2}}\right) = \beta \tag{4.53}$$

and,

$$\tan^{-1}\left(\frac{J'}{\sqrt{G_2^2 - J'^2}}\right) = \gamma \tag{4.54}$$

.

(4.50) can now be written in a simpler format in terms of angles.

$$P_{sw,\,Q1} = \frac{Hf_c}{2\pi}\left[\frac{1}{\cos\beta}(\pi + 2\beta) + \frac{1}{\cos\gamma}(-\pi + 2\gamma)\right] \tag{4.55}$$

Note that all six MOSFETs in a three-phase inverter have the same switching and conduction losses for a balanced three-phase load. The total MOSFET losses in an inverter can be calculated by adding $P_{cond,\,Q1}$ and $P_{sw,Q1}$ and multiplying the sum by six.

4.2.1.5 Diode losses

4.2.1.5.1 Conduction losses

As discussed in the previous chapter, a diode can be represented by its PWL model; therefore, the conduction losses of a diode consist of resistive losses and

losses due to the voltage drop. The expression for the conduction losses of diode D_4 are given by

$$P_{cond,D4} = I_{D4,rms}^2 \cdot R_D + I_{D4,av} \cdot V_D \tag{4.56}$$

The expression for $I_{D4,rms}$ was derived before and is repeated below for convenience

$$I_{D4,rms} = I\sqrt{\frac{1}{8} - \frac{1}{3\pi} M \cos\phi} \tag{4.57}$$

To calculate the second loss term in (4.56), it is required to calculate the average diode current. This derivation is similar to the prior rms derivation.

$$\begin{aligned} I_{D4,av} &= \frac{1}{N}\sum_{n=0}^{N-1} i_{o,n} D'_n \\ &\cong \frac{1}{2\pi}\int_{\phi}^{\pi+\phi} I\sin(\theta-\phi)\frac{1}{2}(1 - M\sin\theta)\,d\theta \\ &= I\left(\frac{1}{2\pi} - \frac{M\cos\phi}{8}\right) \end{aligned} \tag{4.58}$$

Then the power loss of a diode in a PWM inverter is expressed as

$$P_{cond,D4} = I^2 \cdot R_D \cdot \left(\frac{1}{8} - \frac{1}{3\pi} M\cos\phi\right) + I \cdot V_D \cdot \left(\frac{1}{2\pi} - \frac{1}{8} M\cos\phi\right) \tag{4.59}$$

4.2.1.5.2 Switching losses

The experimental switching loss data have been obtained in the previous chapter and plotted in Fig. 3.16. The linear approximations of the switching losses for a V_R=300V and f_c=20kHz can be found in (3.29) – (3.31). These equations are used as switching loss models and are implemented in SIMULINK thermal model of the traction drive.

4.2.1.6. Summary of loss equations

4.2.1.6.1. Diode

$$P_{cond,D4} = I^2 \cdot R_D \cdot \left(\frac{1}{8} - \frac{1}{3\pi} M \cos\phi\right) + I \cdot V_D \cdot \left(\frac{1}{2\pi} - \frac{1}{8} M \cos\phi\right) \tag{4.60}$$

$P_{sw,D4}$ is obtained from (3.29) – (3.31).

4.2.1.6.2. MOSFET

$$P_{cond,Q1} = I^2 \cdot R_{DS,on} \cdot \left(\frac{1}{8} + \frac{1}{3\pi} M \cos\phi\right) \tag{4.61}$$

$$P_{sw,Q1} = \frac{D}{2\pi}\left[\frac{C_1}{\sqrt{C_1^2 - J'^2}}\left(\pi + 2\tan^{-1}\left(\frac{J'}{\sqrt{C_1^2 - J'^2}}\right)\right) + \frac{C_2}{\sqrt{C_2^2 - J'^2}}\left(-\pi + 2\tan^{-1}\left(\frac{J'}{\sqrt{C_2^2 - J'^2}}\right)\right)\right] \tag{4.62}$$

4.2.1.6.3. Total inverter losses

The total inverter losses can be found by adding all the loss components and multiplying the sum by six.

$$P_{total,inverter} = 6 \cdot \left\langle \begin{array}{l} I^2 \cdot R_D \cdot \left(\frac{1}{8} - \frac{1}{3\pi} M \cos\phi \right) + I \cdot V_D \cdot \left(\frac{1}{2\pi} - \frac{1}{8} M \cos\phi \right) \\ + I^2 \cdot R_{DS,on} \cdot \left(\frac{1}{8} + \frac{1}{3\pi} M \cos\phi \right) \\ + P_{sw,D4} \\ + \frac{D}{2\pi} \left[\frac{C_1}{\sqrt{C_1^2 - J'^2}} \left(\pi + 2\tan^{-1} \left(\frac{J'}{\sqrt{C_1^2 - J'^2}} \right) \right) \right. \\ \left. + \frac{C_2}{\sqrt{C_2^2 - J'^2}} \left(-\pi + 2\tan^{-1} \left(\frac{J'}{\sqrt{C_2^2 - J'^2}} \right) \right) \right] \end{array} \right\rangle \quad (4.63)$$

Comparing (4.60) to (4.56), (4.60) looks like the conduction loss of a diode with PWL parameters of $R_D' = R_D \cdot \left(\frac{1}{8} - \frac{1}{3\pi} M \cos\phi \right)$ and $V_D' = V_D \cdot \left(\frac{1}{2\pi} - \frac{1}{8} M \cos\phi \right)$ carrying a dc current *I*. Additionally, comparing (4.61) to (4.23), (4.61) looks like the conduction loss of a MOSFET with $R_{DS,on}' = R_{DS,on} \cdot \left(\frac{1}{8} + \frac{1}{3\pi} M \cos\phi \right)$ carrying the same dc current *I*.

Using this reasoning, the conduction losses of one phase (two diodes and two MOSFETS) of a PWM inverter can be can be represented as an equivalent circuit

shown in Figure 4.22

where R_1 is a constant resistance,

$$R_1 = 2\frac{R_{DS,on} + R_D}{8}, \tag{4.64}$$

R_2 is a modulation index and phase angle dependent resistor,

$$R_2 = 2\left(\frac{R_{DS,on} - R_D}{3\pi}\right)M\cos\phi, \tag{4.65}$$

V_1 is a constant voltage source,

$$V_1 = 2\frac{V_D}{2\pi}, \tag{4.66}$$

and V_2 is a modulation index and phase angle dependent voltage source,

$$V_2 = -2\frac{V_D}{8}M\cos\phi \tag{4.67}$$

.

The equivalent circuit for the conduction losses of the whole inverter is same as the one in Figure 4.22 with each resistance and voltage value multiplied by three

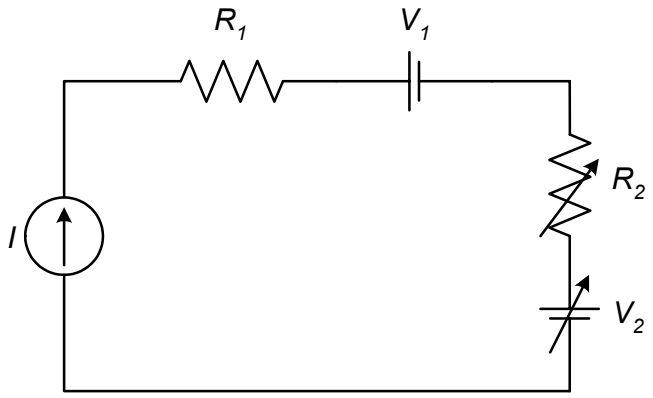

Figure 4.22: Equivalent circuit for the conduction losses.

to account for all three phases.

4.2.2. Results

An HEV traction drive was simulated over the FUDS cycle using ADvanced VehIcle SimulatOR (ADVISOR), which is a user-friendly conventional, electric or hybrid vehicle simulator package programmed in MATLAB/SIMULINK environment by the U.S. Department of Energy Hybrid Program at the National Renewable Energy Laboratory. As a result of simulation, motor torque and speed profiles sampled at 1Hz were obtained. From these profiles, current peak, I, modulation index, M, and phase angle, ϕ profiles were calculated assuming constant V/Hz control and using the following algorithm:

Algorithm to find I, M, and ϕ :

1. Get machine torque, T_e and speed, ω_r profiles from ADVISOR.
2. Machine input power can be calculated using the output power,

$$P_{in} = \frac{P_o}{\eta} = \frac{T_e \cdot \omega_r}{\eta} \tag{4.68}$$

3. Machine output frequency corresponding to the motor speed is

$$f_o = \frac{p}{2} \cdot \frac{\omega_r}{2\pi} \tag{4.69}$$

4. Then, the V/Hz constant is

$$K_v = \frac{\sqrt{\frac{3}{2}}\frac{4}{\pi}\frac{V_{dc}}{2}}{f_b} \tag{4.70}$$

where f_b is the base frequency.

Note that the constant V/Hz control in this study is assumed to be linear for simplicity. The numerator of (4.70) is the rms value of the fundamental voltage corresponding to the square wave operation

5. Rms line voltage at any output frequency can be calculated using the V/Hz constant

$$V_L = f_o \cdot K_v \tag{4.71}$$

6. $$I_L \cdot \cos\phi = \frac{P_{in}}{\sqrt{3}V_L} \tag{4.72}$$

7. $$I_L \cdot \sin\phi = I_m \tag{4.73}$$

where I_m is the magnetizing current of the machine.

8. $$I_L = \sqrt{(I_L \cdot \cos\phi)^2 + (I_L \cdot \sin\phi)^2} = \sqrt{\left(\frac{P_{in}}{\sqrt{3} \cdot V_L}\right)^2 + I_m^2} \tag{4.74}$$

9. Peak line current, $I = \sqrt{2}I_L$ (4.75)

10. $$\phi = \cos^{-1}\frac{I_L \cos\phi}{I_L} \tag{4.76}$$

11. Modulation index, $M = \dfrac{V_L}{\sqrt{\frac{3}{2}}\frac{4}{\pi}\frac{V_{dc}}{2}} = \dfrac{K_v \cdot f_o}{K_v \cdot f_b} = \dfrac{f_o}{f_b}$ (4.77)

This algorithm and the loss equations are implemented in SIMULINK (Figure 4.23) and the resulting model is simulated over the FUDS cycle.

The loss profiles of a diode and a MOSFET obtained as a result of this simulation are shown in Figure 4.24. In this figure, SiC diode losses are lower than Si diode losses mostly because the SiC diode has lower reverse recovery losses. On the other hand, SiC MOSFET losses are lower because the switching losses are similar but SiC MOSFET conduction losses are lower. The reason for lower

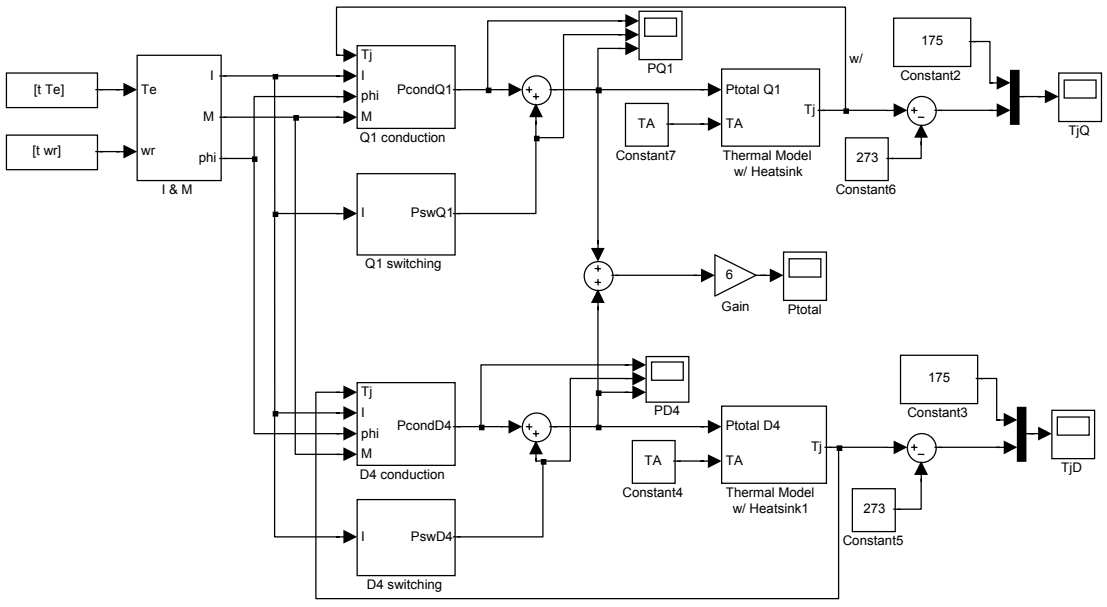

Figure 4.23: SIMULINK model of the traction drive thermal simulation.

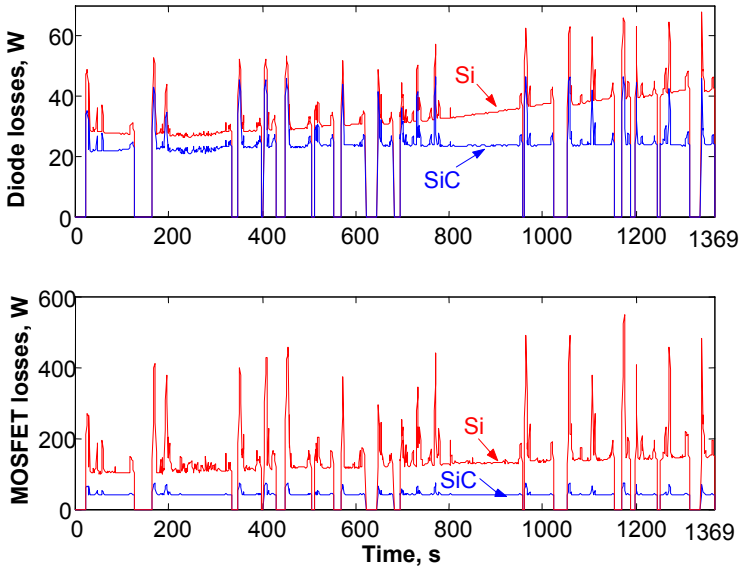

Figure 4.24: Total loss profile for a diode and a MOSFET.

conduction losses is the lower specific on-resistance ($R_{on,sp(Si)}$ = 180×10^{-3} Ω-cm^2, $R_{on,sp(4H\text{-}SiC)}$ = 0.3×10^{-3} Ω-cm^2).

Total energy loss (six diodes and six MOSFETs) is 925 W·s for the Si inverter and 338 W·s for the SiC inverter over the FUDS cycle. The corresponding motoring efficiency (Figure 4.25) of the Si inverter is 80–85%, while that of the SiC inverter is 90–95%. This is a 10% increase in the average efficiency. As a result, the battery in the HEV with the SiC inverter will need less charging than the one with the Si inverter.

The loss profiles in Figure 4.24 are fed to the thermal models of the devices. The resulting junction temperature profiles are shown in Figure 4.26. Normally, for

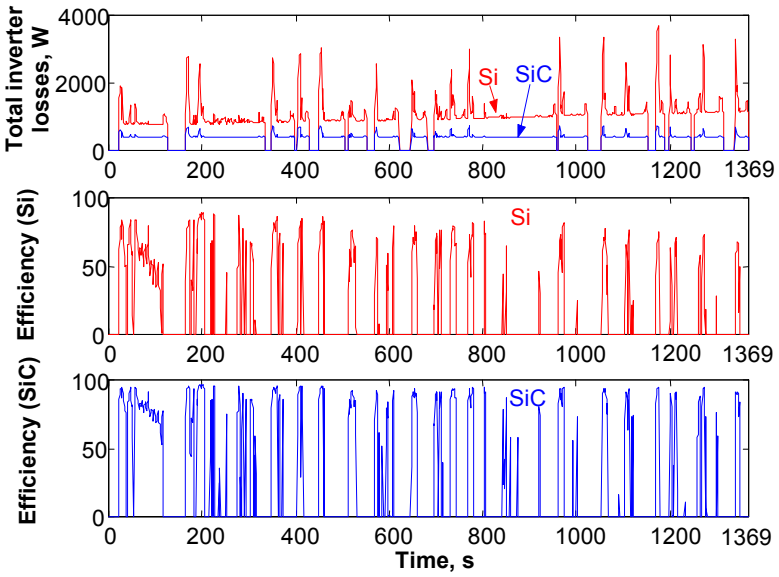

Figure 4.25: Total losses and the efficiency of the inverter over the FUDS cycle.

the kind of inverter in this study, water-cooled heatsinks are used. However, for the ease of calculation, natural air-cooled heatsinks are used to limit the junction temperature to 150°C for Si and 175°C for SiC. The latter temperature limit is found on the datasheet of the Infineon SiC Schottky diode used in this study [13]. The resulting heatsink volumes and masses for each device and each inverter are given in Table 4.4. Using SiC devices instead of their Si counterparts in an HEV traction drive reduces the size and weight of the heatsink to one-third. Note that a heatsink usually occupies one-third the volume of the converter and weighs more than the electronics.

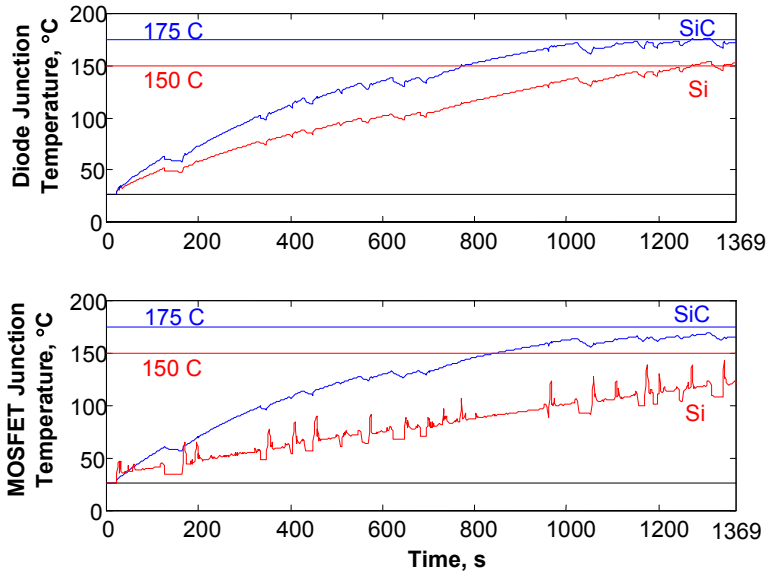

Figure 4.26: Junction temperature profiles of the diodes and MOSFETs in the three-phase inverter.

Table 4.4: Heatsink mass and volume for each device and inverter

	Volume (cm^3)	Mass (g)
Si diodes	444	1200
SiC diodes	162	450
Si MOSFETs	1554	4200
SiC MOSFETs	444	1200
Si inverter	***1998***	***5400***
SiC inverter	***606***	***1650***

Theoretically, SiC devices can work at higher temperatures. If new packaging techniques are developed such that these higher temperatures could be used as the temperature limits, then the amount of cooling required would be less, and more weight and volume savings would be possible.

4.3. Summary

In this chapter, models of two common converters in HEVs have been developed using the device models from Chapter 3. These converter models have been simulated to show the impact of SiC devices at the systems level.

The first one of these converters was an isolated full-bridge dc-dc converter shown in Fig. 4.1. The results of the simulation have shown that an all SiC-based dc-dc converter with a 20kHz switching frequency occupies 169cm^3 less volume and weighs 0.455kg less compared to an all Si-based one. With an increase in the switching frequency to 100kHz, the savings also increase to 1141 cm^3 of volume and 3.077kg of weight. Another benefit of the increased is the decrease in size of the passive components. The simulation results have shown that a five times increase in the switching frequency corresponds to a five times reduction in the size of the filter components and the high frequency transformer.

The results of the traction drive study, on the other hand, have shown that an all SiC-based traction drive inverter has on average ten percentage points higher efficiency because of the lower losses of the SiC power devices. Moreover, with the high-temperature operation capability of the SiC devices, they have less stringent cooling requirements. A HEV traction drive, with an all SiC inverter occupies 1392 cm^3 less space and weighs 3.75 kg less.

The weight reduction and efficiency increase result in an increase in the fuel economy of the vehicle and a longer battery lifetime.

The contributions in this chapter include development of SIMULINK loss models of a dc-dc converter and a traction drive; evaluation of SiC impact on a dc-dc converter's heatsink, filter, and, transformer size, and on a traction drive's heatsink size, efficiency, device losses, and junction temperature. Other contributions include the derivation of a physics-based average switching loss model of a MOSFET to be used in traction drive modeling, and development of an algorithm to find M, I, and ϕ from an induction machine torque and speed data. The final two contributions are the observation of the similarities between the averaging model and a MA model and expressing average modeling as a MA filter series, and the derivation of the equivalent circuit for the averaged conduction losses of an inverter.

Chapter 5

PARAMETRIC DEVICE STUDY

Materials and device researchers build switching devices for the circuits researchers use in their circuits, but they rarely know how and where the devices are going to be used. The circuits people, including power electronics researchers, take the devices as black boxes and use them in their circuits not knowing much about the inside of the devices. The best way to design optimum devices is an interactive design where people designing and building the devices have a close interaction with the people who use them.

This dissertation's scope covers the circuit aspects of the SiC power device development. As a contribution to the above-mentioned interactive design, in this chapter, the device parameters, which need to be improved in order to

design better devices, will be listed. Then the effects of these parameter improvements on the systems will be discussed.

5.1. Diodes

Some important diode parameters for power electronics systems are the breakdown voltage (BV), on resistance (R_D), built-in voltage (V_D), peak reverse recovery current (I_r), and reverse recovery time (t_{rr}).

5.1.1 Conduction loss parameters

5.1.1.1. Traction drive

A diode conduction loss expression for a traction drive inverter was derived in the previous chapter and it is repeated below.

$$P_{cond,D4} = I^2 \cdot R_D \cdot \left(\frac{1}{8} - \frac{1}{3\pi} M \cos\phi\right) + I \cdot V_D \cdot \left(\frac{1}{2\pi} - \frac{1}{8} M \cos\phi\right) \quad (5.1)$$

This equation consists of two parts, loss associated with the on resistance, R_D and loss associated with the voltage drop, V_D. Diodes with lower R_D and V_D would be preferable, but these parameters depend on similar device parameters e.g. both of these parameters depend on the doping densities. Higher doping density means lower R_D but higher V_D and lower breakdown voltage, BV; therefore, both R_D and V_D cannot be lowered at the same time, i.e. a trade-off is required.

Consider a 4H-SiC Schottky diode with a BV of more than 500V for a traction drive.

$$BV \approx \frac{\varepsilon_r E_c^2}{2qN_d} = \frac{1.3511\times10^{21}}{N_d} > 500V \text{ , and } N_d < 2.7\times10^{18} \tag{5.2}$$

The maximum doping density value to sustain the chosen BV is calculated above. The resistance value corresponding to this N_d is the minimum R_D. It cannot be decreased with doping any further, however, the doping density can still be selected lower than this value, which would increase BV, R_D, and decrease V_D. Then, the question is: Can modifying V_D and R_D decrease the conduction losses?

To answer this question, it is required to find how much a change in R_D and/or V_D will affect the conduction losses.

$$I^2 \cdot R_D \cdot \left(\frac{1}{8} - \frac{1}{3\pi} M\cos\phi\right) > ? < I \cdot V_D \cdot \left(\frac{1}{2\pi} - \frac{1}{8} M\cos\phi\right) \tag{5.3}$$

Rearranging terms and assuming $I \neq 0$,

$$I \frac{\left(\frac{1}{8} - \frac{1}{3\pi} M\cos\phi\right)}{\left(\frac{1}{2\pi} - \frac{1}{8} M\cos\phi\right)} > ? < \frac{V_D}{R_D} \tag{5.4}$$

$$I \cdot f(M\cos\phi) > ? < \frac{V_D}{R_D}$$

where $f(M\cos\phi)=\dfrac{\left(\frac{1}{8}-\frac{1}{3\pi}M\cos\phi\right)}{\left(\frac{1}{2\pi}-\frac{1}{8}M\cos\phi\right)}$, M is the modulation index, which varies between 0 and $4/\pi$ (square wave operation), and $cos\phi$ is the power factor, which varies between 0 and 1. The power factor of an induction machine is always lagging; assume that it is rated at 0.9.

$0 \le M \le \dfrac{4}{\pi}$ and $0 \le \cos\phi < 0.9$

Then,

$$0 \le M\cos\phi < \frac{3.6}{\pi} \tag{5.5}$$

and

$f(M\cos\phi)$ varies between 0.787 (no-load) and 0.215 (rated load) as shown in Figure 5.1.

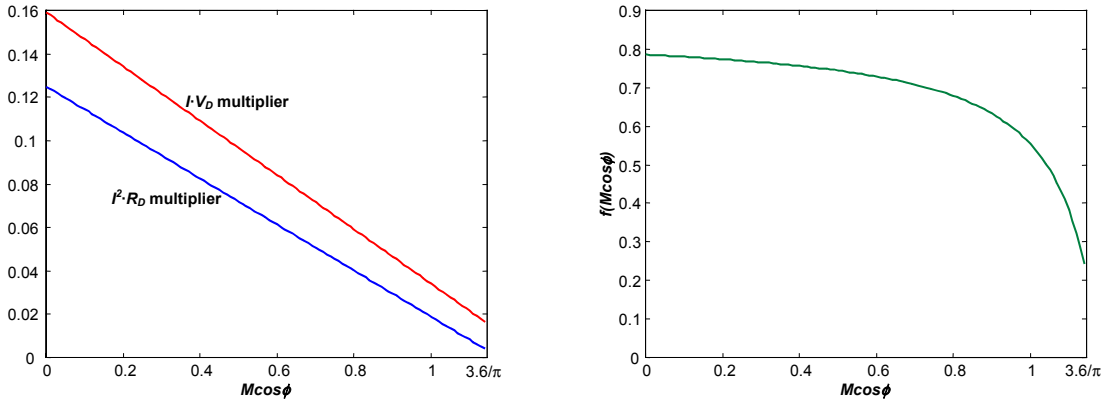

(a) (b)

Figure 5.1: The variation of *f(Mcosϕ)* with *Mcosϕ* **(a)** The denominator and the numerator of *f(Mcosϕ)* vs. *Mcosϕ* **(b)** *f(Mcosϕ)* vs. *Mcosϕ*.

At first glance, it might seem that because the $I \cdot V_D$ multiplier is larger than the $I^2 \cdot R_D$ multiplier at all $M\cos\phi$ values in Fig. 5.1, the V_D losses should always be higher. This observation would have been true if and only if V_D and the $I \cdot R_D$ product were equal. This, however, is not the case and that is why, all three of these variables are included in (5.4) to find under what conditions, what part of the conduction losses is higher.

For the traction drive in this application, the rated peak machine current is 136.28A, which makes $I \cdot f(M\cos\phi) = 136.28 \cdot 0.215 = 29.3A$. Ignoring the off condition, the minimum device current is the magnetizing current, which is 71A. During the magnetizing current operation, the phase angle is almost $\pi/2$ radians and the power factor is almost zero, then $I \cdot f(M\cos\phi) = 71 \cdot 0.787 = 55.9A$

Then considering (5.4)

- If $29.3A > \frac{V_D}{R_D}$, then the R_D losses are higher at all times, keep the doping density and R_D constant because decreasing R_D means decreasing BV, which cannot be allowed.
- If $55.9A < \frac{V_D}{R_D}$, then the V_D losses are higher at all times, decrease the doping density so that V_D will be smaller

- If $29.3A < \frac{V_D}{R_D} < 55.9A$, then it depends on the average current of operation.
  - A drive working around the rated value uses the condition

    $29.3A < \frac{V_D}{R_D}$, where V_D losses are higher, decrease the doping
  - A drive working with low or no-load uses the condition

    $\frac{V_D}{R_D} < 55.9A$, where R_D losses are higher, keep the doping as it is.

Fig. 5.2 displays the above statements on an R_D - V_D plane.

The V_D and R_D values of the SiC diode in this study are tabulated in Table 3.4 and shown as a small rectangular area in Fig. 5.2. Table 5.1 lists the corresponding V_D/R_D ratio at different operating temperatures.

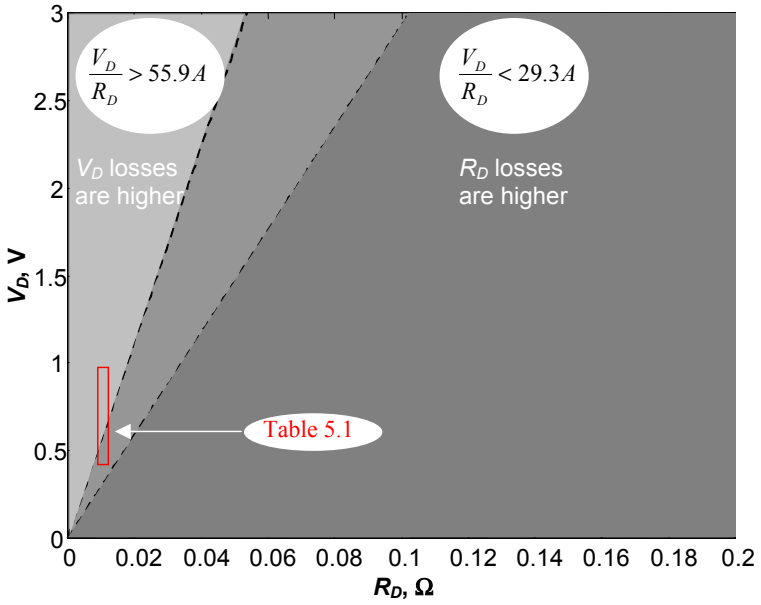

Figure 5.2: The R_D – V_D plane for the traction drive.

Table 5.1: SiC Diode PWL model parameters and V_D/R_D ratio.

T_{oven}, °C	R_D, mΩ	V_D, V	V_D/R_D,A
27	4.2	1.07	254
61	9.4	0.63	67
82	10.3	0.56	55
106	8.9	0.68	76
129	10.0	0.59	59
150	11.5	0.55	48
174	11.7	0.55	48
200	11.8	0.50	42
250	12.1	0.48	40

At temperatures up to and including 129°C, the V_D/R_D ratio is greater than 55.9A, therefore V_D losses are higher. At the other temperatures, the ratio is in between 29.3A and 55.9A. The traction drive will operate close to the rated operation of the induction machine; therefore, consider the comparison with 29.3A. For all the other temperatures, the ratio is greater than 29.3A; thus, the V_D losses are higher again.

As a conclusion for this case, if the doping concentration, N_d for the SiC diodes in this study is decreased, then V_D and the conduction losses decrease. The limit of this decrease is determined by the V_D/R_D ratio.

(5.4) can be used for any sinusoidal PWM application as long as the operation current, power factor, and modulation index information is available.

5.1.1.2. Dc power supply

The conduction loss expression for the dc-dc converter is as follows:

$$P_{cond} = d\left(I_D \cdot V_D + I_D^2 \cdot R_D\right) \tag{5.6}$$

Using the same approach as in the previous subsection, the dominant losses can be found as follows:

$$I_D^2 \cdot R_D > ? < I_D \cdot V_D$$
$$I_D > ? < \frac{V_D}{R_D} \quad . \tag{5.7}$$

What (5.7) means can be summarized as

- If $I_D > \frac{V_D}{R_D}$, then the resistive losses are higher, keep the doping and R_D constant because decreasing R_D means decreasing BV, which cannot be allowed.
    - If $I_D < \frac{V_D}{R_D}$, then the V_D losses are higher, decrease the doping.

According to Table (4.1), I_D varies between 47A and 119A, then applying the above criteria,

- If $47A > \frac{V_D}{R_D}$, then the first criterion applies.

- If $119A < \frac{V_D}{R_D}$, then the second criterion applies.

- If $47A < \frac{V_D}{R_D} < 119A$, then it depends on what limit the magnitude of the current is closer to for the majority of the time. For example, if the average load is varying or constant and is in a range between 3.5 and 5 kW, then the current is closer to the upper limit and the second criterion applies. If, on the other hand, the average load is in a range between 2 and 3.5 kW, then the current is closer to the lower limit and the first criterion applies.

This criteria presented here, can be applied to almost any dc-dc converter.

5.1.2. Switching loss parameters

The diode switching losses occur due to the reverse recovery of the diode, which is caused by the stored charge in the depletion region. Schottky diodes are majority carrier devices, so they do not have stored charge. As explained in Chapter 3, they display a reverse recovery like characteristic due to the ringing of the parasitics and the internal pn junction due to the p-rings.

For Schottky diodes, the switching losses can be reduced either by reducing the parasitic elements or improving the reverse recovery characteristics of the pn junction formed by the p-rings.

Diode switching loss expression was derived in Chapter 3 using Figure 3.9.

$$P_{rr} = f_c \frac{V_R}{2S}\left(\frac{dI_F}{dt}\right)\left(\frac{St_{rr}}{S+1}\right)^2 \tag{5.8}$$

In this expression all the parameters except S and t_{rr} are circuit dependent. These two parameters can be expressed [40] in other device parameters for a pn diode as follows,

$$S = \frac{2W_d}{b} - 1 \tag{5.9}$$

$$t_{rr} = \frac{2bW_d}{D_n} \tag{5.10}$$

where D_n is the electron diffusion constant ($D_n = \frac{kT}{q}\mu_n$), W_d is the width of the drift region, and b is a distance in the drift region measured from the p^+n^- junction $b = \frac{2qAD_n[n(0) - n^*]}{I_F}$ as shown in Fig. 5.3, $n(0)$ is the carrier density at the p^+n^- junction when the diode is on, and n^* is the average carrier concentration in the n^- region.

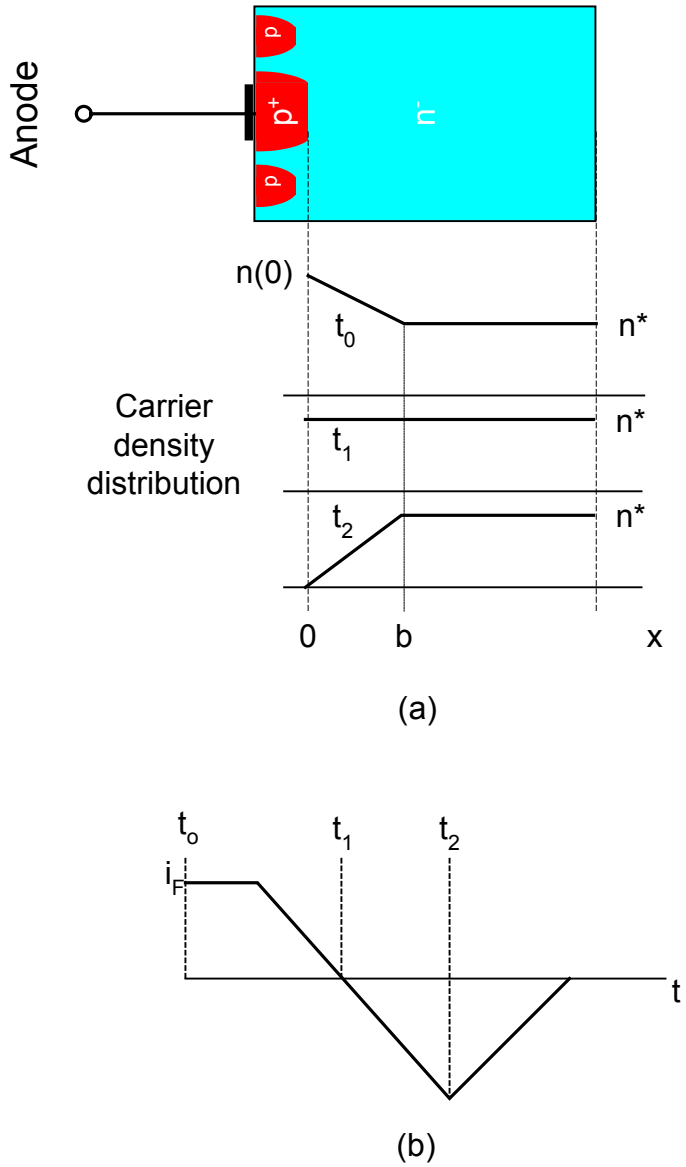

Figure 5.3: Carrier distribution in a diode during turn-off **(a)** Linearized carrier density distribution of a diode at different time instants **(b)** Linearized turn-off current waveform of the diode.

Gathering the S and t_{rr} related terms in (5.8) and inserting (5.9) and (5.10), the following is obtained.

$$\frac{1}{S}\left(\frac{St_{rr}}{S+1}\right)^2 = \frac{St_{rr}^2}{(S+1)^2} = \frac{\left(\frac{2W_d}{b}-1\right)\frac{4b^2W_d^2}{D_n^2}}{\frac{4W_d^2}{b^2}} = \frac{2W_d-b}{b}\frac{4b^4}{D_n^2} = \frac{(2W_d-b)b^3}{D_n^2} \tag{5.11}$$

Therefore, decreasing b and/or W_d can decrease the switching losses and b can be decreased by increasing the area and/or $[n(0)-n^*]$.

Note that the conclusions here also apply to the dc-dc converter, because (5.8) represents a switching cycle independent of the application.

5.2 MOSFETS

The following study will focus on the traction drive but the conclusions derived can also be applied to the dc-dc converter.

5.2.1. Conduction loss parameters

The conduction loss expression of a MOSFET in a traction drive is derived in Chapter 4 and it is repeated below for convenience.

$$P_{cond,Q1} = I^2 \cdot R_{DS,on} \cdot \left(\frac{1}{8} + \frac{1}{3\pi} M \cos\phi\right) \tag{5.12}$$

The only device related parameter in this expression is $R_{DS,on}$, which can be represented in other device parameters as follows

$$R_{DS,on} \approx R_{on,sp} = \frac{4BV^2}{\varepsilon_s \mu E_c^3} \tag{5.13}$$

for a device with 1 cm^2 area where $R_{on,sp}$ is the specific on resistance of the MOSFET drift region and ε_s, E_c, and μ are material related constants.

(5.13) is a rough estimate of a MOSFET resistance which also contains other resistive components like the channel resistance and the contact resistance. The drift resistance cannot be changed much; however, the channel and contact resistances can be lowered with more research.

5.2.2 Switching loss parameters

The energy loss equation of a MOSFET has been shown in Chapter 3 and is repeated below,

$$E_{tot} = E_{on} + E_{off} = \frac{1}{3}\varepsilon_s E_c V \left(\frac{V}{BV}\right)^{1/2}\left[\frac{1}{(K_1 - 1)} + \frac{1}{(K_2 + 1)}\right] \tag{3.35}$$

where $K_1 = \dfrac{g_m(V_{GH} - V_{th})}{J}$ and $K_2 = \dfrac{g_m(V_{th} - V_{GL})}{J}$

If (3.35) is rearranged, (5.14) is obtained.

$$E_{tot} = \frac{1}{3}\varepsilon_s E_c V \left(\frac{V}{BV}\right)^{1/2}\left[\frac{J}{(g_m(V_{GH} - V_{th}) - J)} + \frac{J}{(g_m(V_{th} - V_{GL}) + J)}\right] \tag{5.14}$$

The most important parameter contributing to the MOSFET switching energy loss is the transconductance g_m. This parameter can be represented as follows [41],

$$g_m = \mu \frac{w}{l} C_{ox} V_D = \mu \frac{w}{l} \left(\varepsilon_{ox} \frac{A_{ox}}{t_{ox}} \right) V_D \tag{5.15}$$

where μ is the mobility,

w is the channel width,

l is the channel length,

C_{ox} is the oxide capacitance,

V_D is the drain voltage,

ε_{ox} is the oxide dielectric constant,

t_{ox} is the oxide thickness, and

A_{ox} is the oxide area.

In (5.15), μ and ε_{ox} are material dependent; therefore, for a specific application, four device parameters affect the transconductance, w, A_{ox}, l, and t_{ox}. The first two of these parameters are directly proportional to g_m and the others are indirectly proportional to it.

- Decreasing t_{ox} increases g_m but t_{ox} has to be certain size to be able to support the rated gate voltage; it cannot be changed much.
- Decreasing l decreases g_m but value of l limited by the technology.

- Increasing A_{ox} increases g_m but A_{ox} depends on the device area; it cannot be changed independently.
- Increasing w increases g_m. To increase w, the device area has to be increased proportionally.

As a summary, to decrease the MOSFET switching losses, g_m needs to be increased. Increasing the device's area and consequently increasing A_{ox} and w seem to be the best method to do this.

5.3. Summary

In this chapter, losses of the devices in a traction drive are investigated as functions of device parameters. Some modifications to device parameters are suggested to improve the losses in this drive. The next step is for the device researchers to consider these suggestions and evaluate the viability of these modifications.

The interaction of device and power electronics researchers will be extremely useful in producing the application specific power devices designed for optimum performance. This chapter is the first step to achieving this goal.

Chapter 6

CONCLUSIONS

SiC is a material with superior electrical properties compared with Si; therefore, SiC-based power devices will have a great impact on the future of power electronics. SiC carbide devices are in their infancy but they are still surpassing the mature devices of the Si technology. When this study started, SiC research was limited to device research labs at the universities and companies. SiC research has gained a momentum in the last year and a half with the introduction of the first commercial SiC power devices.

To complement the research around the globe, in this dissertation, system impact of SiC power electronics on transportation applications has been investigated. First, the superiority of SiC over Si has been explained and examples of some SiC

power devices have been listed in comparison with their Si counterparts. Then, models of Si and SiC diodes and MOSFETs have been derived, and these models have been used in system simulations. Finally, a parametric device study has been added to show ways to improve the performance of power devices in order to get more optimum and application specific power devices.

Experimental studies, in this dissertation, have shown that SiC Schottky diode conduction losses are higher than those of Si pn diode at higher temperatures (>55°C). However, SiC diode switching losses have been found to be less than those of the Si diode at any temperature in the range tested. Moreover, these SiC diode switching losses did not change with temperature.

Simulation studies have shown that by simply replacing Si power devices with their SiC counterparts, significant mass and volume savings could be achieved. For example, the mass and volume of a 30 kW traction drive decreases by 3750g and 1392 cm^3 if SiC devices are used. For a 5 KW power supply, the reduction in mass and volume is 455g and 169 cm^3 for a switching frequency of 20 KHz. The savings increase with increased switching frequency, e.g. if the switching frequency is increased to 100kHz, then the savings on the power supply are 3077 g and 1141 cm^3. More of these results can be seen in [43-48].

This dissertation is unique for being a systems study of SiC devices' impact. Before this study, all the research had been focused on device research and some converter application.

6.1. The main contributions of this study

- A survey of the state-of-the art in SiC power device technology.
- Development of an experimental diode modeling procedure including a method to scale 10 A diodes to 200 A.
- Application of Genetic Algorithm to model diodes.
- Developing a SIMULINK loss model of a dc-dc converter.
- Evaluation of SiC impact on a dc-dc converter's heatsink, filter, and, transformer size.
- Observation of the similarities between the averaging model and a MA model. Expressing average modeling as a MA filter series.
- Derivation of physics-based average switching loss model of a MOSFET.
- Derivation of the equivalent circuit for the average conduction losses of an inverter.
- Developing an algorithm to find M, I, and ϕ from an induction machine torque and speed.
- Developing a SIMULINK loss model of a traction drive.

- Evaluation of SiC impact on a traction drive's heatsink size, efficiency, device losses, and junction temperature.
- Isolating the parameters affecting the device losses. Suggesting modifications to the parameters to improve the performance of diodes and MOSFETs.
- Developing a modular, easy to understand SIMULINK induction motor model from flux linkage modeling equations.

6.2. Recommended future work

In this section, recommendations for both circuit and device related future work will be given in the following subsections.

6.2.1. Circuits related future work

- This study has been based on individual device models derived from experimental results and theoretical equations, which are used in computer simulations to show the system impact of SiC power electronics. Validation of the simulation results requires building the power converters described here and comparing the results. As mentioned earlier, commercial SiC MOSFETs and higher current rated SiC diodes are still not available. However, instead of waiting for these devices to be

available, 10A SiC Schottky diodes used in this study can be inserted in Si MOSFET power converters and small scale results of the SiC diode impact can be obtained. These results can then be scaled and compared with the simulation results.

- In this study, transportation applications are used to show the impact of SiC power electronics. As explained in the Chapter 1, SiC power electronics will also have great benefits on other areas like aerospace and power system. These benefits are mentioned in the literature but no quantitative benefit analysis can be found. Not all the results of this dissertation can be applied to other areas; therefore, more application specific systems studies like this one have to be done.

6.2.2. *Device research*

- In Chapter 5, as a result of a parametric study, some recommendations for device modifications have been given. Semiconductor devices are complex structures; therefore, there are limitations to how much each parameter can be modified. To complete this parametric study, it is required for a device researcher to go through these recommendations and come up with a study showing which one of them are feasible and which ones are

not. This study then would complete the feedback loop initiated to design devices optimum for transportation applications.

REFERENCES

[1] W.J. Choyke and R. P. Devaty, "SiC - The power semiconductor for the 21st century: A materials perspective," *Naval Research Reviews*, vol. 51, no. 1, pp. 4-12, 1999.

[2] http://www.ifm.liu.se/matephys/AAnew/research/sicpart/sicindex.html

[3] A. K. Agarwal, s. S. Mani, S. Seshadri, J. B. Cassady, P. A. Sanger, and C. D. Brandt, N. Saks, "SiC Power Devices," *Naval Research Reviews*, vol. 51, no. 1, pp. 14-21, 1999.

[4] http://www.eeenet.org/figs_of_merit.asp

[5] K. Shenai, R. S. Scott, and B. J. Baliga, "Optimum semiconductors for high power electronics," *IEEE Transactions on Electron Devices*, vol. 36, no. 9, pp. 1811-1823, September 1989.

[6] N. Mohan, T.M. Undeland, and W. P. Robbins, *Power Electronics*, 2nd Edition, John Wiley & Sons Inc., New York, 1995.

[7] M. Bhatnagar and B. J. Baliga, "Comparison of 6H-SiC, 3C-SiC, and Si for power devices," *IEEE Trans. on Electron Devices*, vol. 40, No. 3, pp.645-655, March 1993.

[8] http://www.ecn.purdue.edu/WBG/Data_Bank/Best_Performance.html

[9] H. Matsunami, "Progress in Wide Bandgap Semiconductor SiC for Power Devices," *Proceeding of the IEEE International Symposium on Power Semiconductor Devices & ICs*, pp. 3-9, 2000.

[10] J. W. Palmour, R. Singh, R. C. Glass, O. Kordina, and C. H. Carter, Jr., "Silicon Carbide Power Devices," *Proceeding of the IEEE International Symposium on Power Semiconductor Devices & ICs*, pp. 25-32, 1997.

[11] A. Itoh, T. Kimoto, and H. Matsunami, "Excellent reverse blocking characteristics of high-voltage 4H-SiC Schottky rectifiers with boron-implanted edge termination," *IEEE Electron Device Letters*, vol. 17, no. 3, pp. 139–141, March 1996.

[12] T. Kimoto, Q. Wahab, A. Ellison, U. Forsberg, M. Tuominen, R. Yakimova, A. Henry, and E. Janzen, "High Voltage (>2.5kV) 4H-SiC Schottky Rectifiers Processed on Hot-Wall CVD and High-Temperature CVD Layers," *Material Science Forum*, vol. 264-268, pp. 921, 1998.

[13] http://www.infineon.com/

[14] Y. Sugawara, D. Takayama, K. Asano, R. Singh, J. Palmour, and T. Hayashi, "12-19kV 4H-SiC pin diodes with low power loss," *Proceeding of the IEEE International Symposium on Power Semiconductor Devices & ICs*, pp. 27-30, 2001.

[15] Y. Sugawara and K. Asano, "1.4 kV 4H-SiC UMOSFET with low specific on-resistance," *Proceeding of the IEEE International Symposium on Power Semiconductor Devices & ICs*, pp. 119–122, 1998.

[16] N. S. Rebello and F. S. Shoucair, "6H silicon carbide MOSFET modeling for high temperature analogue integrated circuits (25-500°C)," *IEE Proceedings- Circuits Devices Systems*, vol. 143, no. 2, pp. 115-122, April 1996.

[17] W. Wondrak, R. Held, E. Niemann, and U. Schmid, "SiC devices for advanced power and high temperature applications," *IEEE Transactions on Industrial Electronics*, vol. 48, no. 2, pp. 307-308, April 2001.

[18] H. Lendenmann, F. Dahlquist, N. Johansson, P. Bergman, H. Bleichner, and C. Ovren, "Performance and reliability of high power SiC diodes," *Future Electron Devices*, vol. 11, no. 2, pp. 113-118.

[19] M. Shanbhag, T. P. Chow, and M. S. Adler, "Reliability testing of SiC high voltage power devices," *Proceedings of Center for Power Electronic Systems (CPES) Annual Seminar*, pp. 487-490, 2001.

[20] A. R. Hefner, R. Singh, J. S. Lai, D. W. Berning, S .Bouche, and C. Chapuy, "SiC Power diodes provide breakthrough performance for a wide range of applications," *IEEE Transactions on Power Electronics*, vol. 16, no.2, pp. 273-280, March 2001.

[21] C. Winterhalter, H.-R. Chang, and R. N. Gupta, "Optimized 1200 V Silicon Trench IGBTs with SiC Schottky Diodes," *Proceedings of the Annual Meeting of the IEEE Industry Applications Society*, pp. 2928-2933, 2000.

[22] R. Singh, S.-H. Ryu, J. W. Palmour, A. R. Hefner, and J. Lai, "1500V, 4 amp 4H-SiC JBS diodes," *Proceeding of the IEEE International Symposium on Power Semiconductor Devices & ICs*, pp. 101-104, 2000.

[23] A. Hefner, D. Berning, J. S. Lai, C. Liu, and R. Singh, "Silicon Carbide merged PiN Schottky diode switching characteristics and evaluation for power supply applications," *Proceedings of the Annual Meeting of the IEEE Industry Applications Society*, pp. 2948-2954, 2000.

[24] A. Elasser, M. Kheraluwala, M. Ghezzo, R. Steigerwald, N. Krishnamurthy, J. Kretchner, and T. P. Chow, "A comparative evaluation of new silicon carbide diodes and state-of-the-art silicon diodes for power electronic applications," *Proceedings of the Annual Meeting of the IEEE Industry Applications Society*, pp. 341-345, 1999.

[25] M. Trivedi, K. Shenai, and P. G. Neudeck, "High-speed switching performance and buck converter operation of 4H-SiC diodes," *Proceedings of IEEE/Cornell Conference on High Performance Devices*, pp. 69-78, 2000.

[26] V. R. Garuda, M. K. Kazimierczuk, M. L. Ramalingam, C. Tunstall, and L. Tolkkinen, "High-temperature performance characterization of buck

converter using SiC and Si devices," *Proceedings of IEEE Power Electronics Specialist Conference*, pp. 1561-1567, 1998.

[27] W. Wright, J. Carter, P. Alexandrov, M. Pan, M. Weiner, and J. H. Zhao, "Comparison of Si and SiC diodes during operation in three-phase inverter driving ac induction motor," *IEE Electronics Letters*, vol. 37, no. 12, pp. 787-788, June 2001.

[28] J. S. Lai, X. Huang, H. Yu, A.R. Hefner, D. W. Berning, and R. Singh, "High current SiC JBS diode characterization for hard- and soft-switching application," *Proceedings of the Annual Meeting of the IEEE Industry Applications Society*, pp. 384-390, 2001.

[29] M. Trivedi and K. Shenai, "Hard- and soft-switching buck converter performance of high-voltage 4H-SiC and Si PiN diodes," *Proceedings of the Annual Meeting of the IEEE Industry Applications Society*, pp. 391-395, 2001.

[30] M. Coyaud, J.-P. Ferrieux, and Ch. Schaeffer, "Performances of SiC Schottky diodes in power correction," *Proceedings of the Annual Meeting of the IEEE Industry Applications Society*, pp. 370-375, 2001.

[31] L. Lorenz, G. Deboy, and I. Zverev, "Matched pair of CoolMOS™ transistor with SiC-Schottky diode- advantages in application," *Proceedings of the Annual Meeting of the IEEE Industry Applications Society*, pp. 376-383, 2001.

[32] Q. Huang and B. Zhang, "Comparing SiC switching power devices: MOSFET, NPN transistor, and GTO transistor," *Solid State Electronics*, Pergamon Press, pp. 325-340, 2000.

[33] B. Ozpineci, *Studies on a Performance Enhanced DC-HFAC-AC Converter for an AC drive*, A Master's Thesis, May 1998.

[34] P. D. Evans and B. Heffernan, "Electromagnetic considerations in power electronic converters," *Proceedings of the IEEE*, vol. 89, no. 6, pp. 864-875, June 2001.

[35] A. W. Lotfi and M. A. Wilkowski, "Issues and advances in high-frequency magnetics for switching power supplies," *Proceedings of the IEEE*, vol. 89, no. 6, pp. 833-845, June 2001.

[36] K. Berringer, J. Marvin, and P. Perruchoud, "Semiconductor power losses in ac inverters," *IEEE IAS Annual Meeting Conf Proc.*, pp. 882-888, 1995.

[37] W. Kolar, H. Ertl, and F. C. Zach, " How to include the dependency of the $R_{DS(on)}$ of the power MOSFETs on the instantaneous value of the drain current into the calculation of the conduction losses of high-frequency three-phase PWM inverters," *IEEE Transactions on Industrial Electronics*, vol. 45, no. 3, pp. 369-375, June 1998.

[38] B. K. Bose, *Modern Power Electronics and AC Drives*, International Inc., New Jersey, 2001.

[39] A. V. Oppenheim and R. W. Schafer, *Discrete-Time Signal Processing*,

Prentice Hall International Inc., New Jersey, 1989.

[40] B. J. Baliga, *Power Semiconductor Devices*, PWS Publishing Company, Boston, 1996.

[41] D. A. Grant and J. Gowar, *Power MOSFETS-Theory and Applications*, John Wiley & Sons, New York, 1989.

[42] C. Houck, J. Joines, and M. Kay, *The Genetic Algorithm Operation Toolbox (GAOT) for Matlab 5*, http://www.ie.ncsu.edu/mirage/GAToolbox/gaot

[43] B. Ozpineci, L. M. Tolbert, S. K. Islam, and Md. Hasanuzzaman, "Silicon carbide power devices and their impact on power electronics systems," To be presented at The 37th Annual Meeting of the *IEEE Industry Applications Society (IAS'02)*, October 13-18, 2002.

[44] B. Ozpineci, L. M. Tolbert, S. K. Islam, and F. Z. Peng, "Testing, characterization, and modeling of SiC diodes for transportation applications, " To be presented in *IEEE Power Electronics Specialists Conference (PESC'02)*, June 23-27, 2002.

[45] L. M. Tolbert, B. Ozpineci, S. K. Islam, and F. Z. Peng, "Impact of SiC power electronics for hybrid electric vehicles, " To be presented in *SAE Future Car Congress*, June 3-5, 2002.

[46] B. Ozpineci, L. M. Tolbert, S. K. Islam, and Md. Hasanuzzaman, "System Impact of Silicon Carbide (SiC) Power Devices," Accepted to be published in the *International Journal of High Speed Electronics and Systems.*

[47] B. Ozpineci, L. M. Tolbert, S. K. Islam, and Md. Hasanuzzaman, "System Impact of Silicon Carbide (SiC) Power Devices," *Advanced Workshop on 'Frontiers of Electronics' (WOFE'02)*, January 6 -11, 2002, St. Croix, VI, 2002.

[48] B. Ozpineci, L. M. Tolbert, S. K. Islam, and Md. Hasanuzzaman, "Effects of Silicon Carbide (SiC) Power Devices on PWM Inverter Losses," *The 27th Annual Conference of the IEEE Industrial Electronics Society (IECON'01)*, November 29 - December 2, Denver, Colorado, pp. 1187-1192.

APPENDIX

Appendix A

CURVE FITTING USING GENETIC ALGORITHMS

For any optimization application, Genetic Algorithm (GA) is an easy to apply tool with no need for complicated mathematical algorithms, which are not always efficient. In this study, GA optimization will be applied to the diode parameter extraction problem.

To obtain diode parameters from the experimental data requires fitting the diode equation to the experimental data. Commercial PSpice software can do this extraction easily with its "Model Editor" interface, but professional version Pspice software costs a lot of money, and the interface does not come fully functional with the free student version. Moreover, the experimental diode data at different temperatures cannot be used in the "Model Editor" to extract

temperature dependent diode parameters. GA, being free, easy to configure, and flexible is the optimum choice for this application. The following sections will explain GA and its application to curve fitting.

A.1. Genetic Algorithm

Genetic Algorithm is a computational model that solves optimization problems by imitating genetic processes and the theory of evolution. It imitates biological evolution by using genetic operators like reproduction, crossover, mutation, etc.

Optimization in GA means maximization; therefore, in cases where minimization is required, the negative or the inverse of the function to be optimized is used. Inverse can only be used if it is certain that the function will never be equal to zero.

To minimize a function, $f(x_1,x_2,\ldots,x_k)$ using GA, first, each x_i is coded as a binary or floating-point string of length m. In this study, a binary string is preferred, e.g.

$$\begin{aligned} x_1 &= \lfloor 10001\ldots01001 \rfloor \\ x_2 &= \lfloor 00101\ldots11110 \rfloor \\ &\ldots\ \ldots\ \ldots \\ x_k &= \lfloor 11110\ldots01011 \rfloor \end{aligned} \qquad \text{(A.1)}$$

The set of $\{x_1, x_2,\ldots,x_k\}$ is called a chromosome and x_i are called genes. The algorithm works as follows:

1-Initialize population:

Set a population size, N, i.e. the number of chromosomes in a population. Then initialize the chromosome values randomly. If known, the range of the genes should be utilized for initialization.

$$\text{Population, } P=\begin{Bmatrix} x_{1,1},x_{2,1},\ldots,x_{k,1} \\ x_{1,2},x_{2,2},\ldots,x_{k,2} \\ \cdots\ \cdots\ \cdots \\ x_{1,N},x_{2,N},\ldots,x_{k,N} \end{Bmatrix} \tag{A.2}$$

2-Evaluate each chromosome

Use the function in the problem to evaluate the fitness value (FV) of each chromosome,

$$FV=\frac{1}{f(x_1,x_2,\ldots,x_k)} \tag{A.3}$$

Add all the FVs to get the total fitness. Divide each FV by the total FV and find the probability of selection, p_i, for each chromosome. The integer part of the product, p_iN gives the number of descendents from each chromosome. At the end, there should be N descendent chromosomes. If the number of descendents calculated is less then N, the rest of the descendents are found randomly considering the reproduction probabilities, p_i of each chromosome.

3- Crossover Operation

A floating number (between 0 and 1) for each chromosome is assigned randomly. If this number is smaller than a pre-selected crossover probability, this chromosome goes into crossover. The chromosomes undergoing crossover are paired randomly. In this case assume x_1 and x_2 are paired. The crossing point is randomly selected, assume 3 in this case.

Then, before crossover,

$$\begin{aligned} x_1 &= \lfloor \mathbf{100}01\ldots01001 \rfloor \\ x_2 &= \lfloor \mathbf{001}01\ldots11110 \rfloor \end{aligned} \tag{A.4}$$

and after crossover,

$$\begin{aligned} x_1 &= \lfloor \mathbf{100}01\ldots11110 \rfloor \\ x_2 &= \lfloor \mathbf{001}01\ldots01001 \rfloor \end{aligned} \tag{A.5}$$

As seen above, the bits after the 3rd one are exchanged.

4- Mutation Operation:

A floating number (between 0 and 1) for each bit is assigned randomly. If this number is smaller than a pre-selected mutation probability, this bit mutates. Assume that the 2nd and 4th bits of x_1 and 2nd, 3rd and 5th bits of x_2 need to be mutated.

Then, before mutation and after crossover,

$$\begin{aligned} x_1 &= \left[1\mathbf{000}1\ldots11110\right] \\ x_2 &= \left[0\mathbf{01}0\mathbf{1}\ldots01001\right] \end{aligned} \tag{A.6}$$

and after mutation,

$$\begin{aligned} x_1 &= \left[1\mathbf{1}0\mathbf{1}1\ldots11110\right] \\ x_2 &= \left[0\mathbf{1000}\ldots01001\right] \end{aligned} \tag{A.7}$$

Finally, the new population is ready for another cycle of genetic algorithm. The algorithm runs a certain number of times as required by the user. At the end, the chromosome with the maximum *FV* is the answer.

A.2. Curve fitting using GA

In this application, the parameters to be extracted are the constants, R_s, I_s, and n in the diode equation in (3.8), so that the experimental data (u_i,v_i) can be fitted to the diode equation given in the explicit form below.

$$V = \frac{nkT}{q}\ln\left(\frac{I}{I_s}\right) + R_s I \tag{A.8}$$

which in terms of u and v is

$$v_f(u_i) = \frac{nkT}{q}\ln\left(\frac{u_i}{I_s}\right) + R_s u_i \tag{A.9}$$

The chromosomes have three genes, the values for R_s, I_s, and n in binary format and the population consists of ten of these chromosomes.

Curve fitting like any GA application requires a function to calculate the fitness value of each chromosome. This function, in this case, is the negative sum-squared error between the data points and the fitted function given below

$$f = -\sum_{i=1,2,..} \left[v_f(u_i) - v(u_i) \right]^2 \tag{A.10}$$

where $(u_i, v(u_i))$ are ordered experimental diode data pairs and $v_f(u_i)$ are the fitted function values.

The maximum value f can get is zero; therefore, as the curve fitting gets better, f will approach zero. At then end of GA iterations, the chromosome with the highest (or the closest to zero) f value will include the answer genes. Results are shown in Chapter 3.

The GA software used is the Genetic Algorithm Optimization Toolbox (GAOT), which is a MATLAB toolbox that consists of all the MATLAB functions required for any GA application. It is freely available on the internet at [42].

Appendix B

INDUCTION MACHINE SIMULATION

Usually when a machine is simulated in PSpice, its steady state model is used, but for electrical drive studies, the transient behavior is also important. One advantage of SIMULINK over circuit simulators like PSpice is that it is easy to model the transients of electrical machines and drives and to include drive controls in the simulation. As long as the equations are known, anything can be modeled in SIMULINK. However, the equations by themselves are not enough; some experience with differential equation solving is required.

SIMULINK induction motor models are available in the literature, but either they are too complicated to understand or they appear to be black-boxes with no internal details. In this appendix, a modular, easy to understand SIMULINK

induction motor model will be described.

B.1 Induction motor model

The inputs of an induction machine model are the three-phase voltages and their fundamental frequency. The outputs, on the other hand, are the three-phase currents, the output torque, and the rotor speed. The induction machine model in Figure B.1 consists of five blocks: the o-n conversion, abc-syn conversion, syn-abc conversion, unit vector calculation, and the induction machine d-q model blocks. The following subsections will explain each block.

B.1.1. o-n conversion block

This block is required only if an isolated neutral system is being simulated, otherwise it can be bypassed. This transformation done by this block can be

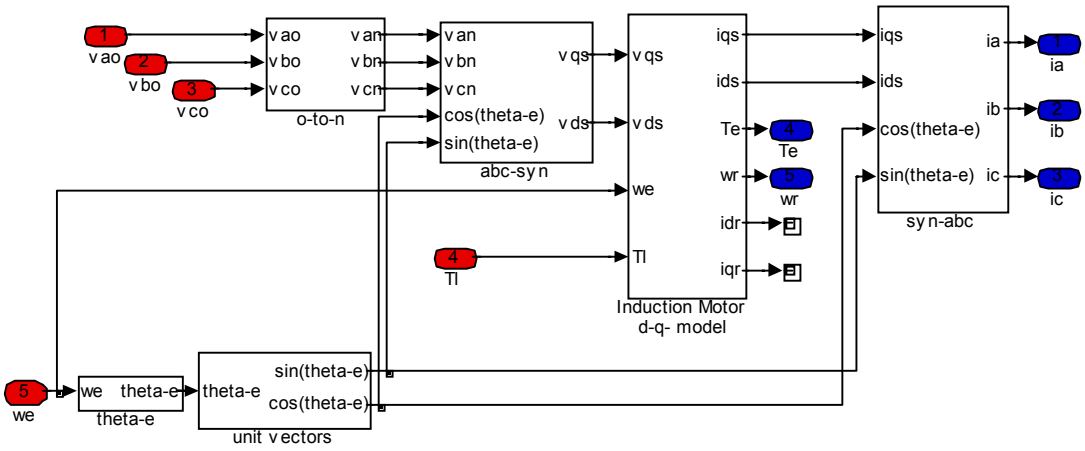

Figure B.1: The complete induction machine SIMULINK model.

represented as follows:

$$\begin{bmatrix} v_{an} \\ v_{bn} \\ v_{cn} \end{bmatrix} = \begin{bmatrix} +\frac{2}{3} & -\frac{1}{3} & -\frac{1}{3} \\ -\frac{1}{3} & +\frac{2}{3} & -\frac{1}{3} \\ -\frac{1}{3} & -\frac{1}{3} & +\frac{2}{3} \end{bmatrix} \begin{bmatrix} v_{ao} \\ v_{bo} \\ v_{co} \end{bmatrix} \tag{B.1}$$

B.1.2. abc-syn conversion block

This block converts the three-phase voltages to a two-phase synchronously rotating frame. To do this, the three-phase voltages are first converted to a two-phase stationary frame using (B.2) and then from the stationary frame to the synchronously rotating frame using (B.3).

$$\begin{bmatrix} v_{qs}^{s} \\ v_{ds}^{s} \end{bmatrix} = \begin{bmatrix} 1 & 0 & 0 \\ 0 & -\frac{1}{\sqrt{3}} & \frac{1}{\sqrt{3}} \end{bmatrix} \begin{bmatrix} v_{an} \\ v_{bn} \\ v_{cn} \end{bmatrix} \tag{B.2}$$

$$\begin{Bmatrix} v_{qs} = v_{qs}^{s} \cos\theta_e - v_{ds}^{s} \sin\theta_e \\ v_{ds} = v_{qs}^{s} \sin\theta_e + v_{ds}^{s} \cos\theta_e \end{Bmatrix} \tag{B.3}$$

B.1.3. syn-abc conversion block

This block does the opposite of the abc-syn conversion block for the current variables using (B.4) and (B.5).

$$\left.\begin{aligned} i_{qs}^{s} &= v_{qs}\cos\theta_e + v_{ds}\sin\theta_e \\ i_{ds}^{s} &= -v_{qs}\sin\theta_e + v_{ds}\cos\theta_e \end{aligned}\right\} \tag{B.4}$$

$$\begin{bmatrix} i_a \\ i_b \\ i_c \end{bmatrix} = \begin{bmatrix} 1 & 0 \\ -\frac{1}{2} & -\frac{\sqrt{3}}{2} \\ -\frac{1}{2} & \frac{\sqrt{3}}{2} \end{bmatrix} \begin{bmatrix} i_{qs}^{s} \\ i_{ds}^{s} \end{bmatrix} \tag{B.5}$$

B.1.4. Unit vector calculation block

The transformations given in the two previous subsections use the unit vectors $cos\theta_e$ and $sin\theta_e$. The angle, θ_e is calculated by integrating the frequency of the input three-phase voltages, ω_e.

$$\theta_e = \int \omega_e dt \tag{B.6}$$

Note that the result of the integration in (B.6) is reset to zero each time it reaches 2π radians. The unit vectors are obtained simply by taking the sine and cosine of θ_e.

B.1.5. Induction machine d-q model block

The induction machine d-q model or the dynamic model is shown in Figure B.2, and the corresponding set of modeling equations are listed in Table B.1 in flux linkage form. To solve these differential equations, they have to be rearranged in the $\dot{x} = Ax + b$ form (Table B.2) where $x = \begin{bmatrix} F_{qs} & F_{ds} & F_{qr} & F_{dr} & \omega_r \end{bmatrix}^T$ is the state

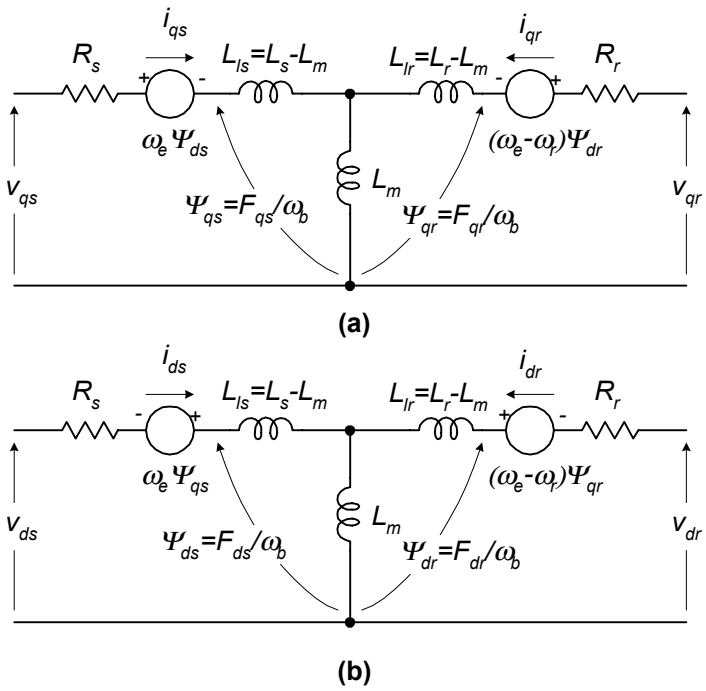

Figure B.2: Dynamic model of an induction machine.

vector. Note that $F_{ij} = \psi_{ij} \cdot \omega_b$, where F_{ij} is the flux linkage (i=q or d and j=s or r), and ψ_{ij} is the flux, and ω_b is the base speed.

In this form, the implementation in SIMULINK is straightforward. First, implement (B.19) - (B.22) with each equation in a block, as seen in Figure B.3 for (B.19). Note that only integrals are used; no derivatives are allowed because derivatives cause problems when their input is discontinuous. Each block then is positioned in Column 1, and the necessary mathematical connections are done as shown in Figure B.4. The outputs of this column are fed to Column 2 where (B.11) and (B.12) are solved. The outputs of the second column are fed to the Column 3 where the current equations, (B.13) – (B.16) are solved. The last

differential equation, (B.23) is solved in the last column together with (B.17). The implementation of (B.23) is shown in Figure B.5. The result of this equation, ω_r is fed back to the rotor flux linkage equations in the first column.

The resulting model is modular and easy to follow. Any variable can be easily traced using the 'scope' blocks. The blocks in the first two columns calculate the flux linkages, which can be used in vector control systems in a flux loop. The blocks in Column 3 calculate all the current variables, which can be both used in the current loops of any current control system and to calculate the three-phase currents. The two blocks of Column 4, on the other hand, calculate the torque and the speed of the induction machine, which again can be used in torque control or speed control loops. These two variables can also be used to calculate the output power of the machine.

Table B.1: Induction motor dynamic model equations (flux linkage form).

$$\frac{dF_{qs}}{dt} = \omega_b \left[v_{qs} - \frac{\omega_e}{\omega_b} F_{ds} + \frac{R_s}{x_{ls}} \left(F_{mq} + F_{qs} \right) \right] \quad \text{(B.7)}$$

$$\frac{dF_{ds}}{dt} = \omega_b \left[v_{ds} + \frac{\omega_e}{\omega_b} F_{qs} + \frac{R_s}{x_{ls}} \left(F_{md} + F_{ds} \right) \right] \quad \text{(B.8)}$$

$$\frac{dF_{qr}}{dt} = \omega_b \left[- \frac{\left(\omega_e - \omega_r \right)}{\omega_b} F_{dr} + \frac{R_r}{x_{lr}} \left(F_{mq} - F_{qr} \right) \right] \quad \text{(B.9)}$$

$$\frac{dF_{dr}}{dt} = \omega_b \left[\frac{\left(\omega_e - \omega_r \right)}{\omega_b} F_{qr} + \frac{R_r}{x_{lr}} \left(F_{md} - F_{dr} \right) \right] \quad \text{(B.10)}$$

$$F_{mq} = x_{ml}^{*} \left[\frac{F_{qs}}{x_{ls}} + \frac{F_{qr}}{x_{lr}} \right] \quad \text{(B.11)}$$

$$F_{md} = x_{ml}^{*} \left[\frac{F_{ds}}{x_{ls}} + \frac{F_{dr}}{x_{lr}} \right] \quad \text{(B.12)}$$

$$i_{qs} = \frac{1}{x_{ls}} \left(F_{qs} - F_{mq} \right) \quad \text{(B.13)}$$

$$i_{ds} = \frac{1}{x_{ls}} \left(F_{ds} - F_{md} \right) \quad \text{(B.14)}$$

$$i_{qr} = \frac{1}{x_{lr}} \left(F_{qr} - F_{mq} \right) \quad \text{(B.15)}$$

$$i_{dr} = \frac{1}{x_{lr}} \left(F_{dr} - F_{md} \right) \quad \text{(B.16)}$$

$$T_e = \frac{3}{2} \left(\frac{p}{2} \right) \frac{1}{\omega_b} \left(F_{ds} i_{qs} - F_{qs} i_{ds} \right) \quad \text{(B.17)}$$

$$T_e - T_L = J \left(\frac{2}{p} \right) \frac{d\omega_r}{dt} \quad \text{(B.18)}$$

Table B.2: (B.7-10,18) in state-space form.

$$\frac{dF_{qs}}{dt} = \omega_b \left[v_{qs} - \frac{\omega_e}{\omega_b} F_{ds} + \frac{R_s}{x_{ls}} \left(\frac{x^*_{ml}}{x_{lr}} F_{qr} + \left(\frac{x^*_{ml}}{x_{ls}} - 1 \right) F_{qs} \right) \right] \tag{B.19}$$

$$\frac{dF_{ds}}{dt} = \omega_b \left[v_{ds} + \frac{\omega_e}{\omega_b} F_{qs} + \frac{R_s}{x_{ls}} \left(\frac{x^*_{ml}}{x_{lr}} F_{dr} + \left(\frac{x^*_{ml}}{x_{ls}} - 1 \right) F_{ds} \right) \right] \tag{B.20}$$

$$\frac{dF_{qr}}{dt} = \omega_b \left[-\frac{(\omega_e - \omega_r)}{\omega_b} F_{dr} + \frac{R_r}{x_{lr}} \left(\frac{x^*_{ml}}{x_{ls}} F_{qs} + \left(\frac{x^*_{ml}}{x_{lr}} - 1 \right) F_{qr} \right) \right] \tag{B.21}$$

$$\frac{dF_{dr}}{dt} = \omega_b \left[\frac{(\omega_e - \omega_r)}{\omega_b} F_{qr} + \frac{R_r}{x_{lr}} \left(\frac{x^*_{ml}}{x_{ls}} F_{ds} + \left(\frac{x^*_{ml}}{x_{lr}} - 1 \right) F_{dr} \right) \right] \tag{B.22}$$

$$\frac{d\omega_r}{dt} = \left(\frac{p}{2J} \right) (T_e - T_L) \tag{B.23}$$

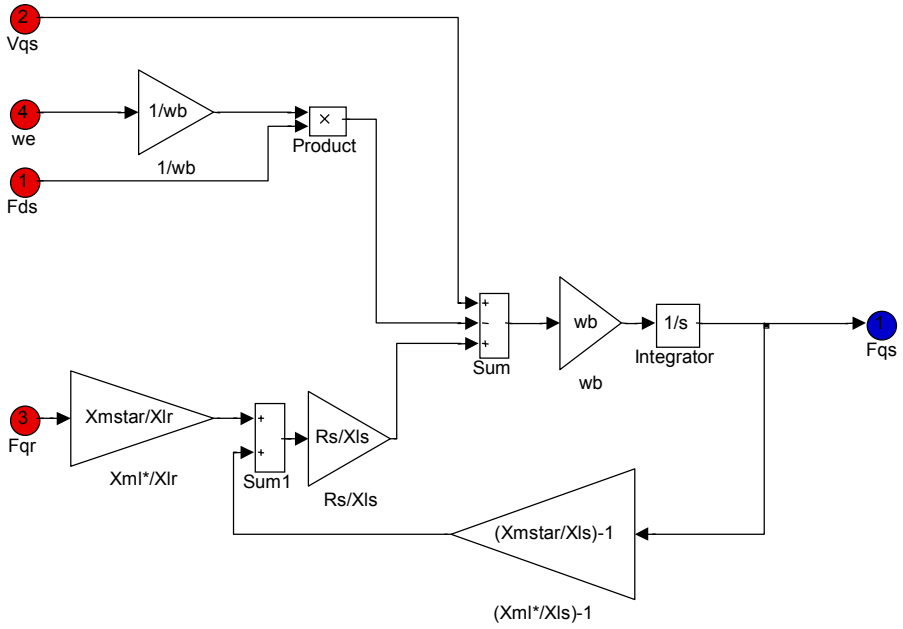

Figure B.3: Implementation of (B.13) in SIMULINK.

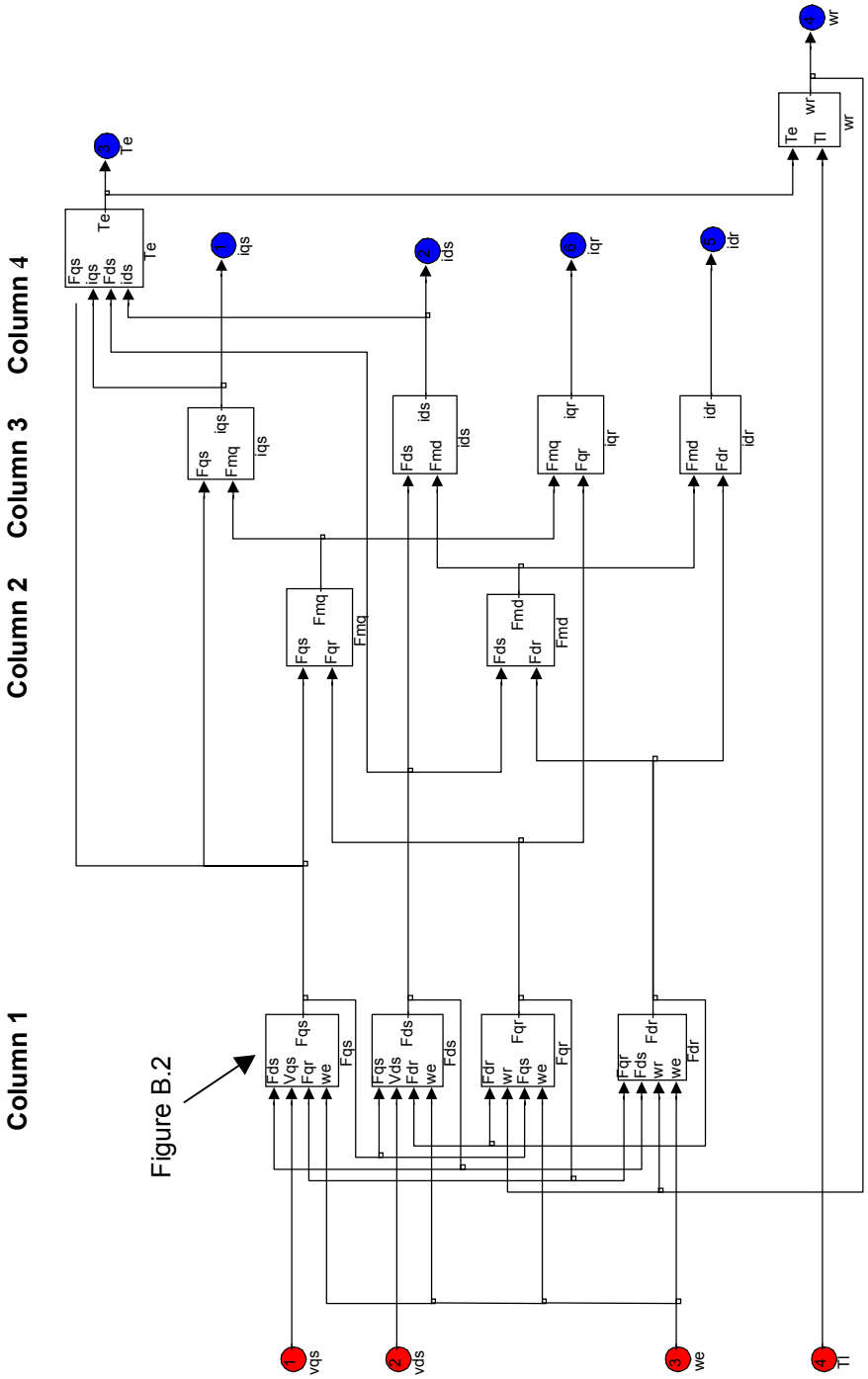

Figure B.4: Induction machine dynamic model implementation in SIMULINK.

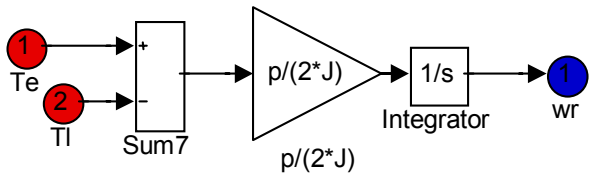

Figure B.5: Implementation of (B.18) in SIMULINK.

B.2. Simulation

B.2.1. Initialization

To simulate the machine in SIMULINK, the model has to be initialized first. For this reason, an initialization file named 'parameters.m' is formed. This file assigns values to the machine parameter variables. For example, Figure B.6 shows the initialization file 'parameters.m' for a 30kW induction machine. Before the simulation this file has to be executed at the MATLAB prompt, otherwise SIMULINK will display an error message.

B.2.2. Results

The induction machine, the parameters of which were listed in Figure B.6 was simulated by applying step speed and load torque changes. First, at zero load torque, the machine is started with 100Hz input voltages. At 0.2s, the frequency is decreased to 60Hz, and at 0.5s it is increased to 80Hz. Then at 0.65s a 35N·m torque is applied which is later decreased to 25N·m. at 1.1s. The simulation results given in Figure B.7 show great speed and torque responses.

```
% 30kw m/c parameters for the d-q induction motor model
% BURAK

% initialization

Rr=.39;                 %rotor resistance
Rs=.19;                 %stator resistance
Lls=.21e-3;             %stator inductance
Llr=.6e-3;              %rotor inductance
Lm=4e-3;                %magnetizing inductance
fb=100;                 %base frequency
p=4;                    %number of poles
J=0.0226;               %moment of inertia
Lr=Llr+Lm;
Tr=Lr/Rr;

%impedance and angular speed calculations

wb=2*pi*fb;             %base speed
Xls=wb*Lls;             %stator impedance
Xlr=wb*Llr;             %rotor impedance
Xm=wb*Lm;               %magnetizing impedance
Xmstar=1/(1/Xls+1/Xm+1/Xlr);
```

Figure B.6: Induction machine model initialization file.

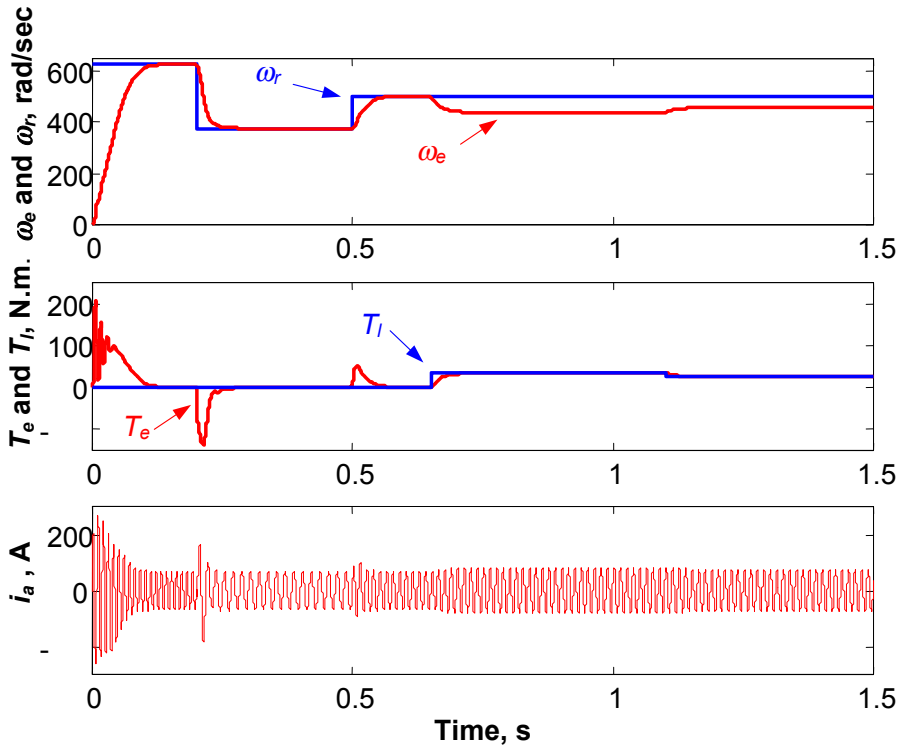

Figure B.7: Induction machine simulation results.

Appendix C

ADVISOR PARAMETERS

ADVISOR is user-friendly conventional, electric, or hybrid electric vehicle simulator package programmed in MATLAB/SIMULINK environment by the U.S. Department of Energy Hybrid Program at the National Renewable Energy Laboratory.

This package includes pre-installed vehicle configurations. For this study, the Prius model is used. The parameters of this model are shown in Figure C.1.

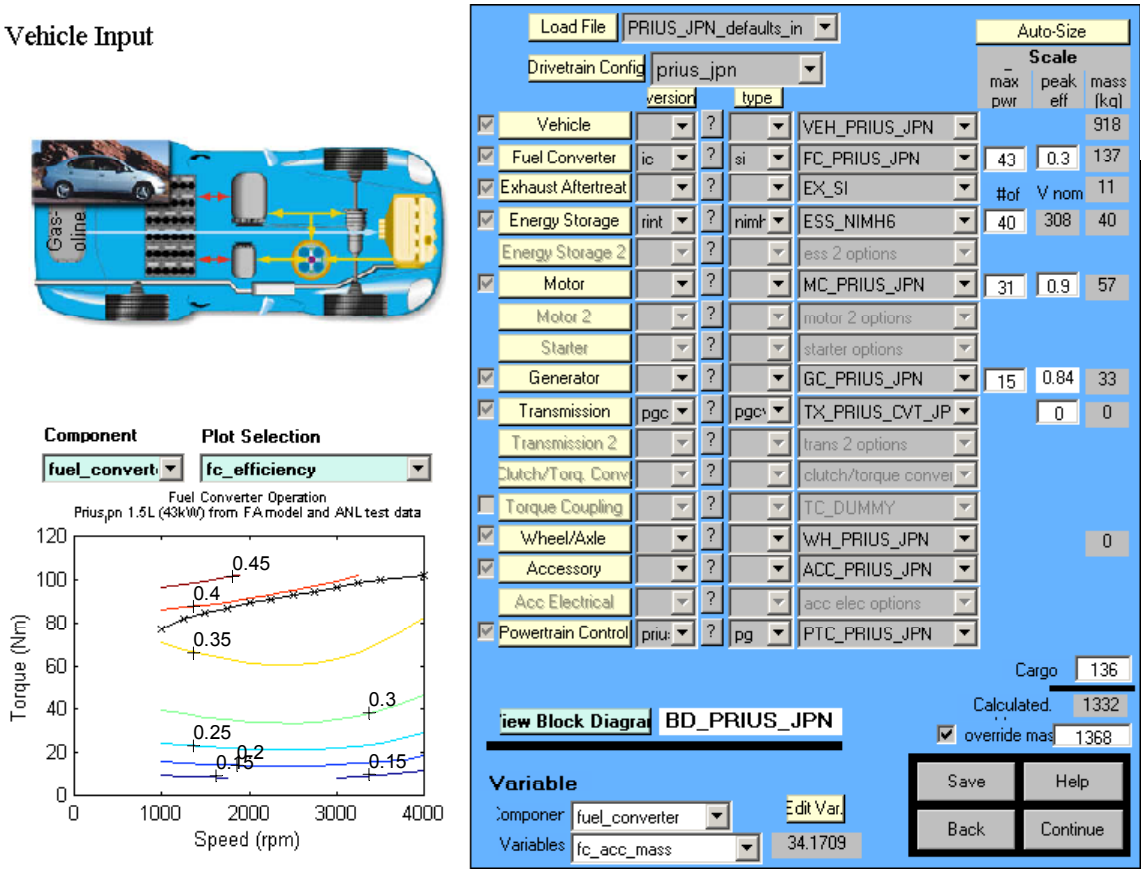

Figure C.1: ADVISOR parameters used in this study

VITA

Burak Ozpineci was born in Istanbul, Turkey in 1972. He entered the Electrical Engineering Department of the Middle East Technical University, Ankara, Turkey. He received a B.S. in electrical engineering on July 3, 1994. He was given a teaching assistantship in the same department. In parallel to this, in September 1995, he joined the power electronics group of The Institute of Information Technologies, Ankara, Turkey where he worked for 9 months as a Project Engineer. In August 1996, he entered the Electrical Engineering Department of The University of Tennessee, Knoxville where he received a M.S. in electrical engineering in 1998. His thesis was titled "*Studies on a Performance Enhanced DC-HFAC-AC Converter for an AC Drive* ". He worked as a graduate research and teaching assistant in the department until he joined the Post-Masters Program with the Power Electronics and Electric Machinery Research Center at the Oak Ridge National Laboratory in February 2001.

He has ten papers published in international conferences and journals, and he holds two international patents. He won the Best Student Paper Award at the IEEE Systems, Man, and Cybernetics conference. He also received University of Tennessee Provost's Citation for Extraordinary Professional Promise.

His research interests include silicon carbide-based power electronic circuits, intelligent control of power electronics, and soft-switching inverters. Burak's e-mail address is *burak@ieee.org*.